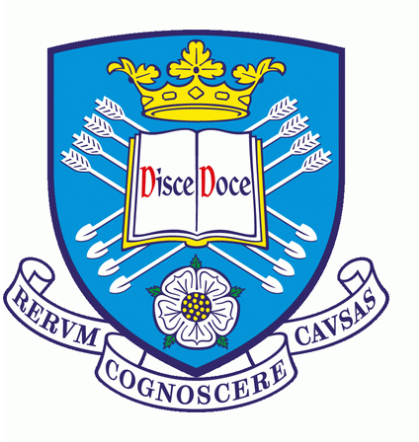

Magnetohydrodynamic Waves in Cylindrical and Multi-slab Environments

Daria Shukhobodskaia

Submitted for the degree of Doctor of Philosophy

School of Mathematics and Statistics

November 2021

Supervisor: Prof Robert von Fáy-Siebenbürgen

Co-Supervisor: Prof Michael S. Ruderman

University of Sheffield

To my family

Abstract

The investigation of magnetohydrodynamic (MHD) wave propagation in different equilibrium configurations is important for the development of solar magneto-seismology (SMS). The applicable models of solar atmospheric waveguides are studied in the framework of Cartesian and cylindrical geometries. First, a magnetised plasma slab sandwiched between an arbitrary number of non-magnetic/ magnetic layers are considered and an analytical approach is used for the derivation of its dispersion relation. The amplitudes of the eigenmodes depend on the equilibrium structuring and the model parameters; this motivates an application as a solar magneto-seismology tool. Specific cases of two- and three-layered slabs are studied in detail and their potential applicability to magnetic bright points is discussed. Furthermore, the resonant damping of propagating kink waves is studied in a straight magnetic flux tube with the density varying along the tube taking into account the magnetic loop expansion. Also non-stationary magnetic tubes to model, for example, cooling coronal loops is considered. In particular, it was found that cooling enhances the wave amplitude and the loop expansion makes this effect more pronounced. After, we analyse 10 driven kink oscillations in coronal loops to further investigate the ability of expansion and cooling to explain complex damping profiles. The used approach could allow to infer some important diagnostic information (such as, for example, the density ratio at the loop foot-points) from the oscillation profile alone, without detailed measurements of the loop and without complex numerical methods. The results imply the existence of correlations between the density ratio at the loop foot-points and the amplitudes and periods of the oscillations. As well, we compare our results to previous models, namely purely Gaussian and purely exponential damping profiles, through the calculation of χ^2 values, finding the inclusion of cooling can produce better fits in some cases. The current study indicates that thermal evolution should be included in kink-mode oscillation models in the future to help us to better understand oscillations that are not purely Gaussian or exponential. Finally, fluting oscillations in a thin straight expanding magnetic flux tube in the presence of background flow are considered. The method of multiple scales is used for the derivation of the system of governing equations. We have found that the amplitude increases due to cooling and is higher for a higher expansion factor. Higher values of the wave number lead to localisation of the oscillation closer to the boundary. We show that the higher the value of the ratio of internal and external plasma densities, the higher the amplification of oscillation due to cooling. So, not only the wave number plays an important role in the evolution of the cooling system, but also the density ratio and the variation of tube expansion are relevant parameters in the cooling process of an oscillating flux tube.

Acknowledgements

First, I would like to express my sincere gratitude to Professor Robert von Fáy-Siebenbürgen for his invaluable support, kindness, guidance throughout my study and for making my PhD such an delightful experience.

As well, I would like to thank Professor Michael S. Ruderman for fruitful discussions, enormous help and expertise, that improved my scientific work.

Moreover, I wish to express my appreciation to Dr Chris Nelson for collaboration in work discussed in Chapter 5.

I am really grateful to all my friends and colleagues from H-floor for mentoring, for friendship, for being ready to help me any time I need it, and for making me feel like home.

Also, I wish to thank the University of Sheffield for funding provided that made this experience possible.

Last, but not least, I want to say thank to my family, my husband Alexander and my kids Vladimir and Yury for their constant inspiration and support during this journey.

Contents

List of Tables

List of Figures

Chapter 1

Introduction

§ 1.1 The Sun: General Information

The Sun is a unique celestial body, which could be even observed with a bare eye. Over millions of years the Sun is nourishing the Earth with life-sustaining energy. Question about the Sun were raised early in the history of mankind. The first records about it could be found in caves as a minimalistic symbolic representations. Later on in the ancient Greece and China solar eclipses were carefully recorded in the form of ancient manuscript. Myriads of ground-based instruments were made in order to understand properties of the Sun. Despite of state-of-the-art technologies, it was impossible to obtain a detailed image of the Sun's surface at that time. The solar image obtained on the Earth is significantly disrupted by the atmosphere of our planet. Fortunately, spacecrafts allowed us to achieve significant scientific progress, that was made in order to comprehend physical properties of this celestial body. This allowed to revolutionise the field of the solar physics more than half a century ago. In 1973, Skylab, with the aid of soft X rays (wavelength = 2.34 -– 4.4 nm), had captured with a moderate resolution of some solar structures that lead to a boom in space-based solar exploration.

One of the reasons why the Sun is still the point of great interest for contemporary physicists is that despite the numerous observational and theoretical works, there are still unresolved fundamental questions about the Sun. One of these questions is the so-called coronal heating problem.

The best way to prepare our mind in order to comprehend such a complex query is to describe the structure of the Sun (see e.g. Priest, 2014). The Sun is assumed to consists of plasma, one of the four fundamental states of matter. In more details, plasma is a highly ionised gaseous substance, making it highly conductive. As a result, plasma behaviour has a significant impact exerted by both from electrical and magnetic fields, with comparison to ordinary fluid. Figure 1.1 provides an intuitive summary of the solar structure. Normally, the structure of the Sun is separated into two specific regions. The first one cannot be observed directly, and is known as the internal region of the Sun. While the second one could be seen directly with the aid of observational instruments and is known as the solar atmosphere. Following the schematic representation of 1.1, the internal region of the Sun starts from core and extends up into the convection zone,

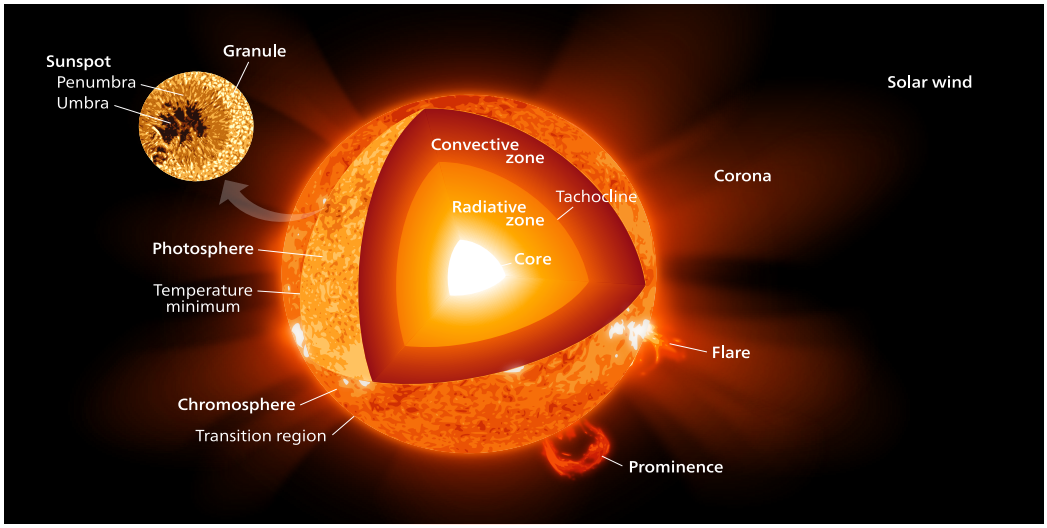

Figure 1.1: The schematic diagram of the Sun's structure. All features drawn to scale. Adapted from Wikipedia, credits to Kelvinsong (2014)

while the solar atmosphere starts with photosphere and ends with the corona.

Interestingly, contemporary solar theory leads us to believe that ≈ 50 % of the solar mass is present within the boundaries of the core region with the radius being only 25 % of the entire radius of the Sun. We estimate the solar mass as $M_\odot \approx 1.99 \times 10^{30}$ kg and the radius of the Sun as $R_\odot = 695.5$ Mm. Furthermore, it is assumed that ≈ 99 % of nuclear fusion happens in that region. As a result, the core is not only the most dense region of the Sun located within $1/4R_\odot$, but also it generates the most significant amount of energy. All this information suggests that we could estimate the temperature of the solar core as $\approx 1.5 \times 10^7$ K.

Following Figure 1.1, let us move to the next region above the core. This layer is commonly called the radiative zone. The name of this region is given by the main suggested energy transfer mechanism – radiation. This region has a proposed theoretical thickness of $0.45R_\odot$ and is closest to the core.

Moving further up in Figure 1.1, we end up next in the tachocline. This layer is relatively thin, only $\approx 0.04R_\odot$. Moreover, the two layers that sandwich the tachocline, the radiative zone and convectional zone, have completely different behaviour of rotation. The first one moves resembling a solid body, while the former has liquid like rotational properties. Therefore, the tachocline is always under an extremely high shear stress.

The final layer of the internal structure of the Sun is known as the convection zone. Similarly to the radiation zone, its name is give by the most significant energy transfer mechanism within the layer – the convection. Its thickness is $0.3R_\odot$. Furthermore, since convection is the main energy transfer mechanism, the hot plasma is actually moving from the center of the Sun towards the cooler photosphere.

The photosphere is the lowest layer of the solar atmosphere and its thickness is in the

region of $\approx 7\times10^{-4}R_{\odot}$, that makes the photosphere much thinner in case it is compared to other solar layers as seen in Figure 1.1. However, it is the most dense visible layer of the Sun, with its density being approximated around 10^{-4} kg/m^3. Furthermore, most of the photosphere consist of granules with cold and dark boundaries around hot and bright centers. The reason behind the granulation is the convection motion, with hot plasma rising towards the photosphere and cold plasma returning back to the convection zone. In case of high-intensity magnetic flux, which often accompanies convection, it is possible to observe large dark structures known as sunspots.

The next layer is known as the chromosphere. The thickness of this layer is not homogeneous and varies with location to be anything between 0.003–$0.02R_{\odot}$. The typical observed structures within this region are spicules and jets.

Next, the transition region is a very narrow layer, around $100km$, of the solar atmosphere. The interesting feature of this region is that the temperature within this region rises dramatically from about 25000 K to over 10^6 K.

The outermost region of the solar atmosphere is the corona as shown in Figure 1.1. It consists of extremely hot plasma, has a strong magnetic field and a very low density. It is estimated that the corona is located in the interval of 1–$3R_{\odot}$ away from the solar geometrical center. The typical observable structures in the solar corona are known as coronal loops, which are typically fixed to the much denser photosphere. Moreover, the corona is one of the most interesting and marvelous parts of the Sun. The reason is that its temperatures is 200 times higher than the temperature of the photosphere (see e.g., Klimchuk, 2006). This phenomenon puzzles the scientific community with contemporary physical knowledge, where it is a norm to accept that the heat dissipates further away from its source and constitutes one of the major problems of solar physics. Fortunately, there are at least two classes of potential candidates to be accounted for such an unexpected temperature behaviour. The first one is known as magnetic reconnection, where Ohmic dissipation is present (see e.g, Priest, 1999). Whereas, the other one is energy dissipation, as a result of e.g. wave damping (see e.g., Nakariakov et al., 1999).

§ 1.2 MHD Waves in Slab Geometry

1.2.1 General information

The solar atmosphere, from the photosphere to the corona, is dominated by a complex and dynamic magnetic field that makes the plasma highly structured. Over the past few decades, vast improvements in solar telescope technology, with the likes of both space-borne instrumentation, *e.g.* SoHO (Solar and Heliospheric Observatory), SDO (Solar Dynamics Observatory), and IRIS (Interface Region Imaging Spectograph), and ground-based solar observing facilities, *e.g.* DST (Dunn Solar Telescope) and SST (Swedish Solar Telescope), have enabled us to resolve the fine sub-structure within many of the larger magnetic features that bejewel the solar atmosphere. Considering the development of the next generation of observational mega-projects, such as the rather imminent commencement of DKIST (Daniel K. Inouye Solar Telescope) and, within

a decade, that of EST (European Solar Telescope), this trend looks set to continue, which motivates solar physicists to fill the gaps in theoretical understanding. Multi-wavelength observations from high-resolution satellites and ground-based telescopes enable the detection of periodic motions in different magnetic structures in the solar atmosphere, such as in coronal loops (see *e.g.* Aschwanden 2005, Thompson et al. 1998, Banerjee et al. 2007, de Moortel 2009), plumes (see *e.g.* Ofman et al. 1997, DeForest and Gurman 1998, Nakariakov 2006), prominences (*e.g.* Arregui et al. 2012), solar wind (see *e.g.* Belcher 1971, Abbo et al. 2016) and spicules (see *e.g.* Zaqarashvili and Erdelyi 2009, Tsiropoula et al. 2012).

These observed periodic perturbations may be described in terms of magnetohydrodynamic (MHD) waves. MHD waves are a key in our understanding of the physical processes in the hot solar plasma. They are not only a mechanism to transfer non-thermal energy between distant locations in the solar plasma, that is then dissipated by physical processes that are yet to be fully understood, like resonant absorption (see *e.g.* Goossens et al. 2011), phase mixing (see *e.g.* Heyvaerts and Priest 1983), non-linear shock damping (see *e.g.* Ballai and Ruderman 2011), rather, they are also excellent tools to be exploited for plasma diagnostics by solar magneto-seismology (SMS) (see *e.g.* the reviews by Nakariakov and Verwichte, 2005; Erdélyi, 2006a,b; Andries et al., 2009; Ruderman and Erdélyi, 2009; De Moortel and Nakariakov, 2012; Mathioudakis et al., 2013).

High-resolution observations of waves and oscillations in magnetic structures, combined with theoretical MHD wave modelling, enable us using a suitable inversion to determine the solar atmospheric parameters that are often very hard to measure directly, such as *e.g.* the coronal magnetic field strength (Nakariakov and Ofman 2001, Erdélyi and Taroyan 2008). The principles of SMS were first suggested by Uchida (1970), Zajtsev and Stepanov (1975) and Roberts et al. (1984) for coronal application, and by Tandberg-Hanssen (1995) for prominence application.

Studying MHD wave propagation is a popular and challenging research topic with plenty of applications to solar and solar-terrestrial plasmas. Their significance has increased not only because of their potential as a remote diagnostic tool, as outlined above, but also due to their presumed contribution to plasma heating processes. It is believed that the heating processes that generate and sustain the hot solar atmosphere may be accounted for the MHD waves (see *e.g.* Alfvén 1947, Osterbrock 1961, Ionson 1978, Hollweg 1991, Goossens et al. 2011, Mathioudakis et al. 2013) that are generated by the convection reservoir and propagating from the lower atmosphere (see *e.g.* Roberts 2000). These and alternative mechanisms such as magnetic reconnection and nano-flares could potentially contribute to coronal heating (see. e.g. Klimchuk 2006; Parnell and De Moortel 2012; Klimchuk 2015).

1.2.2 Previous work

There are two geometric model building-blocks that are popular to approximate the solar atmospheric waveguides: the cylindrical flux tube and the magnetic slab waveguides. The present section focuses on the latter, which can be used as the initial approxima-

tion to model a wide variety of solar atmospheric structures, including prominences, magnetic bright points, light bridges and their corresponding light walls (see *e.g.* Yang et al. 2016, Yang et al. 2017, Yuan et al. 2014), coronal hole boundary layers, the flank structure of coronal mass ejections, as well as several magnetospheric regions.

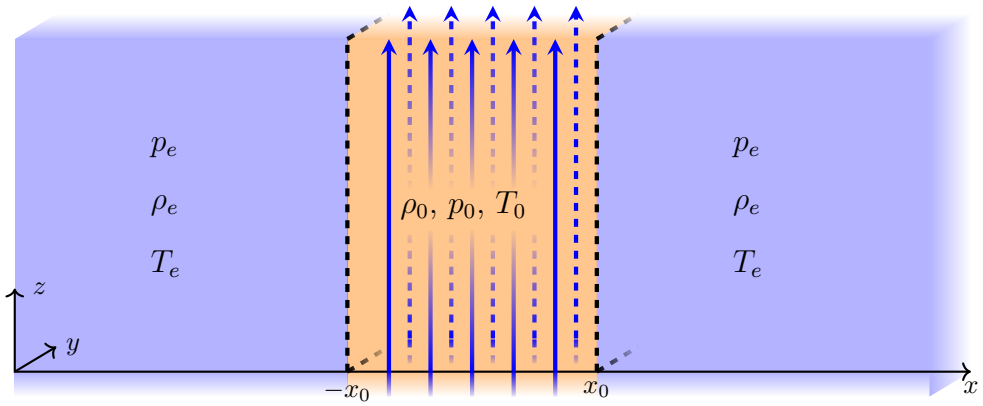

Figure 1.2: The equilibrium configuration for a magnetic slab in a symmetric non-magnetic environment.

First studied as an interface between two semi-infinite plasmas (Roberts, 1981a), the currently frequently used and popular format of the theory of MHD wave propagation in Cartesian geometry has been developed to describe magnetic slabs embedded in non-magnetic (Roberts, 1981b) and magnetic external environment (Edwin and Roberts, 1982), as illustrated on Figure 1.2. It was shown for a non-magnetic environment, that the transverse velocity component has the form

$$\widehat{v}_x(x) = \begin{cases} A_e \exp m_e(x + x_0), & \text{for } x < -x_0, \\ A_0 \cosh m_0 x + B_0 \sinh m_0 x, & \text{for } -x_0 < x < x_0, \\ B_e \exp -m_e(x - x_0), & \text{for } x > x_0, \end{cases} \tag{1.1}$$

where

$$m_e^2 = k^2 - \frac{\omega^2}{c_e^2}, \quad m_0^2 = \frac{(k^2 c_0^2 - \omega^2)(k^2 v_A^2 - \omega^2)}{(c_0^2 + v_A^2)(k^2 c_T^2 - \omega^2)}, \quad c_T^2 = \frac{c_0^2 v_A^2}{c_0^2 + v_A^2},$$

c_0 and c_e are the speeds of sound in the slab and in the external environment, v_A is the Alfvén speed, k is the wavenumber in the z-direction and ω is the angular frequency, A_e, B_e, A_0, B_0 are arbitrary constants. The sign of m_e is assumed to be positive, however m_0^2 could be positive or negative, depending on it the wave could be classified as surface ($m_0^2 > 0$) or body wave ($m_0^2 < 0$). Boundary conditions were applied and the dispersion relation was obtained and decoupled into two equations:

$$(k^2 v_A^2 - \omega^2) m_e = \left(\frac{\rho_e}{\rho_0}\right) \omega^2 m_0 \begin{pmatrix} \tanh m_0 x_0 \\ \coth m_0 x_0 \end{pmatrix}. \tag{1.2}$$

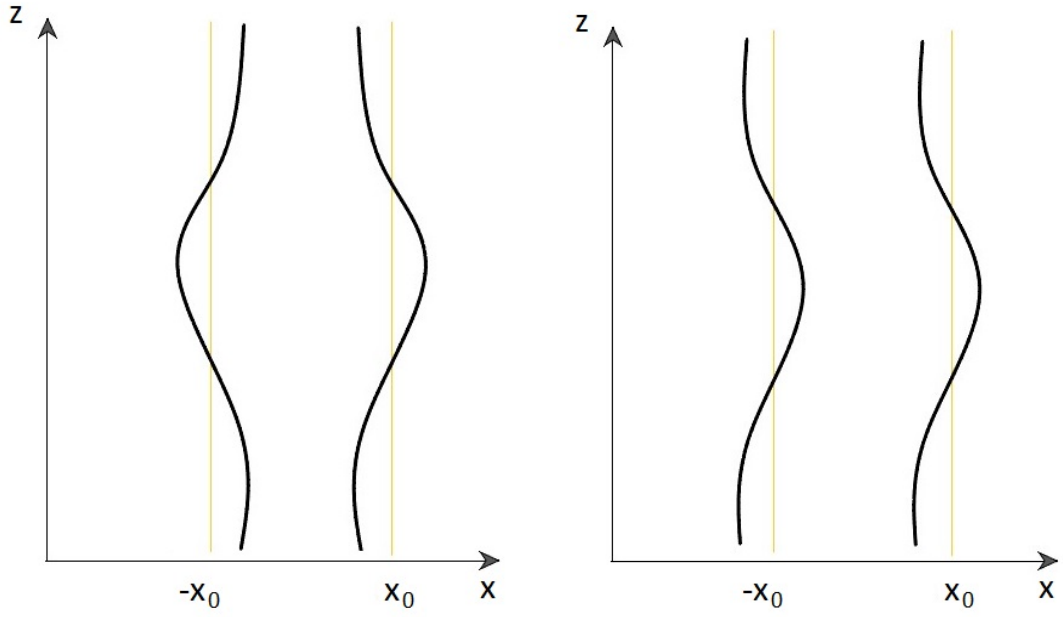

Sausage mode Kink mode

Figure 1.3: Schematic representation of the sausage and kink modes.

The equation with tanh corresponds to sausage modes, transverse velocity perturbation $\widehat{v_x}$ of whose is anti-symmetric around the center of the slab. Symmetric velocity perturbations around $x = 0$ are called the kink modes and are defined by the equation with coth. These modes are illustrated in Figure 1.3.

In more recent studies, the magnetic slab was investigated in asymmetric nonmagnetic and magnetic environments (Allcock and Erdélyi, 2017; Zsámberger et al., 2018) and multi-layered plasmas (Ruderman, 1992; Shukhobodskaia and Erdélyi, 2018). It was shown that in general, the solutions of the exact dispersion relation for both the externally field-free and magnetically asymmetric slab systems are the mixed-nature quasi-sausage and quasi-kink modes. Furthermore, collective standing modes of a multi-layered Cartesian waveguide modelling multi-fibril prominence oscillations (see *e.g.* Díaz et al. 2005; Díaz and Roberts 2006) and coronal loop oscillations (see *e.g.* Luna et al. 2006) have been studied.

Aside from providing a description and nomenclature of solar atmospheric wave physics, the theoretical studies have driven progress in SMS. The asymmetric environment of solar waveguides has been theoretically proposed as a proxy for the local inhomogeneity, *e.g.* in the magnetic field, density, and temperature. This inhomogeneity, through the Amplitude Ratio and the Minimum Perturbation Shift Methods, can be exploited for SMS (Allcock and Erdélyi, 2018). With the sub-structure resolution that these techniques require being reached by some of the currently available instrument suits for solar atmospheric waveguide structures, these techniques were applied

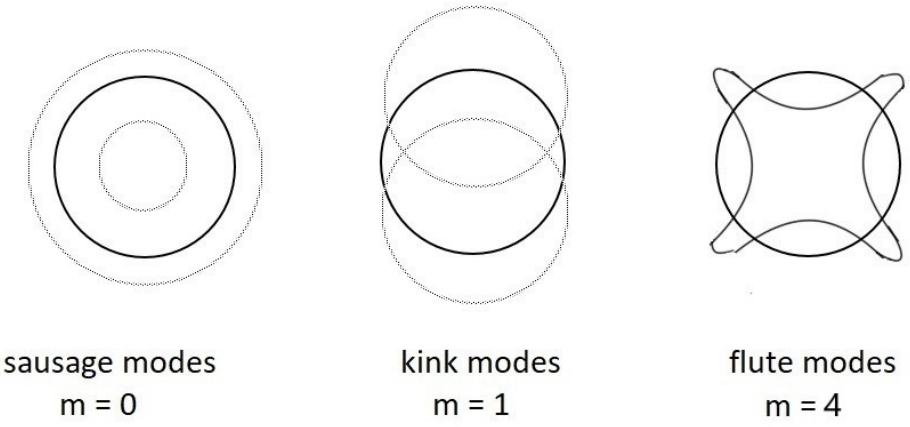

Figure 1.4: Schematic representation of possible modes in cylindrical geometry.

in Allcock et al. (2019) for estimating the Alfvén speed in several chromospheric fibrils.

§ 1.3 MHD Waves in Magnetic Flux Tube Framework

1.3.1 General information

Similarly to the magnetic slab framework, it is customary to categorize the wave modes in a magnetic flux tube depending on the azimuthal wavenumber m (see, e.g., Edwin and Roberts, 1983). Figure 1.4 represents possible configurations in the framework of magnetic flux tube, where $m = 0$ corresponds to sausage waves, modes with $m = 1$ are the kink modes, and modes with $m \geq 2$ are called the fluting modes. It is worth to remarks that the behaviour of kink, sausage and fluting modes are resembling the ones of the slab. Such a framework was shown to have significant impact on explanation of the wave dynamics in coronal loops, solar prominences and filaments. In the next subsection, the previous work on the application of the mathematical theory will be described as a proof of ultimate significance.

1.3.2 Previous work

Propagating kink waves have been observed in many magnetic waveguides in the solar atmosphere, like coronal magnetic loops (see *e.g.* Tomczyk et al., 2007, Tomczyk and McIntosh, 2009), spicules (see *e.g.* De Pontieu et al., 2007, He et al., 2009), fine structures of prominences (see *e.g.* Okamoto et al., 2007), and in filament threads (see *e.g.* Lin et al., 2007, 2009). We note that although some of these observed results were interpreted as Alfvén waves, they might be also interpreted as kink waves (see *e.g.* Doorsselaere et al., 2008; Erdélyi and Fedun, 2007). Both waves could contribute to coronal heating, however they have significant differences, as an Alfvén wave has only torsional component for motion, whereas kink wave has both torsional and transverse

components, that makes the latter easier to identify in observation. One of the first approaches used for modelling solar atmospheric waveguides was based on representing a flux tube as a straight homogeneous magnetic cylinder (see, e.g. Ryutov and Ryutova 1976, Edwin and Roberts 1983). Since then, more complex and more realistic models were developed, for recent reviews see, e.g. Nakariakov and Verwichte, 2005, Ruderman and Erdélyi, 2009, Nakariakov et al., 2016.

It was also observed that these waves damp. The damping profiles of the majority of driven kink-mode oscillations can be well fitted by either Gaussian or exponential profiles (as shown in the statistical study of Goddard et al. 2016) and numerous physical mechanisms have been proposed to account for such decay. At present, resonant absorption is considered as one of the most likely candidate for explaining this damping and it has been widely analysed in numerous analytical works with the aim of better understanding damping within kink-mode oscillations (e.g., Ruderman and Roberts 2002, Goossens et al. 2002, Dymova and Ruderman 2006). Interestingly, resonant absorption was proposed well before the first direct detection of kink-modes in coronal loops in the solar atmosphere (Hollweg and Yang 1988; Goossens et al. 1992; Erdelyi and Goossens 1994, 1995).

The theoretical modelling of the spatial damping of travelling kink waves due to resonant absorption was carried out by e.g. Terradas et al. (2010) and Verth et al. (2010) analytically, and by e.g. Pascoe et al. (2010, 2011) numerically. In all these studies the simplest model of a straight magnetic tube with the density only varying in the radial direction was used.

Later, more sophisticate models have emerged. Soler et al. (2011a) took into account the effect of partial ionisation in the single-fluid approximation. As a result, kink waves were damped by both resonant absorption and ion-neutral collisions. Soler et al. (2011b) studied the resonant absorption of propagating kink waves in the presence of flow. Soler et al. (2011c) investigated the propagation and resonant absorption of kink waves in a magnetic tube with the density varying both along and across the tube. They showed that the variation of the wave amplitude along the tube is determined by the combined effect of resonant damping and the longitudinal density variation. Ruderman et al. (2010) studied the effect of nonlinearity on the resonant damping of propagating kink waves and showed that nonlinearity can strongly enhance the damping efficiency.

All papers cited above used the theory of resonant damping that can now be called "classical". In this theory, the wave amplitude decays exponentially with the distance from the place where it is driven. This result is based on the assumption that a propagating kink wave is an eigenmode of the linearised dissipative MHD.

Standing, driven kink-mode oscillations within coronal loops have been extensively studied by the community ever since they were detected in the solar atmosphere at the end of the 20th Century (Aschwanden et al. 1999; Nakariakov et al. 1999) and for reviews see e.g. Andries et al. (2009); Ruderman and Erdélyi (2009). It is now known that, typically, flare-driven kink-mode oscillations are observed to damp within only a few periods, faster than would routinely be expected given the large amplitudes present (see *e.g.* Aschwanden and Terradas 2008), implying the presence of complex physics during these relatively routine events. In the case of standing kink oscillations

Ruderman and Roberts (2002) showed that after the initial perturbation the kink oscillation of a perturbed magnetic tube is very well described by an eigenmode, within the framework of linear dissipative MHD, after a transitional time of order of the oscillation period everywhere but in a vicinity of the resonant surface. However, in the vicinity of the resonant surface phase mixing continues until it creates perturbations with so small spatial scales that viscosity and/or resistivity stops it. Only after that the perturbation is described by an eigenmode of the linear dissipative MHD everywhere. It was shown numerically that, for typical parameters of coronal magnetic loops, the time when phase mixing stops is at least by an order of magnitude larger than the typical damping time of kink oscillations (Arregui, 2015).

Hence, we conclude that the main assumption of the classical theory of resonant damping is not satisfied. This problem was addressed numerically by e.g. Pascoe et al. (2013), and analytically by Hood et al. (2013). The potential transition from Gaussian to exponential damping during the course of a single coronal loop oscillation for propagating kink waves was derived in the absence of cooling. It was shown that at the initial stage the amplitude variation with the distance from the driver is described by the Gaussian profile. And, only later, the amplitude decays exponentially. As a result, the damping length of a kink wave is somewhat longer than that predicted by the classical theory of resonant damping. Hence, to correctly describe the spatial damping of propagating kink waves we need to use the advanced theory developed by Hood et al. (2013).

Ruderman and Terradas (2013) carried out an analytical analysis of resonant damping of standing kink waves similar to that made by Hood et al. (2013) for propagating kink waves. They, in particular, concluded that the classical theory of resonant damping underestimates the damping time. But, for typical values of coronal magnetic loop parameters, the errors never exceed 20%. Although a similar estimate was not obtained for propagating kink waves, on the basis of the analogy between the spatial damping of propagating waves and temporal damping of standing waves, we believe that, although the classical theory of resonant damping underestimate the damping length, the error is quite moderate. On the other hand, the advanced theory of resonant damping is much more complex than the classical theory. Hence, in this thesis we will use the classical theory of resonant damping. For a review on resonant absorption without complex profiles in a solar context see Goossens et al. (2011).

The improvement in both the spatial and temporal resolutions of coronal imaging which resulted from the launch of the Solar Dynamics Observatory's Atmospheric Imaging Assembly (SDO/AIA; Lemen et al. 2012) in 2010 has facilitated major advances in understanding of coronal loop oscillations over the past decade. For example, it is now known that multiple harmonics can be present in kink-mode oscillations (Pascoe et al. 2016a), that decay-less observations are present in some coronal loops (Anfinogentov et al. 2013), and that coronal loops can be multi-thermal in nature (see *e.g.* Schmelz and Martens 2005; Schmelz et al. 2007; Krishna Prasad et al. 2017). One of the main benefits of the continuous, full-disk observations provided by the SDO/AIA instrument is that large statistical studies of coronal loop oscillations can now be conducted (see, e.g., Zimovets and Nakariakov 2015; Goddard et al. 2016). Goddard et al. (2016), for

example, studied 120 kink-mode oscillations finding parameters such as amplitudes, damping times, and periods. Ground-based facilities also enable such statistical investigations in chromospheric wave-guides, as were conducted by Kuridze et al. (2012), Morton et al. (2012) who studied the properties of transverse oscillations in mottles. Furthermore, for the example of undamped kink oscillations presented by Aschwanden and Schrijver (2011), Kumar et al. (2013) showed that such phenomena could be triggered by the combination of fast and slow MHD waves present within the system. Moreover, Wang et al. (2012) suggested that amplification could occur due to additional energy input, potentially associated with flaring during the lifetime of the initial oscillation (Pascoe et al. 2020).

Such studies are highly valuable and provide important constraints which can help with the verification of numerical and analytical theories. Interestingly, although the evolution of the majority of coronal loop oscillations analysed by Goddard et al. (2016) could be modelled using Gaussian, exponential, or Gaussian followed by exponential fits, 21 decaying kink-mode oscillations were identified which had combinations of both exponential and non-exponential damping profiles co-temporally. The presence of these complex or non-standard damping profiles, which cannot be approximated by a few Gaussian profiles and exponential profiles attached to each other in a definite order, sometimes including amplification of the oscillations through time, implies further work is required to fully understand what effects are important in defining the evolution of kink-modes in some coronal loops.

More recently, the idea of analytically studying cooling effect on MHD waves (see e.g. Morton et al. 2010) and in particular on the seismological properties for kink oscillations of coronal loops (see Morton and Erdélyi 2009, 2010) was proposed. Morton and Erdélyi (2010); Ruderman (2011c) concluded that in the absence of damping due to resonant absorption cooling can cause amplification of coronal loops. Furthermore Ruderman (2011b) concluded that combining cooling and resonant damping can result in the amplitude not varying in time (i.e., the oscillation being decay-less). Ruderman et al. (2017) studied the combination of cooling and expansion for non-damped kink oscillations, it was shown that expansion of coronal loops acts in favour of amplification. Shukhobodskiy et al. (2018) considered a similar problem in the presence of damping due to resonant absorption and found that the combination of cooling and expansion can lead to an increase in the oscillation amplitude even in the presence of resonant damping. The theory was later tested observationally by Nelson et al. (2019) on one kink-mode oscillation. It was found that increases in the amplitude of the oscillation through time could be explained if cooling was considered, without the need of external forces (e.g., additional flaring) affecting the oscillating system in order to sustain oscillation.

Cooling has been observed in many coronal loops during their lifetimes and has numerous observational signatures, both direct and indirect. The most direct signature is the visible transition of the loops from channels sampling hotter plasma to channels sampling cooler plasma through time (as was shown by, for example, Winebarger and Warren 2005; López Fuentes et al. 2007; Aschwanden and Terradas 2008). More indirect mechanisms include coronal rain (e.g., Antolin et al. 2015) and associated process such

as downflows in transition region spectra at the foot-points of coronal loops (Kleint et al. 2014; Ishikawa et al. 2020). Both coronal rain and transition region downflows have been shown to be stable (Antolin et al. 2015; Straus et al. 2015) and variable (Antolin et al. 2015; Nelson et al. 2020a) over short time-scales meaning the thermal evolution of coronal loops may be an on-going and variable process throughout their lifetimes. It is known that transition region downflows occur above almost all sunspots (Samanta et al. 2018; Nelson et al. 2020b) implying that a high number of coronal loops do not maintain constant temperatures through time. The effects of thermal evolution (both heating and cooling) within loops should, therefore, be considered when analysing the oscillations of coronal loops (see e.g. Morton et al. 2010; Erdélyi et al. 2011; Al-Ghafri and Erdélyi 2013; Al-Ghafri et al. 2014 to name a few studies).

Properties of the sausage and kink modes were studied in a significant number of articles, while on the contrary, the fluting modes are not getting sufficient attention that probably might be explained by the absence of observations associated with fluting modes. A reason for the lack of observed detection of these modes may be related to the needed high spatial and temporal resolution that are not easy to achieve.

Nevertheless, there is a great interest in investigating the fluting modes with theoretical approach as analysing these modes may provide a further insight into the sub-resolution structure of a waveguide let alone their contribution to heating. An initial insight into the properties of the oscillations of the flux tube with fluting modes is given by Edwin and Roberts (1983). There, a homogeneous thin flux tube was studied, and it was shown how the kink and fluting modes behave under solar atmospheric circumstances. However, e.g. Ruderman et al. (2017) has theoretically revealed for the kink modes that the dispersion is rather different for non-homogeneous flux tube with plasma flow even in the thin tube and thin boundary approximation. Moreover, numerical experiments and contemporary theory suggest that the kink and fluting waves could couple in a nonlinear fashion (see, e.g., Ruderman et al., 2010; Ruderman, 2017; Terradas et al., 2018). Another interesting aspect is that high azimuthal wavenumbers could be determinant in the cause of the Kelvin-Helmoltz instability (see, e.g., Terradas et al., 2008; Antolin et al., 2014; Magyar and Van Doorsselaere, 2016). As a result, additional investigation of the behaviour of the fluting oscillations could complement the analysis of the sausage and kink modes. Examples of the latter are e.g. Pascoe et al. (2016c); Pascoe et al. (2017); Nelson et al. (2019); Shukhobodskaia et al. (2020) where significant development has lead to a better understanding of kink oscillations of coronal loops, although the contemporary theory still is unable to perfectly match the observed oscillation patterns.

§ 1.4 Outline and structure

The thesis is divide into two main sections. The first one is devoted to the application of magnetic slab framework to wave dynamics in the Sun (chapters 2 and 3). The former is employing advantages of magnetic flux tube approximations in order to describe solar structure (Chapters 4 – 6).

In Chapter 2, based on Shukhobodskaia and Erdélyi (2018), the existence of MHD

waves is considered in a model of a magnetised plasma slab sandwiched between an arbitrary number of interfaces with different densities and temperatures with a straight and uniform magnetic field only present in one layer. The general dispersion relation is derived and is solved analytically for the cases of two (*i.e.* one magnetic and one non-magnetic) or three (*i.e.* a magnetic slab sandwiched between two asymmetric) slabs in the cases of an incompressible fluid and under the thin-slab approximation.

Next, Chapter 3 introduces a general model of a multi-layered MHD waveguide, for which the dispersion relation for linear magneto-acoustic waves is derived. The special case of two magnetic slabs in an asymmetric magnetic environment is discussed. The results presented in this Chapter were published in Allcock et al. (2019).

In the next Chapter (Chapter 4), the propagation of MHD waves in a straight magnetic tube with circular cross-section of variable radius is studied. The standard linearised MHD equations as well as governing equation from Ruderman et al. (2017) are employed to derive an equation that describes the behaviour of a non-stationary magnetic flux tube in the presence of propagating kink waves. Afterwards, the expression that incorporates resonant damping is derived. Furthermore, the amplitude of the wave is found there. Finally, these results are used in order to conduct numerical experiment and obtain behavioural profile of propagating kink wave in the expanding magnetic flux tube. The chapter was build upon Ruderman et al. (2019).

Chapter 5, that was influenced by Shukhobodskaia et al. (2020), is using the advantages of the theory presented by Shukhobodskiy et al. (2018) in order to notify about the importance of cooling within kink oscillations of coronal loops. 10 events of kink oscillations of coronal loops are studied in that chapter. With the aid of the slit technique, canny edge detection method and detrending the oscillation profile was estimated. The obtained result show significant deviation from Gaussian and exponential damping profiles discussed in Pascoe et al. (2016a). In accordance with Shukhobodskiy et al. (2018), the damping profiles generated in the presence of cooling could be Gaussian, exponential or of other nature. At the end, rather than damping, the wave could amplify. Oscillation profiles are later compared for cooling model, and Gaussian and exponential profiles are investigated. The discussion about the results of comparison are later presented and significance of the cooling effect for comprehension of kink oscillation of coronal loops is presented.

In the next Chapter, we analyse the fluting waves in a thin and expanding magnetic flux tube in the presence of a background flow. The tube consist of the core region, where the effect on density variation on radial component is minimal, and transitional region where density could vary in radial component as well and resonant absorption occurs. With the aid of the linearised MHD equations the governing equation describing such system is obtained. That equation is valid for both standing and propagating waves, making it useful to apply for studying waves in coronal loops, fillaments and prominences. Next, in the case the transitional layer is absent, an adiabatic invariant is obtained and a Kelvin-Helmholtz stability region is found. Then, the governing equation is solved numerically to investigate the effect of wavenumber m, density ratio ζ and magnetic flux tube expansion. The results presented in this Chapter were submitted to Shukhobodskaia et al. (2021).

In the final Chapter, we conclude about all of the achievements of this thesis and discuss potential future work.

Chapter 2

Surface MHD Waves in Asymmetric Multi-Layered Plasma

§ 2.1 Derivation of General Dispersion Relation

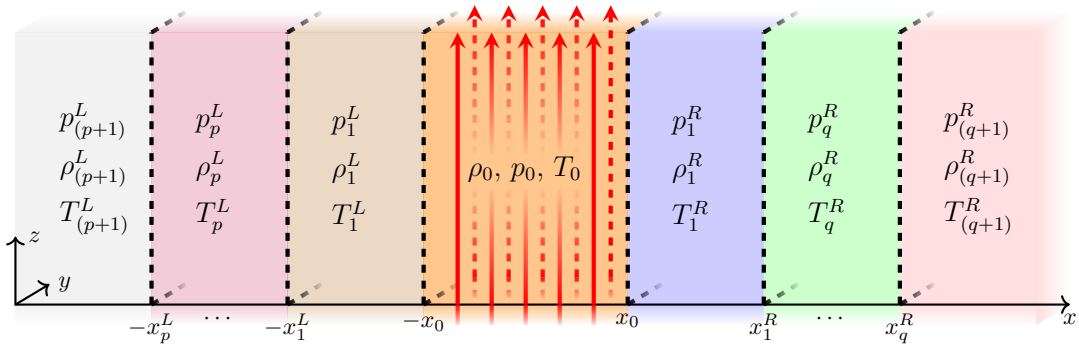

Figure 2.1: Equilibrium configuration of a layered plasma. The red arrows represent the vertical magnetic field, $B(x)\widehat{z}$. Kinetic pressure, $p_i^{L/R}$, density, $\rho_i^{L/R}$, and temperature, $T_i^{L/R}$ are equilibrium parameters. The subscript i corresponds to the relevant slab and varies from 1 to $p+1$ on the left side and from 1 to $q+1$ on the right side, where L/R corresponds to left/right.

Consider an infinite compressible inviscid static plasma embedded in a uniform and confined region $|x| \leq x_0$ with magnetic field $B(x)\ \widehat{\mathbf{z}}$, where

$$B(x) = \begin{cases} B_0, & |x| \leq x_0, \\ 0, & |x| > x_0. \end{cases}$$

The effect of gravity is ignored. Inside the magnetic slab, the equilibrium kinetic plasma pressure, density, and temperature are denoted by p_0, ρ_0, and T_0, respectively. $p_i^{L/R}$,

$\rho_i^{L/R}$, and $T_i^{L/R}$ denote the equilibrium kinetic pressure, density, and temperature inside the $i-$th slab on the left/right of the magnetic region with subscript i that varies from 1 to $p+1$ on the left side and from 1 to $q+1$ on the right. In total, there are $p+q+3$ regions, of which one has a magnetic field.

The equations that govern the perturbations within the magnetic slab are the ideal MHD equations:

$$\begin{aligned} \rho\frac{D\mathbf{v}}{Dt} &= -\nabla p - \frac{1}{\mu_0}\mathbf{B}\times(\nabla\times\mathbf{B}),\\ \frac{\partial\rho}{\partial t} + \nabla\cdot(\rho\mathbf{v}) &= 0,\\ \frac{D}{Dt}\left(\frac{p}{\rho^\gamma}\right) &= 0,\\ \frac{\partial\mathbf{B}}{\partial t} &= \nabla\times(\mathbf{v}\times\mathbf{B}), \end{aligned} \tag{2.1}$$

where μ_0 is the magnetic permeability of free space, γ is the adiabatic index, variables $\mathbf{v} = (v_x, v_y, v_z)$, $\mathbf{B}$, p, and ρ are velocity, magnetic field, kinetic pressure and density, at time t. After linearising and some algebra, we have

$$\begin{aligned} \left(\frac{\partial}{\partial t^2} - v_A^2\frac{\partial}{\partial z^2}\right)v_x &= \frac{\partial}{\partial x}\left(\left(c_0^2+v_A^2\right)\nabla\cdot\mathbf{v} - v_A^2\frac{\partial v_z}{\partial z}\right),\\ \left(\frac{\partial}{\partial t^2} - v_A^2\frac{\partial}{\partial z^2}\right)v_y &= \frac{\partial}{\partial y}\left(\left(c_0^2+v_A^2\right)\nabla\cdot\mathbf{v} - v_A^2\frac{\partial v_z}{\partial z}\right),\\ \frac{\partial^2 v_z}{\partial t^2} &= c_0^2\frac{\partial}{\partial z}\nabla\cdot\mathbf{v}. \end{aligned} \tag{2.2}$$

Here, $v_A = B_0/\sqrt{\mu_0\rho_0}$ is the Alfvén speed and $c_0 = \sqrt{\gamma p_0/\rho_0}$ is the sound speed in the magnetic slab. The sound speed in the $i-$th left/right non-magnetic region is denoted by $c_i^{L/R} = \sqrt{\gamma p_i^{L/R}/\rho_i^{L/R}}$. For the equilibrium conditions to be stable, the equilibrium pressure balance across each interface is required, *i.e.*

$$p^L_{(p+1)} = p^L_p = \ldots = p^L_1 = p_0 + \frac{B_0^2}{2\mu_0} = p^R_1 = \ldots = p^R_q = p^R_{(q+1)}. \tag{2.3}$$

Equation (2.3) yields to the following relation between characteristic speeds and density ratios for any two non-magnetic regions:

$$\frac{(c_i^{L/R})^2}{(c_j^{L/R})^2} = \frac{\rho_j^{L/R}}{\rho_i^{L/R}}.$$

We seek solution to Equations (2.2) of the following form:

$$v_x(\mathbf{x},t) = \widehat{v}_x(x)e^{i(kz-\omega t)},\ v_y(\mathbf{x},t) = 0,\ v_z(\mathbf{x},t) = \widehat{v}_z(x)e^{i(kz-\omega t)}, \tag{2.4}$$

representing wave propagation in the $\widehat{\mathbf{z}}$-direction, where ω is the angular frequency and k is the length of the wavenumber vector in the $\widehat{\mathbf{z}}$-direction. We only consider

field-aligned propagation of the perturbations. Substituting solutions (2.4) into the system of Equations (2.2), and combining the obtained equations, it is possible to derive an ordinary differential equation for $\widehat{v}_x$ representing transversal motions inside the magnetic slab, *i.e.* $\mid x \mid \leq x_0$:

$$\frac{d^2\widehat{v}_x}{dx^2} - m_0^2\widehat{v}_x = 0, \tag{2.5}$$

where

$$m_0^2 = \frac{(k^2v_A^2 - \omega^2)(k^2c_0^2 - \omega^2)}{(c_0^2 + v_A^2)(k^2c_T^2 - \omega^2)}, \quad c_T^2 = \frac{c_0^2v_A^2}{c_0^2 + v_A^2}. \tag{2.6}$$

Note that since $\mathbf{k} = (0, 0, k)$, and the system is homogeneous in the $y-$direction, the other transversal component of the motion (*i.e.* $\widehat{v}_y$) representing Alfvén waves decouples. For each of the left/right non-magnetic regions we obtain

$$\frac{d^2\widehat{v}_x}{dx^2} - (m_i^{L/R})^2\widehat{v}_x = 0, \tag{2.7}$$

with

$$(m_i^{L/R})^2 = k^2 - \frac{\omega^2}{(c_i^{L/R})^2}. \tag{2.8}$$

Equations (2.5) and (2.7) are formally identical to the corresponding equations for the symmetric slab, considered by Roberts (1981b), if $p = q = 0$ and $\rho_1^L = \rho_1^R = \rho_e$.

Let us assume that the perturbations vanish at infinity so that $\widehat{v}_x \to 0$ as $x \to \pm\infty$. It should be noted that m_0^2 and $(m_i^{L/R})^2$ may be positive or negative for i from 1 to p on the left side and from 1 to q on the right side. Taking into account that the wave amplitudes decay exponentially in the ambient, *i.e.* we are only dealing with trapped waves, we acquire a general solution of Equations (2.5) and (2.7) given by

$$\widehat{v}_x(x) = \begin{cases} A_{p+1}^L(\cosh m_{p+1}^L x + \sinh m_{p+1}^L x), & \text{for } x < -x_p^L, \\ A_p^L \cosh m_p^L x + B_p^L \sinh m_p^L x, & \text{for } -x_p^L < x < -x_{p-1}^L, \\ \dots & \\ A_1^L \cosh m_1^L x + B_1^L \sinh m_1^L x, & \text{for } -x_1^L < x < -x_0, \\ A_0 \cosh m_0 x + B_0 \sinh m_0 x, & \text{for } |x| \leq x_0, \\ A_1^R \cosh m_1^R x + B_1^R \sinh m_1^R x, & \text{for } x_0 < x < x_1^R, \\ \dots & \\ A_q^R \cosh m_q^R x + B_q^R \sinh m_q^R x, & \text{for } x_{q-1}^R < x < x_q^R, \\ A_{q+1}^R(\cosh m_{q+1}^R x - \sinh m_{q+1}^R x), & \text{for } x > x_q^R, \end{cases} \tag{2.9}$$

where A_i^L, B_j^L, A_s^R, B_t^R, A_0, and B_0, are constants with $i = 1, 2, \dots p+1$, $j = 1, 2, \dots p$, $s = 1, 2, \dots q+1$ and $t = 1, 2, \dots q$. The total (kinetic plus magnetic) pressure perturbation, $P_T(\mathbf{x}, t)$, satisfies the equation

$$\frac{\partial P_T}{\partial t} = \rho_0 v_A^2 \frac{\partial v_z}{\partial z} - \rho_0(c_0^2 + v_A^2)\nabla \cdot \mathbf{v}. \tag{2.10}$$

Considering $P_T(\mathbf{x},t)$ in a Fourier form, $P_T(\mathbf{x},t)=\widehat{p}(x)e^{i(kz-\omega t)}$, and employing Equations (2.2) and (2.10), we obtain that

$$\widehat{p}(x)=\widehat{v}_x'(x)\begin{cases}\Lambda^L_{p+1}/m^L_{p+1}, & \text{for } x<-x^L_p,\\ \Lambda^L_p/m^L_p, & \text{for } -x^L_p<x<-x^L_{p-1},\\ \dots & \\ \Lambda^L_1/m^L_1, & \text{for } -x_1<x<-x_0,\\ \Lambda_0/m_0, & \text{for } |x|\le x_0,\\ \Lambda^R_1/m^R_1, & \text{for } x_0<x<x^R_1,\\ \dots & \\ \Lambda^R_q/m^R_q, & \text{for } x^R_{q-1}<x<x^R_q,\\ \Lambda^R_{q+1}/m^R_{q+1}, & \text{for } x>x^R_q,,\end{cases} \tag{2.11}$$

where

$$\Lambda_0=-\frac{i\rho_0(k^2v_{\rm A}^2-\omega^2)}{m_0\omega},\quad \Lambda^L_j=\frac{i\rho^L_j\omega}{m^L_j},\quad \text{for}\quad j=1,2,\dots p+1,\quad \text{and}$$
$$\Lambda^R_l=\frac{i\rho^R_l\omega}{m^R_l},\quad \text{for}\quad l=1,2,\dots q+1. \tag{2.12}$$

Let us now establish appropriate boundary conditions. For physical solutions, the velocity, $v_x(\mathbf{x},t)$, and total pressure, $P_T(\mathbf{x},t)$, have to be continuous across the boundaries $x=-x^L_i$, $x=\pm x_0$ and $x=x^R_j$, for $i=1\dots p$ and $j=1\dots q$. Equations (2.9) and (2.11) give us $4+2(p+q)$ coupled homogeneous algebraic equations:

$$\begin{gathered}
A^L_{p+1}(\cosh m^L_{p+1}x^L_p-\sinh m^L_{p+1}x^L_p)=A^L_p\cosh m^L_px^L_p-B^L_p\sinh m^L_px^L_p,\\
\Lambda^L_{p+1}A^L_{p+1}(\cosh m^L_{p+1}x^L_p-\sinh m^L_{p+1}x^L_p)=\Lambda^L_p(B^L_p\cosh m^L_px^L_p-A^L_p\sinh m^L_px^L_p),\\
A^L_p\cosh m^L_px^L_{p-1}-B^L_p\sinh m^L_px^L_{p-1}=A^L_{p-1}\cosh m^L_{p-1}x^L_{p-1}-B^L_{p-1}\sinh m^L_{p-1}x^L_{p-1},\\
\Lambda^L_p(B^L_p\cosh m^L_px^L_{p-1}-A^L_p\sinh m^L_px^L_{p-1})=\\
=\Lambda^L_{p-1}(B^L_{p-1}\cosh m^L_{p-1}x^L_{p-1}-A^L_{p-1}\sinh m^L_{p-1}x^L_{p-1}),\\
\dots\\
A^L_1\cosh m^L_1x_0-B^L_1\sinh m^L_1x_0=A_0\cosh m_0x_0-B_0\sinh m_0x_0,\\
\Lambda^L_1(B^L_1\cosh m^L_1x_0-A^L_1\sinh m^L_1x_0)=\Lambda_0(B_0\cosh m_0x_0-A_0\sinh m_0x_0),\\
A_0\cosh m_0x_0+B_0\sinh m_0x_0=A^R_1\cosh m^R_1x_0+B^R_1\sinh m^R_1x_0\\
\Lambda_0(A_0\sinh m_0x_0+B_0\cosh m_0x_0))=\Lambda^R_1(A^R_1\sinh m^R_1x_0+B^R_1\cosh m^R_1x_0),\\
\dots\\
A^R_{q-1}\cosh m^R_{q-1}x^R_{q-1}+B^R_{q-1}\sinh m^R_{q-1}x^R_{q-1}=A^R_q\cosh m^R_qx^R_{q-1}+B^R_q\sinh m^R_qx^R_{q-1},\\
\Lambda^R_{q-1}(A^R_{q-1}\sinh m^R_{q-1}x^R_{q-1}+B^R_{q-1}\cosh m^R_{q-1}x^R_{q-1})=\Lambda^R_q(A^R_q\sinh m^R_qx^R_{q-1}+B^R_q\cosh m^R_qx^R_{q-1}),\\
A^R_q\cosh m^R_qx^R_q+B^R_q\sinh m^R_qx^R_q=A^R_{q+1}(\cosh m^R_{q+1}x^R_q-\sinh m^R_{q+1}x^R_q),\\
\Lambda^R_q(A^R_q\sinh m^R_qx^R_q+B^R_q\cosh m^R_qx^R_q)=\Lambda^R_{q+1}A^R_{q+1}(\sinh m^R_{q+1}x^R_q-\cosh m^R_{q+1}x^R_q).
\end{gathered} \tag{2.13}$$

Here, $A_i^{L/R}$ are constant with respect to x. We now rewrite the above equations into the following compact matrix form:

$$\mathbf{M}\left(A_{p+1}^L,\ A_p^L,\ B_p^L,\ \ldots\ A_1^L,\ B_1^L,\ A_0,\ B_0,\ A_1^R,\ B_1^R,\ \ldots\ A_q^R,\ B_q^R,\ A_{q+1}^R\right)^T = \mathbf{0}, \tag{2.14}$$

where $\mathbf{M}$ is a $[4+2(p+q)] \times [4+2(p+q)]$ matrix. The precise form of the matrix $\mathbf{M}$ is given by Equations (A.1-A.6) in Appendix A.

In order to have a non-trivial solution of the system, the determinant of the matrix $\mathbf{M}$ must be equal to zero:

$$\det \mathbf{M} = 0. \tag{2.15}$$

Equation (2.15) is the dispersion relation of the multi-layer system. In general, unlike the symmetric case studied *e.g.* by Roberts (1981b), the dispersion relation Equation (2.15) cannot be decoupled into two equations that correspond to the well-known sausage (oscillations at the slab boundaries in anti-phase, that correspond mathematically to the equation containing $\tanh m_0 x_0$) and kink (perturbations of the slab boundaries oscillating in-phase that correspond to the equation with $\coth m_0 x_0$) MHD waves. Solutions to Equation (2.15) will provide modes modified by the density difference at the sides of the magnetic slab similar to a single asymmetric slab investigated by Allcock and Erdélyi (2017). We adopt the notions of quasi-sausage and quasi-kink to describe these eigenmodes, because they have mixed characters. The slab cross-sectional width, that is constant for symmetric kink modes, is affected for asymmetric kink modes and the line of zero perturbation is shifted for asymmetric sausage modes when compared to the symmetric case, namely, the center of the slab. Furthermore, both the sausage and kink modes can be further categorised as body and surface modes. Surface waves exist when $m_0^2 > 0$ which corresponds to evanescent solutions of Equation (2.5), while body waves exist when $m_0^2 < 0$ which corresponds to spatially oscillatory solutions. This nomenclature for wave classification was introduced by Roberts (1981b) for symmetric and Allcock and Erdélyi (2017) for asymmetric equilibria.

Let us now consider some specific cases of an asymmetric multi-layered plasma slab structure that are analytically solvable and have potential for solar application. First, by setting $p = q = 0$, we verify that the dispersion relation reduces to that which governs the asymmetric slab configuration of Allcock and Erdélyi (2017), namely

$$\tanh 2m_0 x_0 \left(\Lambda_0 \Lambda_0 + \Lambda_1^L \Lambda_1^R\right) + \Lambda_0 \left(\Lambda_1^L + \Lambda_1^R\right) = 0. \tag{2.16}$$

We will now focus on cases of two layers (one magnetic and one non-magnetic), and three (a magnetic layer sandwiched between two non-magnetic) slabs, respectively, and investigate how the multi-layered structure affects the eigenmodes and their eigenfunctions.

Two-slab case

Let us first consider the case of two slabs, represented by $p = 1$ and $q = 0$, which is illustrated by Figure 2.2. The width of the non-magnetic and magnetic slabs are

denoted as d_1^L and d_0, respectively. Such a model could be useful for modelling MHD waves in magnetic bright points (MBP) of the solar photosphere (as shown on Figure 2.3). MBPs are approximately vertical magnetic structures between supergranule convection cells of different densities and temperatures. Since neighbouring granular cells affect the MBP, we can apply a two-slab description to analyse what will change when comparing eigenmodes to MHD waves in a single-slab case.

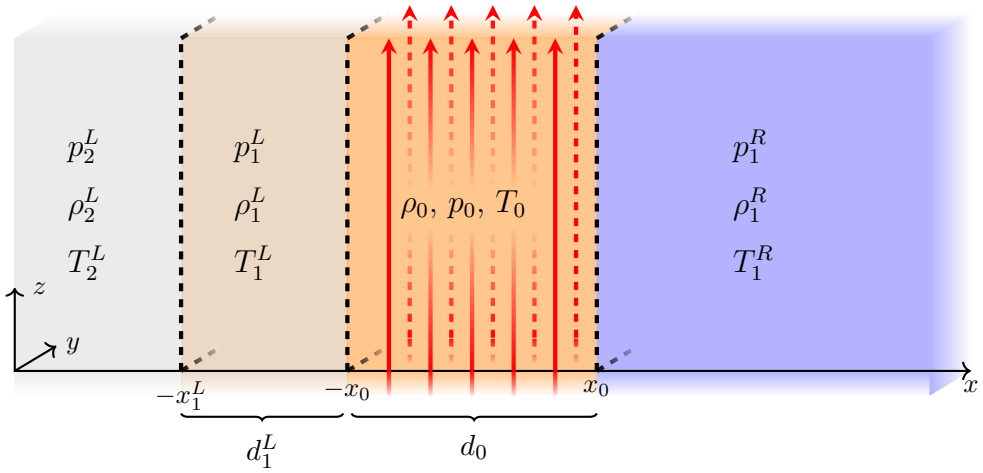

Figure 2.2: Equilibrium configuration for a two-slab case: a magnetic slab, $|x| \leq x_0$, and a non-magnetic slab, $-x_1^L \leq x \leq -x_0$.

From condition (2.15), we obtain the dispersion relation

$$\left[\Lambda_0\Lambda_0\left(\Lambda_1^L - \Lambda_2^L \tanh m_1^L(x_0 - x_1^L)\right) + \Lambda_1^L\Lambda_1^R\left(\Lambda_2^L - \Lambda_1^L \tanh m_1^L\left(x_0 - x_1^L\right)\right)\right] \times$$
$$\times \tanh 2m_0x_0 + \Lambda_0\left[\Lambda_1^L\left(\Lambda_1^R + \Lambda_2^L\right) - \left(\Lambda_1^L\Lambda_1^L + \Lambda_1^R\Lambda_2^L\right)\tanh m_1^L\left(x_0 - x_1^L\right)\right] = 0. \tag{2.17}$$

Note, that the two-slab case may be reduced to the single slab case, by letting $x_0 = x_1^L$ and $\Lambda_1^L = \Lambda_2^L$. By substituting notations introduced by Equation (2.12) into the dispersion relation (2.17), we obtain

$$\tanh 2m_0x_0\left[\omega^4\frac{m_0^2}{\rho_0^2} + \frac{m_1^R}{\rho_1^R}\frac{m_2^L}{\rho_2^L}\left(k^2v_A^2 - \omega^2\right)^2 - \right.$$
$$\left.\left(\frac{m_1^L}{\rho_1^L}\frac{m_1^R}{\rho_1^R}\left(k^2v_A^2 - \omega^2\right)^2 + \frac{m_0^2}{\rho_0^2}\omega^4\frac{\rho_1^L}{m_1^L}\frac{m_2^L}{\rho_2^L}\right)\tanh m_1^L\left(x_0 - x_1^L\right)\right] - \frac{m_0}{\rho_0}\omega^2 \times$$
$$\times\left(k^2v_A^2 - \omega^2\right)\left(\frac{m_1^R}{\rho_1^R} + \frac{m_2^L}{\rho_2^L} - \left(\frac{m_1^R}{\rho_1^R}\frac{m_2^L}{\rho_2^L}\frac{\rho_1^L}{m_1^L} + \frac{m_1^L}{\rho_1^L}\right)\tanh m_1^L\left(x_0 - x_1^L\right)\right) = 0. \tag{2.18}$$

Equation (2.18) is the dispersion relation describing the propagation of quasi-kink and quasi-sausage waves for the case of two (one magnetic and one non-magnetic) slabs.

Next, let us plot the eigenfunctions using numerical solutions. In Figure 2.4a, the effect of varying the density ratios ρ_1^L/ρ_0 and ρ_2^L/ρ_1^L is shown, and its cross-cut slice is

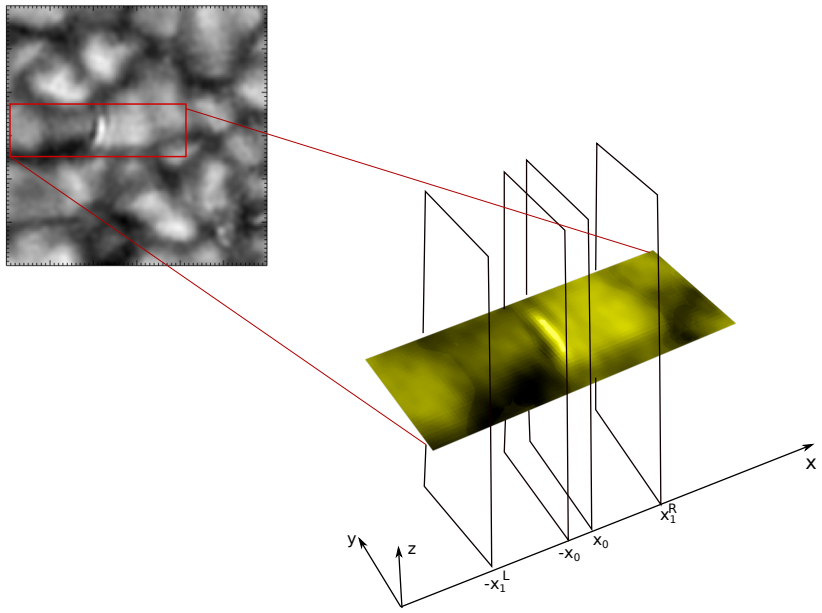

Figure 2.3: Asymmetric multi-slab approximation for an elongated MBP, based on Figure 11 of Liu et al. (2018), observed by the New Vacuum Solar Telescope in TiO 7058 Å.

plotted in Figure 2.4b for a characteristic value of the ratio $\rho_2^L/\rho_0 = 0.3$. The panels of Figure 2.4c illustrate the behaviour of slow surface quasi-kink and quasi-sausage modes, in a two-slab system using numerical solutions for the dispersion relation Equation (2.18) for $\rho_1^L/\rho_0 = 1, 2, 3$. The central plot shows the case where $\rho_1^L = \rho_1^R$. The density ratio is $\rho_1^R/\rho_0 = 2$, the characteristic speed orderings are $c_1^R = 0.7c_0$, $v_A = 0.4c_0$, the non-dimensional width of the magnetic slab is $kx_0 = 1.5$ and the width of the non-magnetic slab is $x_1^L = 2x_0$.

Two important features are notable when inspecting the eigenfunctions of Figure 2.4c. First, although the eigenfunctions themselves are continuous, this is not the case for their derivatives, which are discontinuous at the interfaces. Assuming a suitable spatial resolution of linear perturbations during an observation of structured MHD waveguides, the spatial distribution of the eigenfunctions (say transversal velocity, intensity, or the appropriate component of the magnetic field) could be measured and the above discontinuous feature confirmed. In order to resolve discontinuities of the transversal velocity perturbation at the interfaces of size around Mm, as shown in Figure 2.4c, the Doppler shift measurements could be used and spatial resolution around 250 km is needed.

Now, from the measured spatial distribution of these eigenfunctions, one may then determine the details of the structuring of the MHD waveguide by means of SMS.

Second, the amplitudes of the perturbations themselves at the boundaries of an

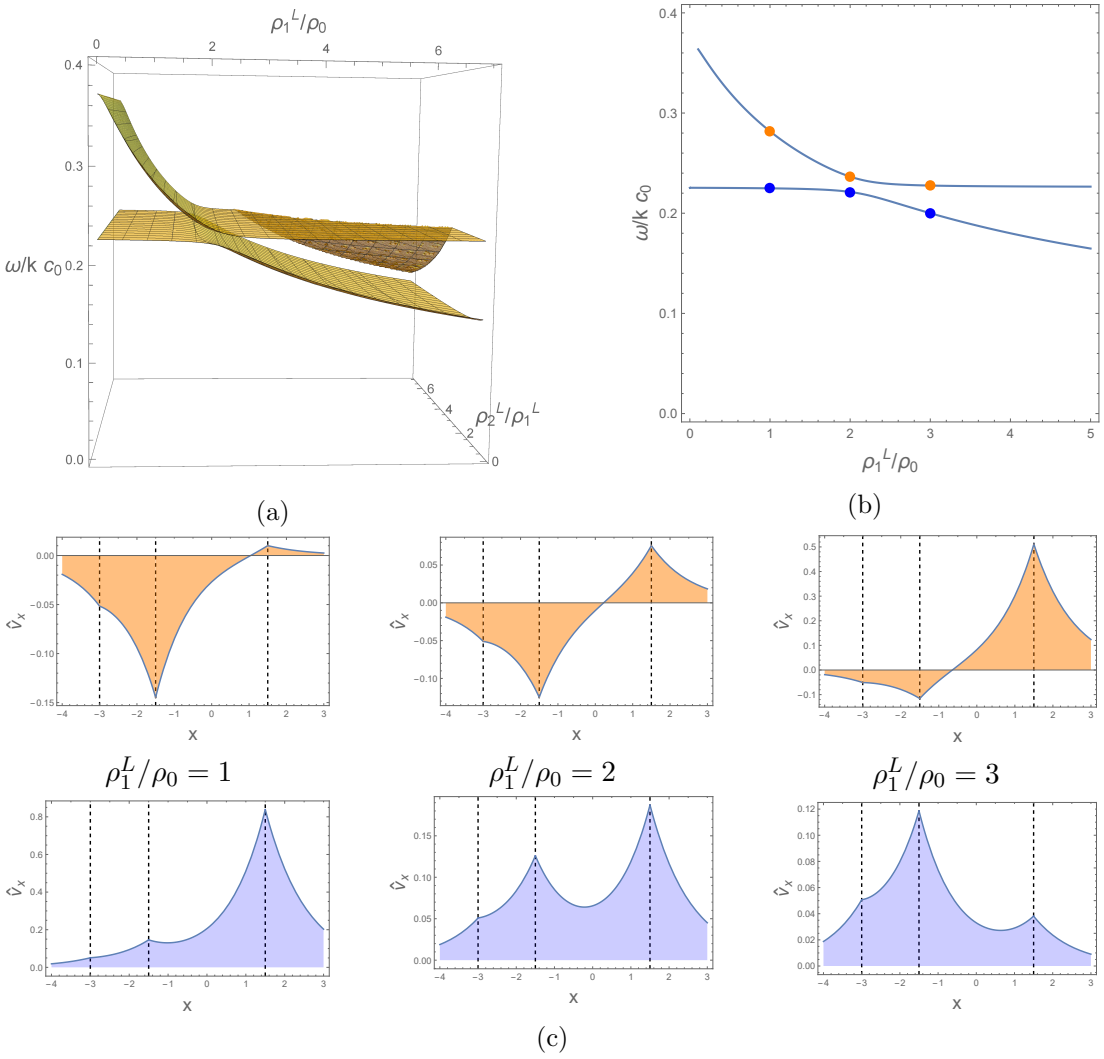

Figure 2.4: (a) Slow surface mode solutions of the dispersion relation (2.18) showing the effect of varying the density ratios ρ_1^L/ρ_0 and ρ_2^L/ρ_1^L. Panel (b) is a cross-cut of panel (a) for $\rho_2^L/\rho_0 = 0.3$. Distributions of the transverse velocity perturbation, $\widehat{v}_x$, for given density ratios are plotted on panels (c). Here, the other density ratio is fixed at $\rho_1^R/\rho_0 = 2$. The characteristic speed ordering is $c_1^R = 0.7c_0$, $v_A = 0.4c_0$, the width of the non-dimensional magnetic slab is $kx_0 = 1.5$, and $x_1^L = 2x_0$. The orange (blue) dots in panel (b) corresponds to the quasi-sausage (quasi-kink) mode. The parameters at each blue and orange dot are used to plot the distribution of the transverse velocity perturbation. The upper (lower) rows in panels (c) correspond to the quasi-sausage (quasi-kink) mode solutions corresponding to density ratios $\rho_1^L/\rho_0 = 1$, 2, and 3.

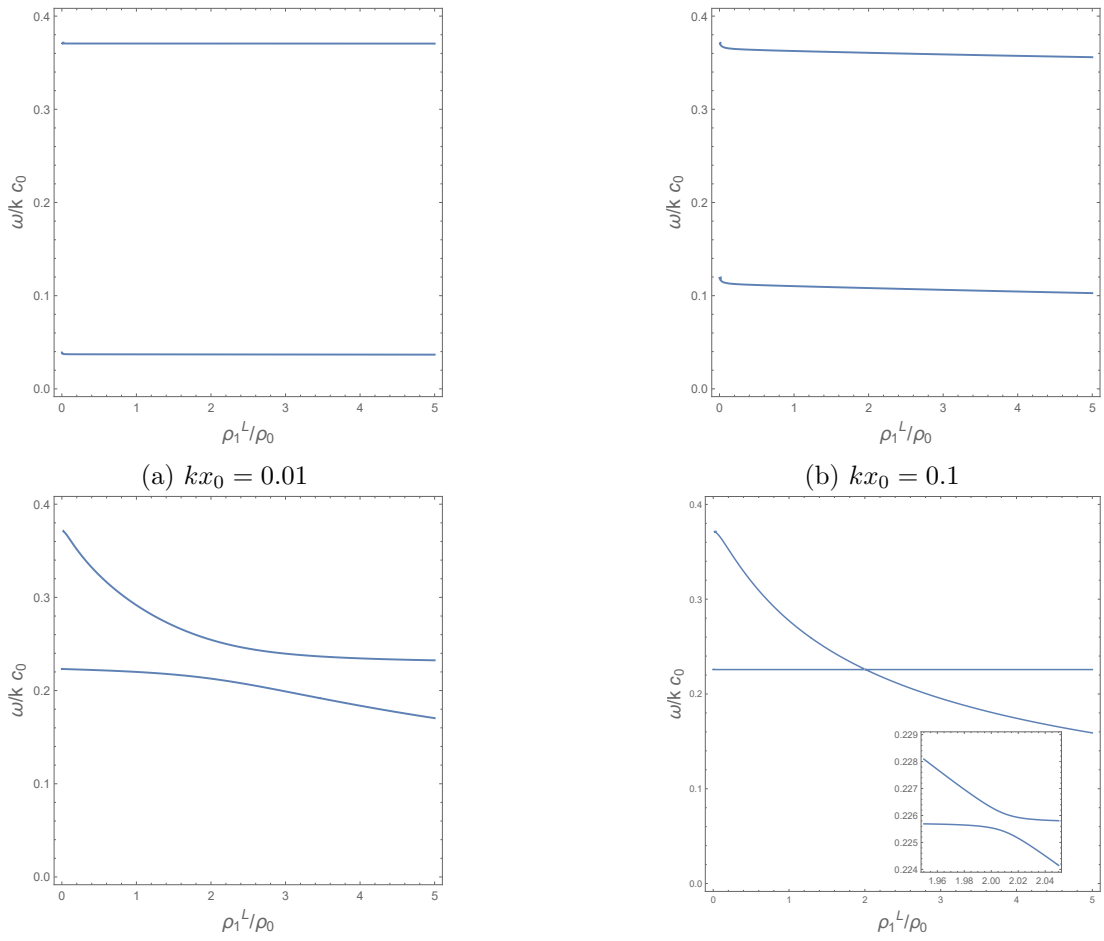

(a) $kx_0 = 0.01$ (b) $kx_0 = 0.1$

(c) $kx_0 = 1$ (d) $kx_0 = 3$

Figure 2.5: Dependence on the ratio of non-magnetic slab density to the magnetic slab density is shown in panels (a) - (d) for typical values of non-dimensional magnetic slab width $kx_0 = 0.01$, 0.1, 1, and 3. The characteristic speed orderings are $c_1^R = 0.7c_0$ and $v_A = 0.4c_0$, the width of the non-magnetic slab is $x_1^L = 2x_0$, and the density ratios take values are $\rho_2^L/\rho_0 = 0.3$ and $\rho_1^R/\rho_0 = 2$.

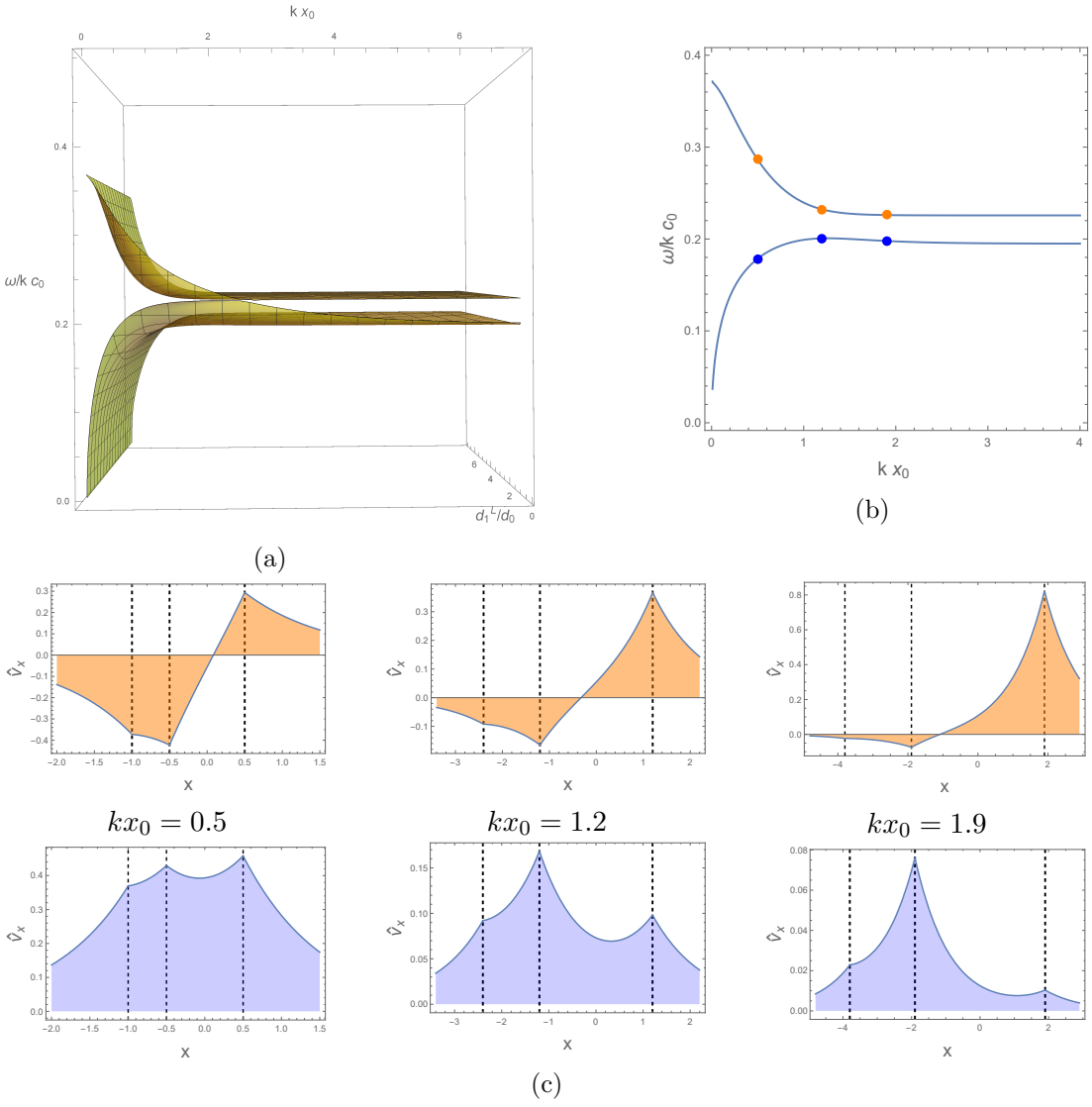

Figure 2.6: Same as Figure 2.4, but (a) shows slow surface mode solutions of the dispersion relation (2.18) emphasising the effect of varying the ratio of non-magnetic slab width d_1^L to magnetic slab width d_0. Panel (b) is a cross-cut of panel (a) for $d_1^L/d_0 = 0.5$ In panels (c), distributions of the transverse velocity perturbation $\widehat{v}_x$ as the ratio of non-dimensional magnetic slab width kx_0 are plotted. The density ratios are fixed at $\rho_1^R/\rho_0 = 2$, $\rho_1^L/\rho_0 = 3$, and $\rho_2^L/\rho_0 = 0.3$. The characteristic speed orderings are $c_1^R = 0.7c_0$ and $v_A = 0.4c_0$, and the non-magnetic slab width is $x_1^L = 2x_0$.

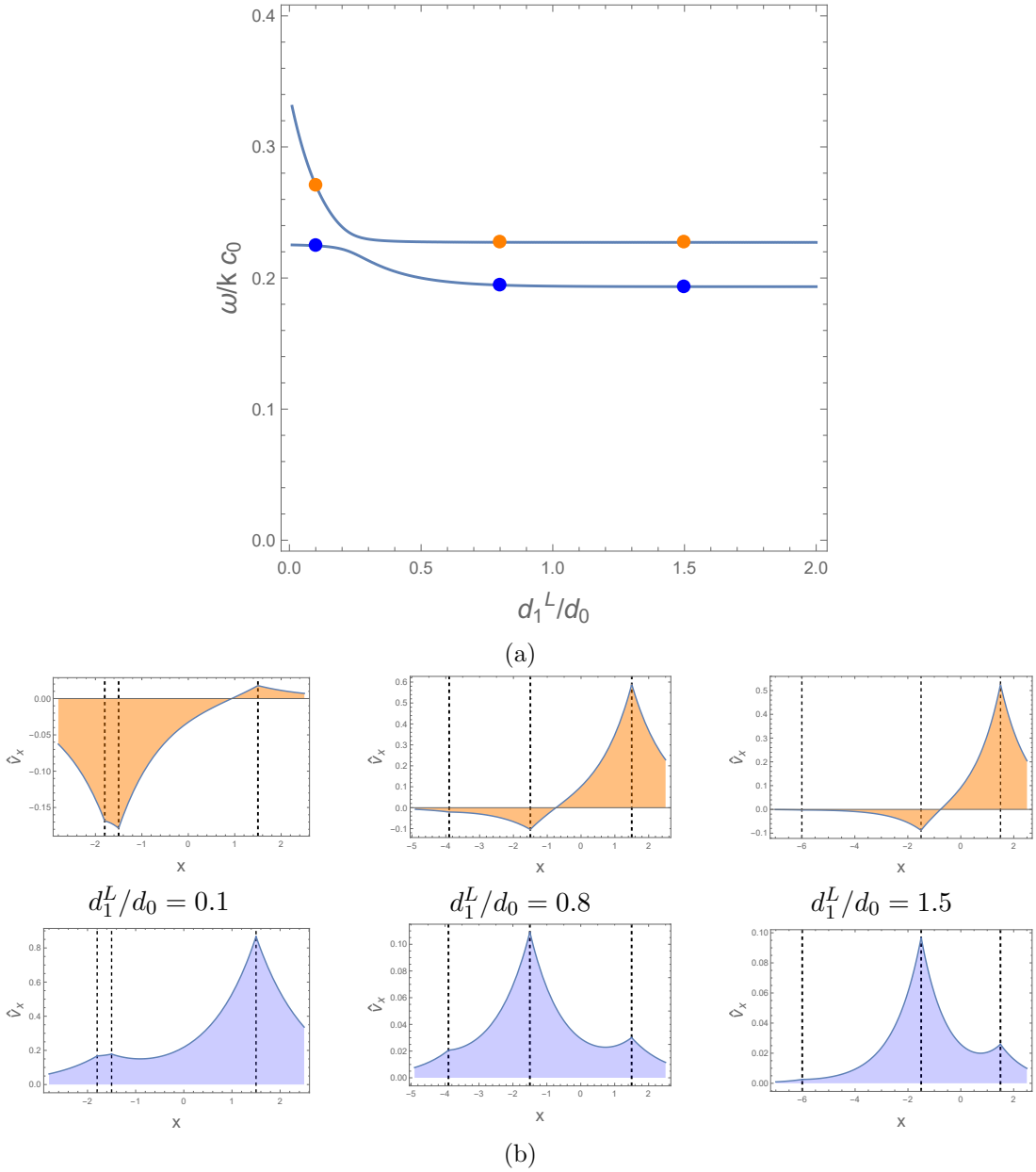

Figure 2.7: Same as Fig 2.4, but the density ratio are now fixed at $\rho_1^R/\rho_0 = 2$, $\rho_1^L/\rho_0 = 3$, and $\rho_2^L/\rho_0 = 0.3$ and non-dimensional magnetic slab width is $kx_0 = 1.5$. The characteristic speed orderings are $c_1^R = 0.7c_0$ and $v_A = 0.4c_0$. In panel (b), distributions of the transverse velocity perturbation, $\widehat{v}_x$, for a specific value of the ratio of non-magnetic slab width d_1^L to magnetic slab width d_0 are plotted. The upper (lower) row in panel (b) corresponds to the quasi-sausage (quasi-kink) mode solutions.

asymmetric structured waveguide will not be symmetric with respect to the center of the magnetic waveguide. This information could also be exploited to determine the equilibrium parameters of the MHD waveguide structure, however, that is beyond the scope of the current chapter. For an analogue of how the concept works for a single asymmetric waveguide, see Allcock and Erdélyi (2018).

Figures 2.5a - 2.5d reveal the behaviour of the slow surface modes as the non-magnetic slab density is varied with $kx_0 = 0.01, 0.1$, and 3. For a wide slab width $kx_0 \gg 1$, the phenomenon of *avoided crossing* is visualised in Figure 2.5d. It happens between phase speed of quasi-sausage and quasi-kink modes. The main idea of it is that the loci of the eigenvalues of the slow surface modes do not intersect, because system parameters doesn't allow phase speeds to be equal to each other. It demonstrates why the dispersion relation Equation (2.18) does not decouple into two equations for sausage and kink modes, as it does in the symmetric case. For more on the meaning of avoided crossings of eigenmodes in the present context, see Allcock and Erdélyi (2017). The density ratios are fixed at $\rho_2^L/\rho_0 = 0.3$, $\rho_1^R/\rho_0 = 2$, the characteristic speed orderings are $c_1^R = 0.7c_0$, $v_A = 0.4c_0$ and the width of the non-magnetic slab is $x_1^L = 2x_0$.

In Figure 2.6a, the effect of varying the non-dimensional magnetic slab width kx_0 and the ratio d_1^L/d_0 is illustrated. For a characteristic value of the ratio of non-magnetic slab width to magnetic slab width $d_1^L/d_0 = 0.5$, a cross-cut of Figure 2.6a is plotted in Figure 2.6b, and for a specific value of non-dimensional magnetic slab $kx_0 = 1.5$ in Figure 2.7a. The panels in Figure 2.6c and Figure 2.7b show the slow surface quasi-sausage and quasi-kink modes for different values of the non-dimensional magnetic slab width $kx_0 = 0.5, 1.2, 1.9$ and the ratio $d_1^L/d_0 = 0.1, 0.8, 1.5$, respectively. The density ratios are fixed at $\rho_2^L/\rho_0 = 0.3$, $\rho_1^L/\rho_0 = 3$, and $\rho_1^R/\rho_0 = 2$ and the characteristic speed orderings are $c_1^R = 0.7c_0$ and $v_A = 0.4c_0$.

Three-slab case

Let us now move on to study the three-slab case as a generalisation of the two-slab configuration, to better model *e.g.* MBPs. It could help to understand how consideration of a set of multiple granular cells may influence oscillations in MBPs. The case of three adjacent slabs is established when $p = q = 1$ and is visualised in Figure 2.8, where the widths of the left non-magnetic slab and right magnetic slab are denoted by $d_1^{L/R}$ and d_0, respectively. The dispersion relation in this case takes the form:

$$\begin{aligned}
&\tanh 2m_0x_0\left(\Lambda_0\Lambda_0\left(\Lambda_1^L-\Lambda_2^L\tanh m_1^L(x_0-x_1^L)\right)\left(\Lambda_1^R-\Lambda_2^R\tanh m_1^R(x_0-x_1^R)\right)+\right.\\
&+\Lambda_1^L\Lambda_1^R\left(\Lambda_2^L-\Lambda_1^L\tanh m_1^L\left(x_0-x_1^L\right)\right)\left(\Lambda_2^R-\Lambda_1^R\tanh m_1^R\left(x_0-x_1^R\right)\right)\Big)\\
&+\Lambda_0\left(\Lambda_1^L\Lambda_1^R\left(\Lambda_2^L+\Lambda_2^R\right)-\Lambda_1^L\left(\Lambda_1^R\Lambda_1^R+\Lambda_2^L\Lambda_2^R\right)\tanh m_1^R\left(x_0-x_1^R\right)-\right.\\
&-\Lambda_1^R\left(\Lambda_1^L\Lambda_1^L+\Lambda_2^L\Lambda_2^R\right)\tanh m_1^L\left(x_0-x_1^L\right)\\
&\left.+\left(\Lambda_1^L\Lambda_1^L\Lambda_2^R+\Lambda_1^R\Lambda_1^R\Lambda_2^L\right)\tanh m_1^L\left(x_0-x_1^L\right)\tanh m_1^R\left(x_0-x_1^R\right)\right)=0. \qquad (2.19)
\end{aligned}$$

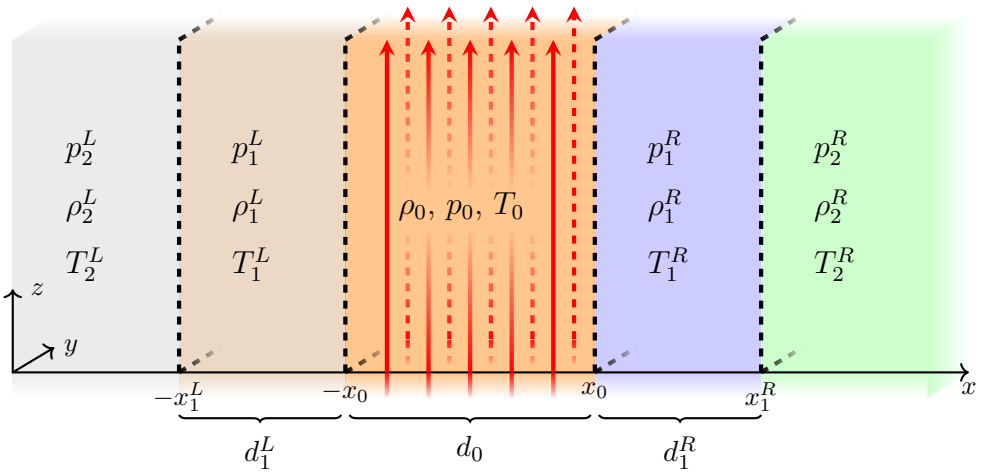

Figure 2.8: Equilibrium configuration for the three-slab case. A magnetic slab at $|x| \leq x_0$ is sandwiched between two non-magnetic slabs at $-x_1^L \leq x \leq -x_0$ and $x_0 \leq x \leq x_1^R$.

Substituting back the notations of (2.12), we arrive at

$$\tanh 2m_0x_0\left(\omega^4\frac{m_0^2}{\rho_0^2}\left(\frac{m_1^L}{\rho_1^L}-\frac{m_2^L}{\rho_2^L}\tanh m_1^L\left(x_0-x_1^L\right)\right)\left(\frac{m_1^R}{\rho_1^R}-\frac{m_2^R}{\rho_2^R}\right.\right.$$
$$\left.\tanh m_1^R\left(x_0-x_1^R\right)\right)+\frac{m_1^L}{\rho_1^L}\frac{m_1^R}{\rho_1^R}\left(k^2v_A^2-\omega^2\right)^2\left(\frac{m_2^L}{\rho_2^L}-\frac{m_1^L}{\rho_1^L}\tanh m_1^L\left(x_0-x_1^L\right)\right)$$
$$\left.\left(\frac{m_2^R}{\rho_2^R}-\frac{m_1^R}{\rho_1^R}\tanh m_1^R\left(x_0-x_1^R\right)\right)\right)-\frac{m_0}{\rho_0}\omega^2\left(k^2v_A^2-\omega^2\right)\left(\frac{m_1^L}{\rho_1^L}\left(\frac{m_1^R}{\rho_1^R}\frac{m_2^R}{\rho_2^R}+\frac{m_1^R}{\rho_1^R}\frac{m_2^L}{\rho_2^L}\right.\right.$$
$$\left.-\left(\frac{m_2^L}{\rho_2^L}\frac{m_2^R}{\rho_2^R}+\left(\frac{m_1^R}{\rho_1^R}\right)^2\right)\tanh m_1^R\left(x_0-x_1^R\right)\right)-\tanh m_1^L\left(x_0-x_1^L\right)\left(\frac{m_1^R}{\rho_1^R}\left(\frac{m_1^L}{\rho_1^L}\right)^2\right.$$
$$\left.\left.+\frac{m_1^R}{\rho_1^R}\frac{m_2^L}{\rho_2^L}\frac{m_2^R}{\rho_2^R}-\left(\left(\frac{m_1^L}{\rho_1^L}\right)^2\frac{m_2^R}{\rho_2^R}+\left(\frac{m_1^R}{\rho_1^R}\right)^2\frac{m_2^L}{\rho_2^L}\right)\tanh m_1^R\left(x_0-x_1^R\right)\right)\right)=0. \quad (2.20)$$

Equation (2.20) is the dispersion relation for the three-slab case with one magnetic slab embedded between two non-magnetic plasma slabs with different equilibrium parameters. It was shown by Roberts (1981b), that the dispersion relation governing wave propagation in the case of a single symmetric slab consists of two decoupled equations, describing sausage and kink MHD waves. For the two- and three-slab cases, similarly to the one-slab asymmetric case, the dispersion relation is a single equation, which describes the propagation of quasi-kink and quasi-sausage waves.

In the symmetric case, where $\rho_1^L = \rho_1^R = \rho_1$ and $\rho_2^L = \rho_2^R = \rho_2$, the dispersion relation (2.20) decouples into two equations, one with tanh (sausage mode) and one

with coth (kink mode):

$$\frac{\rho_1}{\rho_0}\omega^2 m_0 \left(m_1\rho_2 - m_2\rho_1 \tanh m_1 (x_0 - x_1)\right) \begin{pmatrix} \tanh m_0 x_0 \\ \coth m_0 x_0 \end{pmatrix} = \\ = m_1 \left(k^2 v_A^2 - \omega^2\right) \left(m_2\rho_1 - m_1\rho_2 \tanh m_1 (x_0 - x_1)\right). \tag{2.21}$$

§ 2.2 Analytical solutions

Let us now consider the analytical examination of the dispersion relations (2.18) and (2.20) under the incompressible and thin-slab approximations.

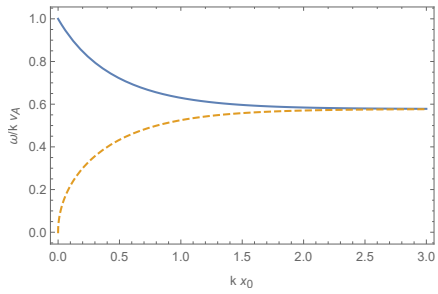

(a) $R_2^L = R_1^L = R_1^R = 2$

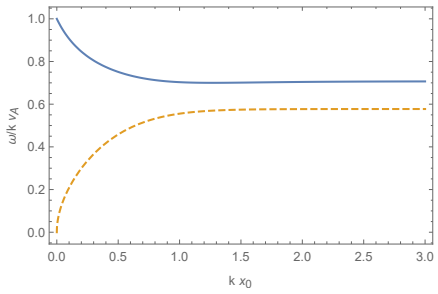

(b) $R_2^L = 3$, $R_1^L = 1$, $R_1^R = 2$

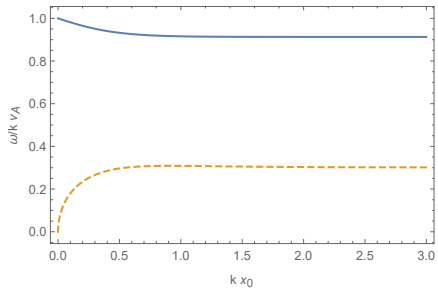

(c) $R_2^L = 5$, $R_1^L = 10$, $R_1^R = 0.2$

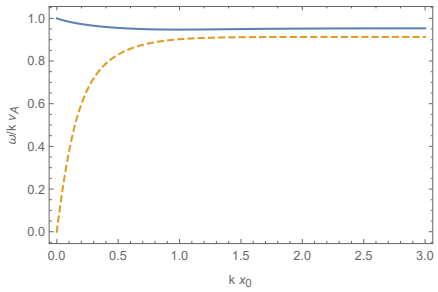

(d) $R_2^L = 100$, $R_1^L = 0.1$, $R_1^R = 0.2$

Figure 2.9: The dispersion of MHD modes in an incompressible multi-layered symmetric (a) and asymmetric slab (b) - (d) system ($p = 1$, $q = 0$, $x_1^L = 2x_0$). Plotted are the two sub-Alfvénic surface modes for different densities ratios $R_i^{L/R} = \rho_i^{L/R}/\rho_0$ for the two-slab case.

2.2.1 Spurious Solutions

It is obvious that $\omega = k^2 v_A^2$ is an exact solution of both of the dispersion relations (2.18) and (2.20). However, for this solution, $m_0 = 0$, which leads to a linear solution of the governing differential equation (2.5), and not to exponential or oscillatory solution. Hence, this solution is considered to be spurious. The same is true for the solutions

$\omega = kc_0$ and $\omega = kc_T$. So, there are no global modes with a finite wave number with phase-speed c_T, c_0, or v_A.

2.2.2 Incompressible approximation

Magnetoacoustic modes in the incompressible limit arise only from slow modes, *i.e.* modes with speed less than v_A, in the given equilibrium and choice of field-aligned propagation. In general, it is not possible to solve the dispersion relations (2.18) and (2.20) analytically, but the incompressible approximation simplifies it significantly and allows us to find an analytical solution. Therefore, we focus on other effects than compressibility. Let us examine the dispersion relations (2.18) and (2.20) in the limit $\gamma \to \infty$, where γ is the adiabatic index, corresponding to the approximation of an incompressible plasma. In this limit, we obtain $c_T \to v_A$, hence $m_0 \to k$, $m_i^L \to k$ and $m_j^R \to k$.

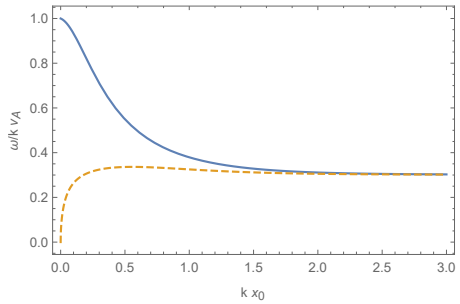

(a) $R_2^L = R_2^R = 0.5$, $R_1^L = R_1^R = 10$

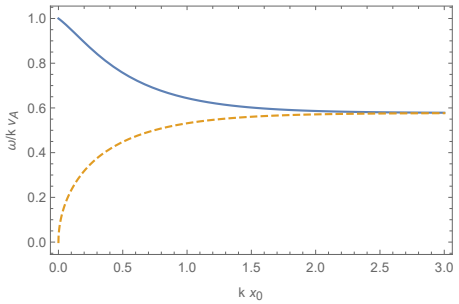

(b) $R_2^L = 3$, $R_1^L = R_1^R = 2$, $R_2^R = 0.5$

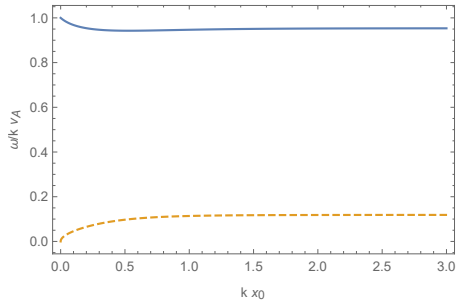

(c) $R_2^L = 100$, $R_1^L = 70$, $R_1^R = 0.1$, $R_2^R = 0.5$

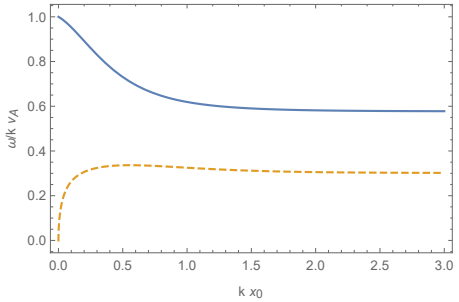

(d) $R_2^L = 0.5$, $R_1^L = 2$, $R_1^R = 10$, $R_2^R = 1$

Figure 2.10: Solutions to the dispersion relation (2.25) of the modes in an incompressible symmetric (a) and asymmetric (b) - (d) slab for the case of a magnetic slab embedded between two non-magnetic asymmetric slabs, all in an asymmetric plasma environment, with $p = 1$, $q = 1$, and $x_1^L = x_1^R = 2x_0$.

Two-slab case

First, let us study the two-slab case. Here, applying the incompressible approximation, the dispersion relation (2.18) becomes

$$\tanh 2kx_0 \left(\frac{\omega^4}{\rho_0^2} + \frac{(k^2 v_A^2 - \omega^2)^2}{\rho_1^R \rho_2^L} - \left(\frac{(k^2 v_A^2 - \omega^2)^2}{\rho_1^L \rho_1^R} + \frac{\omega^4}{\rho_0^2} \frac{\rho_1^L}{\rho_2^L} \right) \tanh k(x_0 - x_1^L) \right) - \frac{\omega^2}{\rho_0} \left(k^2 v_A^2 - \omega^2 \right) \left(\frac{1}{\rho_1^R} + \frac{1}{\rho_2^L} - \left(\frac{\rho_1^L}{\rho_1^R \rho_2^L} + \frac{1}{\rho_1^L} \right) \tanh k(x_0 - x_1^L) \right) = 0. \quad (2.22)$$

Equation (2.22) is quadratic in ω^2, so we can solve it in a closed form. Its solutions are

$$\omega^2 = \frac{1}{2} k^2 v_A^2 \left(\frac{\sigma + 2\rho_0 \coth kx_0 \left(\rho_1^L - \rho_2^L \tanh k(x_0 - x_1^L) \right) \pm \sqrt{\varsigma}}{\sigma + 2\frac{\rho_1^L \rho_1^R}{\rho_0} \coth kx_0 \left(\rho_2^L - \rho_1^L \tanh k(x_0 - x_1^L) \right)} \right), \quad (2.23)$$

with

$$\begin{aligned} \sigma &= \rho_1^L \left(\rho_1^R + \rho_2^L + 2\rho_0 \coth kx_0 + \left(\rho_1^R + \rho_2^L \right) \coth {kx_0}^2 \right) - \\ &- (\coth {kx_0}^2 - 1) \left(\left(\rho_1^L \rho_1^L + \rho_1^R \rho_2^L \right) \cosh 2kx_0 + \rho_0 \rho_2^L \sinh 2kx_0 \right) \tanh k(x_0 - x_1^L), \\ \varsigma &= \left(\rho_1^L \left(\rho_1^R + \rho_2^L \right) - \left(\rho_1^L \rho_1^L + \rho_1^R \rho_2^L \right) \tanh k(x_0 - x_1^L) \right)^2 \left(\coth^2 kx_0 - 1 \right)^2 + \\ &+ 4 \coth^2 kx_0 \left(\rho_1^L \left(\rho_1^R - \rho_2^L \right) + \left(\rho_1^L \rho_1^L - \rho_1^R \rho_2^L \right) \tanh k(x_0 - x_1^L) \right)^2 . \end{aligned} \quad (2.24)$$

The solutions given by Eq. (2.23) are surface waves with sub-Alfvénic phase-speeds.

We introduce the following notation $R_i^{L/R} = \rho_i^{L/R}/\rho_0$. Figure 2.9a shows the dispersion behaviour of two sub-Alfvénic surface modes in one symmetric slab for density ratios $R_2^L = R_1^L = R_1^R = 2$. Figs. 2.9b - 2.9d illustrate that, in the incompressible approximation, the phase speed of the modes approach either the Alfvén speed or zero in the long-wavelength limit. However, when $k \to \infty$, and depending on the external densities, the phase speeds converge to different speeds. Further, when $R_i^L \approx R_i^R$ the converged speeds are almost identical. For Figure 2.9b, the density ratios are $R_2^L = 3, R_1^L = 1$, and $R_1^R = 2$, for Figure 2.9c density ratios are $R_2^L = 5, R_1^L = 10$, and $R_1^R = 0.2$, and in Figure 2.9d $R_2^L = 100, R_1^L = 0.1$, and $R_1^R = 0.2$.

Three-slab case

Similar to the two-slab case, from the dispersion relation (2.20), we now obtain

$$0 = \tanh 2kx_0 \left(\frac{\omega^4}{\rho_0^2} \left(\frac{1}{\rho_1^L} - \frac{1}{\rho_2^L} \tanh k(x_0 - x_1^L) \right) \left(\frac{1}{\rho_1^R} - \frac{1}{\rho_2^R} \tanh k(x_0 - x_1^R) \right) + \right.$$
$$+ \frac{(k^2 v_A^2 - \omega^2)^2}{\rho_1^L \rho_1^R} \left(\frac{1}{\rho_2^L} - \frac{1}{\rho_1^L} \tanh k(x_0 - x_1^L) \right) \left(\frac{1}{\rho_2^R} - \frac{1}{\rho_1^R} \tanh k(x_0 - x_1^R) \right) \Bigg)$$
$$- \frac{\omega^2}{\rho_0} \left(k^2 v_A^2 - \omega^2 \right) \left(\frac{1}{\rho_1^L} \left(\frac{1}{\rho_1^R \rho_2^R} + \frac{1}{\rho_1^R \rho_2^L} - \left(\frac{1}{\rho_2^L \rho_2^R} + \frac{1}{(\rho_1^R)^2} \right) \tanh k(x_0 - x_1^R) \right) \right.$$
$$\left. - \tanh k(x_0 - x_1^L) \left(\frac{1}{\rho_1^R (\rho_1^L)^2} + \frac{1}{\rho_1^R \rho_2^L \rho_2^R} - \left(\frac{1}{(\rho_1^L)^2 \rho_2^R} + \frac{1}{(\rho_1^R)^2 \rho_2^L} \tanh k(x_0 - x_1^R) \right) \right) \right). \tag{2.25}$$

Eq. (2.25) is quadratic in ω^2 so its analytical solutions exist, namely,

$$\omega^2 = \frac{1}{2} k^2 v_A^2 \times$$
$$\frac{\sigma + \rho_0 \tanh 2kx_0 \left(\rho_1^L - \rho_2^L \tanh k(x_0 - x_1^L) \right) \left(\rho_1^R - \rho_2^R \tanh k(x_0 - x_1^R) \right) \pm \sqrt{\varsigma}}{\sigma + \frac{\rho_1^L \rho_1^R}{\rho_0} \tanh 2kx_0 \left(\rho_2^L - \rho_1^L \tanh k(x_0 - x_1^L) \right) \left(\rho_2^R - \rho_1^R \tanh k(x_0 - x_1^R) \right)}. \tag{2.26}$$

Here,

$$\sigma = \rho_1^L \rho_1^R \left(\rho_2^L + \rho_2^R + \rho_0 \tanh 2kx_0 \right) -$$
$$\rho_1^R \left(\rho_1^L \rho_1^L + \rho_2^L \rho_2^R + \rho_0 \rho_2^L \tanh 2kx_0 \right) \tanh k(x_0 - x_1^L) -$$
$$\rho_1^L \left(\rho_1^R \rho_1^R + \rho_2^L \rho_2^R + \rho_0 \rho_2^R \tanh 2kx_0 \right) \tanh k(x_0 - x_1^R) +$$
$$\left(\rho_1^R \rho_1^R \rho_2^L + \rho_1^L \rho_1^L \rho_2^R + \rho_0 \rho_2^L \rho_2^R \tanh 2kx_0 \right) \tanh k(x_0 - x_1^L) \tanh k(x_0 - x_1^R),$$
$$\varsigma = -\rho_1^L \rho_1^R (1 - \tanh^2 k(x_0 - x_1^L))(1 - \tanh^2 k(x_0 - x_1^R))$$
$$\left(-2\rho_1^L \rho_2^L \cosh 2k(x_0 - x_1^L) + \left(\rho_1^L \rho_1^L + \rho_2^L \rho_2^L \right) \sinh 2k(x_0 - x_1^L) \right)$$
$$\left(-2\rho_1^R \rho_2^R \cosh 2k(x_0 - x_1^R) + \left(\rho_1^R \rho_1^R + \rho_2^R \rho_2^R \right) \sinh 2k(x_0 - x_1^R) \right) \tanh^2 2kx_0 +$$
$$\left(-\rho_1^L \rho_1^R (\rho_2^L + \rho_2^R) + \rho_1^L \left(\rho_1^R \rho_1^R + \rho_2^L \rho_2^R \right) \tanh k(x_0 - x_1^R) + \right.$$
$$\left. \tanh k(x_0 - x_1^L) \left(\rho_1^R \left(\rho_1^L \rho_1^L + \rho_2^L \rho_2^R \right) - \left(\rho_1^R \rho_1^R \rho_2^L + \rho_1^L \rho_1^L \rho_2^R \right) \tanh k(x_0 - x_1^R) \right) \right)^2. \tag{2.27}$$

As well as for the two-slab case, solutions (2.26) correspond to surface MHD waves with sub-Alfvénic phase-speeds. Let us now visualise these solutions. Figure 2.10a illustrates the symmetric case with density ratios $R_2^L = R_2^R = 0.5$ and $R_1^L = R_1^R = 10$. In Figs. 2.10b - 2.10d, dispersion is shown under the incompressible approximation, for the case of three adjacent slabs. The behaviour of surface modes resembles the two-slab case. Strong dispersion is found for $kx_0 \leq 1$, and weak dispersion is found in the short-wavelength limit. In the case of strong asymmetry, Figs. 2.10c - 2.10d, the quasi sausage/kink modes do not seem to converge to the same phase speed. This feature

could be exploited for solar magneto-seismology purposes as indication of asymmetric structures. Figure 2.10b corresponds to $R_2^L = 3, R_1^L = R_1^R = 2$, and $R_2^R = 0.5$, for Figure 2.10c the density ratios are $R_2^L = 100, R_1^L = 70, R_1^R = 0.1$, and $R_2^R = 0.5$ and in Figure 2.10d $R_2^L = 0.5, R_1^L = 2, R_1^R = 10$, and $R_2^R = 1$.

2.2.3 Thin-slab approximation for surface waves

By propagating waves in the thin-slab approximation, it is meant the wavelength λ is much greater than the lateral characteristic dimension of the magnetic field. We consider two cases, $d_1^L \approx d_1^R \approx d_0 \ll \lambda$ and $d_1^L \approx d_1^R \ll d_0 \ll \lambda$. The first case corresponds to slabs with similar width, the second one corresponds to a case where the widths of slabs on the left/right are much smaller than that of the central one. We now focus on surface waves, meaning that $m_0^2 > 0$ and $(m_i^{L/R})^2 > 0$. The details of the derivation of the relevant dispersion relation in this approximation are given in Appendix. B. Eqs. (B.2) and (B.3) are the dispersion relations for two-slab case for $d_1^L \approx d_1^R \approx d_0 \ll \lambda$ and $d_1^L \approx d_1^R \ll d_0 \ll \lambda$, respectively. Similarly, Eqs. (B.5), (B.6) correspond to the dispersion relations for the three-slab case under the same assumptions.

Two-slab case

Let us now investigate the modes in the case of a thin magnetic and non-magnetic slab embedded in an asymmetric plasma environment. The spurious solution $\omega^2 = k^2 v_A^2$ to Equations (B.2) and (B.3) is dealt with in Section 3.1. The other solutions to Eq. (B.3), up to first order in kx_0, are

$$\omega^2 = k^2 c_T^2 \left[1 - \frac{2(kx_0)(c_0^2 - c_T^2)}{(c_0^2 + v_A^2)\left(\frac{\rho_0}{\rho_1^R}\sqrt{1 - \frac{c_T^2}{(c_1^R)^2}} + \frac{\rho_0}{\rho_2^L}\sqrt{1 - \frac{c_T^2}{(c_2^L)^2}} \right)} \right], \tag{2.28}$$

and

$$\omega^2 = k^2 v_A^2 \, (kx_0) \, \frac{2\rho_0}{\rho_1^R + \rho_2^L}. \tag{2.29}$$

Solution (2.28) behaves like $\omega^2 \to k^2 c_T^2$ as $kx_0 \to 0$. In particular, although there are no modes with a finite wavenumber with phase-speed c_T, there are waves with approximate phase speed c_T that exist only if $c_T < c_1^R$ and $c_T < c_2^L$. This mode is identified as a slow quasi-sausage surface mode. Solution (2.29) corresponds to the slow quasi-kink surface mode.

Three-slab case

Let us now analyse the three-slab case in the thin magnetic slab approximation. Similar to the two-slab case, $\omega^2 = k^2 v_A^2$ is a spurious solution to Equations (B.5) and (B.6).

The slow quasi-sausage surface mode solution to Eq. (B.6) up to first order in kx_0 is

$$\omega^2 = k^2 c_T^2 \left[1 - \frac{2(kx_0)(c_0^2 - c_T^2)}{(c_0^2 + v_A^2)\left(\frac{\rho_0}{\rho_2^R}\sqrt{1 - \frac{c_T^2}{c_{2r}^2}} + \frac{\rho_0}{\rho_2^L}\sqrt{1 - \frac{c_T^2}{c_{2l}^2}} \right)} \right], \tag{2.30}$$

and the slow quasi-kink surface mode solution is

$$\omega^2 = k^2 v_A^2 \, (kx_0) \, \frac{2\rho_0}{\rho_2^R + \rho_2^L}. \tag{2.31}$$

If $c_{1l} = c_{1r} = c_{2l} = c_{2r} = c_e$ and, hence, $\rho_1^R = \rho_1^L = \rho_2^R = \rho_2^L = \rho_e$, we have one more solution of Eqs. (B.3) and (B.6):

$$\omega^2 = k^2 c_e^2 \left(1 - \left[\frac{(kx_0)\, \rho_e c_e^2 \left(c_0^2 - c_e^2\right)}{\rho_0 \left(c_0^2 + v_A^2\right)\left(c_T^2 - c_e^2\right)} \right]^2 \right). \tag{2.32}$$

Eq. (2.32) is a quasi-sausage mode. Since the results (2.28) - (2.32) do not depend on d_1^L, d_1^R, the results are the same for both cases, up to the first order of the approximation used, and it agrees with the results obtained by Allcock and Erdélyi (2017).

§ 2.3 Summary

In Chapter 2 a mathematical model of a magnetised plasma slab sandwiched between an arbitrary number of plasma interfaces is considered, generalising MHD wave studies in a plasma slab embedded in an asymmetric environment studied by Allcock and Erdélyi (2017, 2018).The general dispersion relation was derived in the matrix form, in particular, dispersion relations were obtained for the two- and three- slab cases. It was shown that, unlike the symmetric case investigated by Roberts (1981b), the dispersion relation does not decouple into dispersion relations of independent modes, resulting now in the existence of solutions with mixed properties, namely the quasi-kink and quasi-sausage modes.

For the two-slab case, eigenfunctions were plotted using numerical solutions for the dispersion relation. Effects of varying the density ratios and ratios of non-magnetic slab width to magnetic slab width were studied. Analytical solutions for the two- and three-slab cases were obtained in the incompressible limit. It is worth noting that the overall behaviour of the phase speed of the modes (*i.e.* the dispersion) for multi-layered slabs is similar to that of the asymmetric single slab case. The phase speeds approach either the Alfvén speed or zero in the thin slab limit, and they converge to different speeds in the wide slab limit.

Next, the thin-slab approximation for surface waves was investigated. It is noted that, up to first order in kx_0, the solutions depend on the equilibrium parameters only of the magnetic slab and the plasma environment at infinity. As well, for both cases $d_1^L \approx d_1^R \approx d_0 \ll \lambda$ and $d_1^L \approx d_1^R \ll d_0 \ll \lambda$, the solutions remain the same.

Chapter 3

MHD waves in magnetic multi-layered asymmetric waveguides

§ 3.1 General multi-layered waveguide model

Let us first consider a model of a plasma structured by an arbitrary number of interfaces with different homogeneous magnetic fields, temperatures, and densities, illustrated by Figure 3.1 in Cartesian geometry. Such a model could be useful for studying linear MHD wave propagation in observed solar atmospheric structures closer to the photosphere, such as magnetic bright points, sunspot light bridges, or light walls. In what follows,

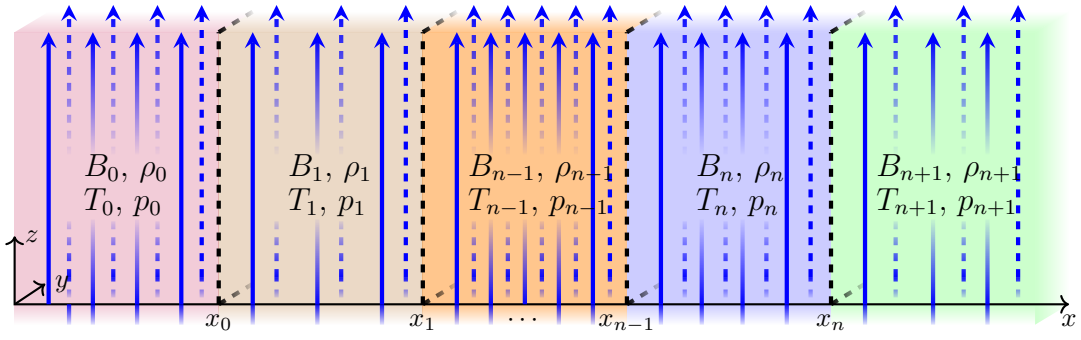

Figure 3.1: The equilibrium configuration of a layered magnetised plasma. The blue arrows represent the vertical magnetic field, $B(x)\widehat{\mathbf{z}}$. The kinetic pressure, p_j, density, ρ_j, and temperature, T_j are equilibrium parameters. The subscript j corresponds to the relevant slab and varies from 0 to $n+1$.

we consider an infinite compressible inviscid structured static plasma with magnetic

field $B(x)\,\widehat{\mathbf{z}}$, where

$$B(x) = \begin{cases} B_0, & \text{for } x < x_0, \\ B_1, & \text{for } x_0 \le x < x_1, \\ \dots & \\ B_n, & \text{for } x_{n-1} \le x < x_n, \\ B_{n+1}, & \text{for } x \ge x_n. \end{cases}$$

We ignore the effects of gravity. We denote the equilibrium kinetic plasma pressure, the density, and temperature by p_j, ρ_j, and T_j, respectively, with subscript j that varies from 0 to $n+1$. In total, there are $n+2$ regions, all of which, in general, are magnetized.

We assume, as before, that the perturbations within the magnetic slab are governed by the ideal MHD Equations (2.1). The Alfvén and sound speeds in the jth region are $v_{Aj} = B_j/\sqrt{\mu\rho_j}$ and $c_j = \sqrt{\gamma p_j/\rho_j}$, respectively. For the system to remain in equilibrium, pressure balance across each interface is required, *i.e.*

$$p_0 + \frac{B_0^2}{2\mu} = p_1 + \frac{B_1^2}{2\mu} = \ldots = p_n + \frac{B_n^2}{2\mu}. \tag{3.1}$$

Equation (3.1) yields the following relation between characteristic speeds and density ratios for any two regions:

$$\frac{\rho_i}{\rho_j} = \frac{c_j^2 + \frac{1}{2}\gamma v_{Aj}^2}{c_i^2 + \frac{1}{2}\gamma v_{Ai}^2}$$

We linearise the governing equations by setting, for each variable f, $f = f_j + f'$, where f_j is the background variable in region j and f' is the comparatively much smaller perturbation variable, then neglecting terms of quadratic or higher order in perturbation variables. For brevity, we drop the $'$ hereafter. We seek plane wave solutions to the linearised governing equations of the form (2.4). Substituting solutions (2.4) into the system of Equations (2.2), and combining the obtained equations, we derive an ordinary differential equation for $\widehat{v}_x$ representing transverse motions inside the magnetic slab,

$$\frac{d^2\widehat{v}_x}{dx^2} - m_j^2\widehat{v}_x = 0, \tag{3.2}$$

where

$$m_j^2 = \frac{(k^2v_{Aj}^2 - \omega^2)(k^2c_j^2 - \omega^2)}{(c_j^2 + v_{Aj}^2)(k^2c_{Tj}^2 - \omega^2)}, \quad c_{Tj}^2 = \frac{c_j^2v_{Aj}^2}{c_j^2 + v_{Aj}^2}. \tag{3.3}$$

Note that $k = (0, 0, k)$, the system is homogeneous in the y-direction, and this derivation deals with magnetoacoustic modes and not Alfvén modes, since $v_y = 0$. Now, we assume that the perturbations vanish at infinity, so that $\widehat{v}_x \to 0$ as $x \to \pm\infty$. We note that m_j^2 may take positive or negative values for j from 1 to n. Since the wave amplitudes

decay exponentially at infinity, we obtain a general solution of Equations (3.2) given by

$$\widehat{v}_x(x) = \begin{cases} P_0(\cosh m_0 x + \sinh m_0 x), & \text{for } x < x_0, \\ P_1 \cosh m_1 x + Q_1 \sinh m_1 x, & \text{for } x_0 < x < x_1, \\ \dots & \\ P_n \cosh m_n x + Q_n \sinh m_n x, & \text{for } x_{n-1} < x < x_n, \\ P_{n+1}(\cosh m_{n+1} x - \sinh m_{n+1} x), & \text{for } x > x_n, \end{cases} \tag{3.4}$$

where P_i and Q_j are constants with $i = 0, 1, \dots n+1$ and $j = 1, 2, \dots n$. Considering the total pressure perturbation $P_T(\mathbf{x}, t)$ in a Fourier form, we obtain

$$\widehat{p}(x) = \widehat{v}_x(x) \begin{cases} \Lambda_0/m_0, & \text{for } x < x_0, \\ \Lambda_1/m_1, & \text{for } x_0 < x < x_1, \\ \dots & \\ \Lambda_n/m_n, & \text{for } x_{n-1} < x < x_n, \\ \Lambda_{n+1}/m_{n+1}, & \text{for } x > x_n, \end{cases} \tag{3.5}$$

with

$$\Lambda_j = -\frac{i\rho_j(k^2 v_{\mathrm{Aj}}^2 - \omega^2)}{m_j \omega}, \quad \text{for} \quad j = 0, 1, \dots n+1. \tag{3.6}$$

Let us now establish appropriate boundary conditions. For physical solutions, the velocity, $v_x(\mathbf{x}, t)$, and total pressure, $P_T(\mathbf{x}, t)$, have to be continuous across the boundaries $x = x_j$ for $j = 0 \dots n$. Equations (3.4) and (3.5) give us $2(n+1)$ coupled homogeneous algebraic equations:

$$\begin{gathered} P_0(\cosh m_0 x_0 + \sinh m_0 x_0) = P_1 \cosh m_1 x_0 + Q_1 \sinh m_1 x_0, \\ \Lambda_0 P_0(\cosh m_0 x_0 + \sinh m_0 x_0) = \Lambda_1(P_1 \sinh m_1 x_0 + Q_1 \cosh m_1 x_0), \\ P_1 \cosh m_1 x_1 + Q_1 \sinh m_1 x_1 = P_2 \cosh m_2 x_1 + Q_2 \sinh m_2 x_1, \\ \Lambda_1(P_1 \sinh m_1 x_1 + Q_1 \cosh m_1 x_1) = \Lambda_2(P_2 \sinh m_2 x_1 + Q_2 \cosh m_2 x_1), \\ \dots \\ P_{n-1} \cosh m_{n-1} x_{n-1} + Q_{n-1} \sinh m_{n-1} x_{n-1} = P_n \cosh m_n x_{n-1} + Q_n \sinh m_n x_{n-1}, \\ \Lambda_{n-1}(P_{n-1} \sinh m_{n-1} x_{n-1} + Q_{n-1} \cosh m_{n-1} x_{n-1}) = \Lambda_n(P_n \sinh m_n x_{n-1} + Q_n \cosh m_n x_{n-1}), \\ P_n \cosh m_n x_n + Q_n \sinh m_n x_n = P_{n+1}(\cosh m_{n+1} x_n - \sinh m_{n+1} x_n), \\ \Lambda_n(P_n \sinh m_n x_n + Q_n \cosh m_n x_n) = \Lambda_{n+1} P_{n+1}(\sinh m_{n+1} x_n - \cosh m_{n+1} x_n), \end{gathered} \tag{3.7}$$

where P_i and Q_j are constant with respect to x. Then, we define $Q_0 = P_0$ and $Q_{n+1} = -P_{n+1}$ and rewrite the above boundary conditions into the following compact form

$$\begin{gathered} P_j \cosh m_j x_j + Q_j \sinh m_j x_j = P_{j+1} \cosh m_{j+1} x_j + Q_{j+1} \sinh m_{j+1} x_j, \\ \Lambda_j(P_j \sinh m_j x_j + Q_j \cosh m_j x_j) = \Lambda_{j+1}(P_{j+1} \sinh m_{j+1} x_j + Q_{j+1} \cosh m_{j+1} x_j), \end{gathered} \tag{3.8}$$

for $j = 0, 1, \ldots n$. One of the advantages of the above form is its simplistic format which enables it to be used in numerical studies for sufficiently large values of n.

We now rearrange the obtained boundary conditions into the following compact matrix form:

$$\mathbf{M}\left(P_0,\ P_1,\ Q_1,\ \ldots\ P_n,\ Q_n,\ P_{n+1}\right)^T = \mathbf{0}, \tag{3.9}$$

where $\mathbf{M}$ is a $[2n+2] \times [2n+2]$ matrix. The precise form of the matrix is given in Appendix C by Equations (C.1)-(C.5).

In order to have a non-trivial solution of the system, the determinant of the matrix $\mathbf{M}$ must be equal to zero:

$$\det \mathbf{M} = 0. \tag{3.10}$$

Equation (3.10), the general dispersion relation, prescribes the nature of linear MHD waves that can propagate along a static multi-layered waveguide, visualized by Figure 3.1. The solutions to this equation, given by the angular frequency, ω, as a function of the wavenumber, k, correspond to the eigenfrequencies of the system.

Two-slab case

In order to make analytical progress, we now analyze a special case of this model in Cartesian geometry, namely, two slabs in an asymmetric magnetic environment, represented by $n = 2$, which is illustrated by Figure 3.2. These special cases bring the waveguide model closer to reality as there are several phenomena in the solar atmosphere that can be well modelled by isolated magnetic slabs, including prominences (Arregui et al., 2012), elongated magnetic bright points (Berger and Title, 1996), and light walls (Yang et al., 2015), to name a few. The width of the magnetic slabs are denoted as d_1 and d_2.

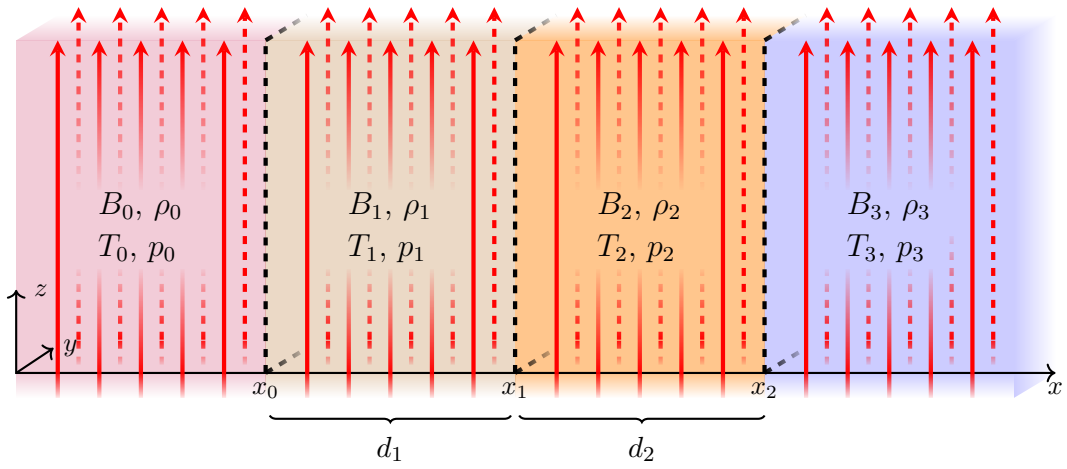

Figure 3.2: Equilibrium configuration for a two-slab case.

From condition (3.10), we obtain the dispersion relation

$$\begin{aligned}\tanh m_2 d_2 \left[\Lambda_1 \left(\Lambda_2^2 + \Lambda_0\Lambda_3\right) + \tanh m_1 d_1 \left(\Lambda_0\Lambda_2^2 + \Lambda_1^2\Lambda_3\right)\right] \\ +\Lambda_2 \left[\Lambda_1 \left(\Lambda_0 + \Lambda_3\right) + \left(\Lambda_1^2 + \Lambda_0\Lambda_3\right) \tanh m_1 d_1\right] = 0. \end{aligned} \tag{3.11}$$

Note, that the two-slab case may be reduced to the single slab case, by assuming that $x_1 = x_2$ and $\Lambda_2 = \Lambda_3$. Substituting notations introduced for Equation (3.6) into the dispersion relation (3.11) and introducing new notation

$$\begin{aligned} T_{ij}^k &= \frac{m_i m_j \rho_k}{\rho_i \rho_j m_k} \left(k^2 v_{Ak}^2 - \omega^2\right)^2 \left(k^2 v_{Al}^2 - \omega^2\right), \\ R_i &= \frac{m_i}{\rho_i} \left(k^2 v_{Aj}^2 - \omega^2\right) \left(k^2 v_{Ak}^2 - \omega^2\right) \left(k^2 v_{Al}^2 - \omega^2\right), \end{aligned}$$

we obtain for surface modes in both slabs

$$\begin{aligned} R_0 + R_3 + \tanh m_1 d_1 \left(R_1 + T_{03}^1\right) \\ + \tanh m_2 d_2 \left(T_{03}^2 + R_2 + \tanh m_1 d_1 \left(T_{13}^2 + T_{02}^1\right)\right) = 0, \end{aligned} \tag{3.12}$$

for surface mode in one slab and body mode in another

$$\begin{aligned} -(R_0 + R_3) + \tan m_1 d_1 \left(R_1 - T_{03}^1\right) \\ - \tanh m_2 d_2 \left(T_{03}^2 + R_2 + \tan m_1 d_1 \left(T_{13}^2 - T_{02}^1\right)\right) = 0 \end{aligned} \tag{3.13}$$

and for body modes in both slabs

$$\begin{aligned} R_0 + R_3 + \tan m_1 d_1 \left(-R_1 + T_{03}^1\right) \\ + \tan m_2 d_2 \left(T_{03}^2 - R_2 - \tan m_1 d_1 \left(T_{13}^2 + T_{02}^1\right)\right) = 0. \end{aligned} \tag{3.14}$$

If $B_0 = B_3 = B_e$, the dispersion relation (3.11) reduces to

$$\begin{aligned} 2\Lambda_1\Lambda_2\Lambda_e + \Lambda_1 \left(\Lambda_2^2 + \Lambda_e^2\right) \tanh m_2 d_2 + \\ + \left(\Lambda_2 \left(\Lambda_1^2 + \Lambda_e^2\right) + \left(\Lambda_1^2 + \Lambda_2^2\right) \Lambda_e \tanh m_2 d_2\right) \tanh m_1 d_1 = 0. \end{aligned}$$

It is possible to split it into the form $(a + b \tanh \frac{d_2 m_2}{2})(a + b \coth \frac{d_2 m_2}{2}) = 0$ with

$$\begin{aligned} a = \Lambda_1 \left(\Lambda_2^2 + \Lambda_e^2\right) + \left(\Lambda_1^2 + \Lambda_2^2\right) \Lambda_e \tanh m_1 d_1 + \\ +\sqrt{\left(\Lambda_2^2 - \Lambda_e^2\right) \left(\Lambda_1 \left(\Lambda_2 - \Lambda_e\right) + \left(\Lambda_2\Lambda_e - \Lambda_1^2\right) \tanh m_1 d_1\right)} \\ \sqrt{\left(\Lambda_1(\Lambda_2 + \Lambda_e) + \left(\Lambda_1^2 + \Lambda_2\Lambda_e\right) \tanh m_1 d_1\right)}, \\ b = 2\Lambda_1\Lambda_2\Lambda_e + \Lambda_2 \left(\Lambda_1^2 + \Lambda_e^2\right) \tanh m_1 d_1. \end{aligned}$$

In general, the solutions of the exact dispersion relation are the mixed-nature quasi-sausage and quasi-kink modes.

3.1.1 Thin-Slab Approximation

By propagating waves in the thin-slab approximation, it is meant the wavelength λ is much greater than the width of the slab. We consider $d_1 \approx d_2 \ll \lambda$ it corresponds to slabs with similar width. We now focus on surface waves, meaning that $m_i^2 > 0$. From Equation (3.12) we receive

$$\begin{aligned} R_0 + R_3 + m_1 d_1 \left(R_1 + T_{03}^1\right) + m_2 d_2 \left(T_{03}^2 + R_2\right) + \\ + m_1 m_2 d_1 d_2 \left(T_{13}^2 + T_{02}^1\right) + O[d_1]^3 + O[d_2]^3 = 0. \end{aligned} \tag{3.15}$$

If $d_1 \approx d_2 \ll \lambda$ from Eq. (3.15) we obtain

$$R_0 + R_3 + m_1 d_1 \left(R_1 + T_{03}^1\right) + m_2 d_2 \left(T_{03}^2 + R_2\right) = 0. \tag{3.16}$$

The frequencies $\omega^2 = k^2 v_{Aj}^2$ are trivial solutions of the dispersion relation.

3.1.2 Incompressible approximation

Magnetoacoustic modes in the incompressible limit arise only from slow modes in the given geometry and choice of field-aligned propagation. In general, the dispersion relation (3.12) is not possible to solve analytically, but the incompressible approximation simplifies it significantly and allows to find an analytical solution. Therefore we focus on other effects than compressibility. Now, let us examine the dispersion relations (3.12) in the limit $\gamma \to \infty$, corresponding to the approximation of an incompressible plasma, where γ is the adiabatic index. From $\gamma \to \infty$, we obtain $c_{Tj} \to v_{Aj}$, hence $m_j \to k$. Let us study the two-slab case. Here, applying the incompressible approximation, the dispersion relation (3.12) becomes

$$\begin{aligned} \tilde{R}_0 + \tilde{R}_3 + \tanh kd_1 \left(\tilde{R}_1 + \tilde{T}_{03}^1\right) + \\ + \tanh kd_2 \left(\tilde{T}_{03}^2 + \tilde{R}_2 + \tanh kd_1 \left(\tilde{T}_{13}^2 + \tilde{T}_{02}^1\right)\right) = 0. \end{aligned} \tag{3.17}$$

where

$$\begin{aligned} \tilde{T}_{ij}^k &= \frac{\rho_k}{\rho_i \rho_j} \left(k^2 v_{Ak}^2 - \omega^2\right)^2 \left(k^2 v_{Al}^2 - \omega^2\right), \\ \tilde{R}_i &= \frac{1}{\rho_i} \left(k^2 v_{Aj}^2 - \omega^2\right) \left(k^2 v_{Ak}^2 - \omega^2\right) \left(k^2 v_{Al}^2 - \omega^2\right), \end{aligned}$$

Equation (3.17) is cubic in ω^2, and can be represented in the form:

$$a\omega^6 - bk^2\omega^4 + ck^4\omega^2 - k^6 d = 0, \tag{3.18}$$

where

$$a = \frac{1}{\rho_0} + \frac{1}{\rho_3} + \left(\frac{1}{\rho_1} + \frac{\rho_1}{\rho_0\rho_3}\right)\tanh kd_1 + \left(\frac{\rho_2}{\rho_0\rho_3} + \frac{1}{\rho_2}\right)\tanh kd_2 + \\ + \left(\frac{\rho_2}{\rho_1\rho_3} + \frac{\rho_1}{\rho_0\rho_2}\right)\tanh kd_1 \tanh kd_2,$$

$$b = \frac{v_{A1}^2 + v_{A2}^2 + v_{A3}^2}{\rho_0} + \frac{v_{A0}^2 + v_{A1}^2 + v_{A2}^2}{\rho_3} + \left(\frac{v_{A0}^2 + v_{A2}^2 + v_{A3}^2}{\rho_1} \right. \\ \left. + \frac{\left(2v_{A1}^2 + v_{A2}^2\right)\rho_1}{\rho_0\rho_3}\right)\tanh kd_1 + \left[\frac{\left(2v_{A2}^2 + v_{A1}^2\right)\rho_2}{\rho_0\rho_3} + \frac{v_{A0}^2 + v_{A1}^2 + v_{A3}^2}{\rho_2} \right. \\ \left. + \left(\frac{\left(2v_{A2}^2 + v_{A0}^2\right)\rho_2}{\rho_1\rho_3} + \frac{\left(2v_{A1}^2 + v_{A3}^2\right)\rho_1}{\rho_0\rho_2}\right)\tanh kd_1\right]\tanh kd_2,$$

$$c = \frac{v_{A2}^2 v_{A3}^2 + v_{A1}^2 v_{A2}^2 + v_{A1}^2 v_{A3}^2}{\rho_0} + \frac{v_{A1}^2 v_{A2}^2 + v_{A0}^2 v_{A1}^2 + v_{A0}^2 v_{A2}^2}{\rho_3} + \\ + \left(\frac{v_{A2}^2 v_{A3}^2 + v_{A0}^2 v_{A2}^2 + v_{A0}^2 v_{A3}^2}{\rho_1} + \frac{\left(v_{A1}^4 + 2v_{A1}^2 v_{A2}^2\right)\rho_1}{\rho_0\rho_3}\right)\tanh kd_1 + \\ \left(\frac{\left(v_{A2}^4 + 2v_{A1}^2 v_{A2}^2\right)\rho_2}{\rho_0\rho_3} + \frac{v_{A1}^2 v_{A3}^2 + v_{A0}^2 v_{A1}^2 + v_{A0}^2 v_{A3}^2}{\rho_2}\right)\tanh kd_2 + \\ + \left(\frac{\left(v_{A2}^4 + 2v_{A0}^2 v_{A2}^2\right)\rho_2}{\rho_1\rho_3} + \frac{\left(v_{A1}^4 + 2v_{A1}^2 v_{A3}^2\right)\rho_1}{\rho_0\rho_2}\right)\tanh kd_1 \tanh kd_2,$$

$$d = \frac{v_{A1}^2 v_{A2}^2 v_{A3}^2}{\rho_0} + \frac{v_{A0}^2 v_{A1}^2 v_{A2}^2}{\rho_3} + \left(\frac{v_{A0}^2 v_{A2}^2 v_{A3}^2}{\rho_1} + \frac{v_{A1}^4 v_{A2}^2 \rho_1}{\rho_0\rho_3}\right)\tanh kd_1 + \\ + \left(\frac{v_{A0}^2 v_{A1}^2 v_{A3}^2}{\rho_2} + \frac{v_{A2}^4 v_{A1}^2 \rho_2}{\rho_0\rho_3}\right)\tanh kd_2 + \left(\frac{v_{A1}^4 v_{A3}^2 \rho_1}{\rho_0\rho_2} + \frac{v_{A0}^2 v_{A2}^4 \rho_2}{\rho_1\rho_3}\right)\tanh kd_1 \tanh kd_2,$$

so we can solve it in a closed form using Cardano's Formula.

§ 3.2 Summary

The propagation of linear MHD waves in a multi-layered magnetised plasma structure is studied in the Cartesian slab geometry approximation. Each magnetic slab is uniform and non-stratified (*i.e.* neither density nor magnetic stratification is considered). A general dispersion relation is derived for a mathematical model of this plasma structured by an arbitrary number of interfaces. The derived dispersion relation could be used not only for multi-layered magnetised plasma structure, but also for a different combination of magnetic and non-magnetic slabs, by simply choosing corresponding magnetic field for non-magnetic slab equal to zero. One special cases of a two-slabs embedded in an asymmetric magnetic environment is considered. Unlike the symmetric case, the obtained dispersion relation does not decouple into two dispersion relations of independent wave mode solutions. This coupling manifests as mixed properties of

the eigenmodes, which are referred to as quasi-kink and quasi-sausage wave solutions to the governing linear magneto-acoustic equations. These newly obtained eigenmodes are generalisations of the traditionally known sausage and kink modes of symmetric linear MHD waveguides.

The asymmetry of waveguides, which is highly likely in many solar structures due to the structural inhomogeneity of the various observed MHD waveguides in the solar atmosphere, is a proxy for background parameters of the waveguide. Incorporating asymmetric external magnetic fields into the multi-slab model provides a further useful middle-ground between the breadth of applications and analytical tractability. From coronal hole boundaries, through prominences, to MBPs of the photosphere, a variety of solar atmospheric fine structures can be more closely described as a magnetized asymmetric slab system. Next to numerical root-finding methods, making certain well-known approximations, such as investigating the limit of a thin or a wide slab, allows us to concisely describe the various quasi-sausage, quasi-kink, surface, or body modes that we expect, and to identify some of their fundamental characteristics.

The one- or multi-slab approach to asymmetric waveguides has wide applicability in different layers of the solar atmosphere. MHD waves have been observed in many structures of our Sun, and to correctly interpret some of them, the asymmetry of their environments should be taken into account.

A variety of waves have been observed in sunspot structures, for example, in the penumbra, which itself shows a filamentary structure. Neighbouring filaments may be modelled by different plasma and magnetic parameters, and they have been observed to support upward propagating slow-mode magneto-acoustic waves in the form of running penumbral waves (Bloomfield et al., 2007; Freij et al., 2014; Löhner-Böttcher and Bello González, 2015). The multi-slab model may be a good approximation for high-frequency waves. Another sunspot element where asymmetry of the plasma environment could heavily influence wave propagation is the light bridge and corresponding light wall reaching up into higher layers of the atmosphere, which are trapped between two, sometimes vastly different umbral cores. Oscillations recently detected in light walls have been interpreted as signatures of propagating magneto-acoustic (shock) waves (Yang et al., 2015; Zhang et al., 2017).

Small, bright magnetic flux concentrations are located in the intergranular lanes wedged in-between two granular cells, whose plasma and magnetic properties can potentially be highly different. This asymmetry then naturally affects the characteristics of any waves present in the above-mentioned MBPs. These small-scale magnetic elements, which might take on the appearance of a nearly circular flux tube or a strongly elongated slab-like structure, have been put forward as the photospheric anchor points of chromospheric waveguides that show sausage-mode oscillations (Morton et al., 2012). The existence of wealth of magneto-acoustic oscillations within MBPs themselves has also been concluded from high-cadence observations performed at different altitudes (Jess et al., 2012). Chromospheric manifestations of bright points have been confirmed to sway around their photospheric counterparts, signalling the presence of kink type oscillations (Xiong et al., 2017).

Additionally, Alfvén waves are also known to propagate in the solar atmosphere.

However, Alfvén waves are local waves as opposed to the sausage and kink waves that have a global character. Alfvén waves propagate along constant magnetic surfaces . If there is a suitable driver, each magnetic surface supports its own Alfvén wave, which will be characterised by the properties of the individual flux sheets and will not be strongly affected by the rest of the plasma environment. Because of this, Alfvén waves are not very promising disturbances for the application of our magneto-seismological technique described in this chapter.

Chapter 4

Resonant damping of propagating kink waves in non-stationary, longitudinally stratified, and expanding solar waveguides

§ 4.1 Problem formulation and governing equations

In this chapter, propagation of kink waves is considered in a straight expanding magnetic flux tube with a variable radius of the circular cross-section (see Fig. 4.1). We define its characteristic radius as R_*. Since the tube expansion is present, we suppose that the magnetic field has a spatial dependence. However, its spatial variation scale is $L_* \gg R_*$, which means that the thin tube approximation could be used. We introduce cylindrical coordinate system r, φ, z, where the tube axis matches with the z-axis. It is alleged, that the system is axisymmetric, that yields that all model parameters could be assumed to be independent of φ. As well, a non-twisted magnetic field is considered, i.e. $B_\varphi = 0$. Hence the equilibrium magnetic field has only axial and radial components, that can be rewritten in terms of the magnetic flux function ψ as

$$B_r = -\frac{1}{r}\frac{\partial \psi}{\partial z}, \quad B_z = \frac{1}{r}\frac{\partial \psi}{\partial r}. \tag{4.1}$$

It was shown by Ruderman et al. (2017) (Paper I in what follows) that in the thin tube approximation

$$\psi = \frac{1}{2} r^2 h(z), \tag{4.2}$$

where $h(z)$ is an arbitrary function of z. This expression is valid both in the tube and in its immediate surrounding.

From Equations (4.1) and (4.2) it follows that

$$B_r = -\frac{1}{2} r h'(z), \quad B_z = h(z). \tag{4.3}$$

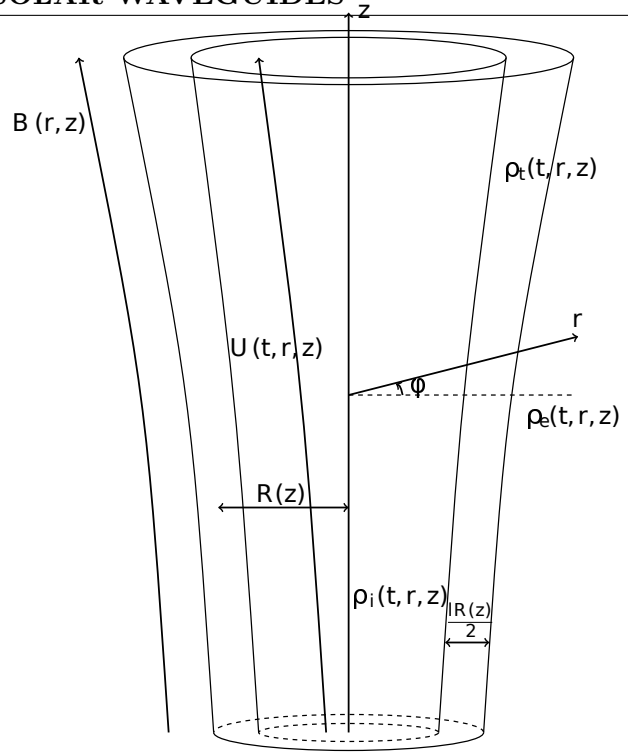

Figure 4.1: Sketch of the equilibrium.

Since $h'(z) \sim h(z)/L_*$, thus

$$\frac{B_r}{B_z} = \mathcal{O}(\varepsilon), \quad B = h(z)\big[1 + \mathcal{O}\big(\varepsilon^2\big)\big], \tag{4.4}$$

where $\varepsilon = R_*/L_*$.

In this model, the tube consists of core and transitional regions. In what follows, for the quantities in the core, transitional regions and in the surrounding plasma we use indices i, t, e, respectively. The plasma density is considered to be monotonically decreasing function in the radial direction. It has value ρ_i in the core region inside the tube and reaches value ρ_e outside the tube. It varies as well in the longitudinal direction. The transitional layer is supposed to be thick, its characteristic thickness is lR_*, where $l \ll 1$. Thus the thin boundary approximation is applied. The transitional layer boundaries are defined by the equations

$$r = R(z)(1 - l/2), \quad r = R(z)(1 + l/2). \tag{4.5}$$

Now it follows from the magnetic flux conservation that the magnetic field tube magnitude and the tube radius are related by the approximate equation

$$BR^2 = \text{const}. \tag{4.6}$$

It follows from Equations (4.2)–(4.6) that the transitional layer boundaries are magnetic field lines and their equations can be written in an alternative form as

$$\psi = \psi_i \equiv \frac{1}{2}BR^2\left(1-\frac{l}{2}\right)^2, \quad \psi = \psi_e \equiv \frac{1}{2}BR^2\left(1+\frac{l}{2}\right)^2. \tag{4.7}$$

The density variation has characteristic scale L_* in the longitudial direction. In the radial direction, it has the same characteristic scale outside the tube and in the core layer, and the characteristic scale is lR_* in the boundary region. Moreover, ρ is a function on time, that could create the plasma flow in the direction of the line of magnetic force. It is supposed, that the variation of the velocity is weak along the tube in the core region and in the surrounding plasma, however, in the boundary layer it has characteristic variation scale of lR_*. The mass conservation equation that connects velocity $\boldsymbol{U} = (U_r, 0, U_z)$ and density ρ is

$$\frac{\partial\rho}{\partial t} + \frac{1}{r}\frac{\partial(\rho r U_r)}{\partial r} + \frac{\partial(\rho U_z)}{\partial z} = 0. \tag{4.8}$$

Since the velocity is parallel to the magnetic field it follows from Equation (4.4) that

$$\frac{U_r}{U_z} = \mathcal{O}(\varepsilon), \quad U = U_z\big[1+\mathcal{O}\big(\varepsilon^2\big)\big]. \tag{4.9}$$

We integrate Equation (4.8) over the area of the tube core cross-section, that is over a circle of radius $R(z)(1-l/2)$. As a result we obtain

$$R^2(1-l/2)^2\left(\frac{\partial\rho}{\partial t} + \frac{\partial(\rho U_z)}{\partial z}\right) + 2(\rho r U_r)\big|_{r=R(1-l/2)} = 0. \tag{4.10}$$

It follows from Equations (4.3), (4.4), and (4.6) that $hR^2 = \text{const}$. Using this equation and Equations (4.3), (4.4), and (4.9) yields

$$\left.\frac{U_r}{U}\right|_{r=R(1-l/2)} = \left.\frac{B_r}{B}\right|_{r=R(1-l/2)} = -\frac{h'R(1-l/2)}{2h} = R'(1-l/2). \tag{4.11}$$

Substituting this result in Equation (4.10) we obtain in the leading order approximation with respect to ε and l

$$\frac{\partial\rho_i}{\partial t} + \frac{1}{R^2}\frac{\partial(\rho_i R^2 U_i)}{\partial z} = 0. \tag{4.12}$$

Next we integrate Equation (4.8) over the ring region $R(1+l/2) \le r \le \varsigma R$, where $\varsigma - 1 \gg l$ and ς is of the order of unity. This yields

$$R^2\big(\varsigma^2 - 1 - l - l^2/4\big)\left(\frac{\partial\rho}{\partial t} + \frac{\partial(\rho U_z)}{\partial z}\right) + 2(\rho r U_r)\Big|_{r=R(1+l/2)}^{\varsigma R} = 0. \tag{4.13}$$

Similar to Equation (4.8) we obtain

$$\left.\frac{U_r}{U}\right|_{r=\varsigma R} = \varsigma R'. \tag{4.14}$$

Using Equations (4.11) and (4.14) we obtain from Equation (4.13), again in the leading order approximation with respect to ε and l,

$$\frac{\partial \rho_e}{\partial t} + \frac{1}{R^2}\frac{\partial (\rho_e R^2 U_e)}{\partial z} = 0. \tag{4.15}$$

It was shown in Paper I that long linear kink waves, which are waves with the wavelength much larger than R_*, in an expanding and non-stationary magnetic tube is described by the equation

$$\begin{aligned} &\rho_i\left(\frac{\partial}{\partial t} + \frac{U_i}{R^2}\frac{\partial}{\partial z}R^2\right)\left(\frac{\partial \eta}{\partial t} + U_i\frac{\partial \eta}{\partial z}\right) \\ &+ \rho_e\left(\frac{\partial}{\partial t} + \frac{U_e}{R^2}\frac{\partial}{\partial z}R^2\right)\left(\frac{\partial \eta}{\partial t} + U_e\frac{\partial \eta}{\partial z}\right) - \frac{2B^2}{\mu_0}\frac{\partial^2 \eta}{\partial z^2} = \mathcal{L}, \end{aligned} \tag{4.16}$$

where

$$\begin{aligned} \mathcal{L} = &\frac{\delta P}{R^2} + \frac{B^2}{\mu_0}\frac{\partial^2 (l\eta + \delta\eta)}{\partial z^2} \\ &- \rho_e\left(\frac{\partial}{\partial t} + \frac{U_e}{R^2}\frac{\partial}{\partial z}R^2\right)\left(\frac{\partial}{\partial t} + U_e\frac{\partial}{\partial z}\right)(l\eta + \delta\eta). \end{aligned} \tag{4.17}$$

In this equations μ_0 is the magnetic permeability of free space, P is the perturbation of magnetic pressure, $\eta = \xi_{\perp i}/R$, and $\xi_\perp$ is the plasma displacement in the $\varphi = \text{const}$ plane and perpendicular to the magnetic field lines. We note that in the thin tube approximation $\xi_{\perp i}$ is independent of r. The quantities $\delta\eta$ and δP are the jumps across the transitional layer defined by

$$\delta\eta = \frac{1}{R}\left(\xi_\perp\big|_{\psi=\psi_e} - \xi_\perp\big|_{\psi=\psi_i}\right), \quad \delta P = P\big|_{\psi=\psi_e} - P\big|_{\psi=\psi_i}. \tag{4.18}$$

Equation (4.17) with the right-hand side defined by Equation (4.18) is used below to study the propagation of kink waves.

§ 4.2 Derivation of the evolutionary equation

In this section we consider propagation of kink waves along an expanding and non-stationary magnetic tube. Using Equations (4.12) and (4.15) we transform Equation (4.11) to

$$\begin{aligned} (\rho_i + \rho_e)\frac{\partial^2 \eta}{\partial t^2} &+ 2(\rho_i U_i + \rho_e U_e)\frac{\partial^2 \eta}{\partial t \partial z} + \left(\rho_i U_i^2 + \rho_e U_e^2 - \frac{2B_0^2}{\mu_0}\right)\frac{\partial^2 \eta}{\partial z^2} \\ &+ \left\{\frac{\partial}{\partial t}(\rho_i U_i + \rho_e U_e) + \frac{1}{R^4}\frac{\partial}{\partial z}\left[R^4(\rho_i U_i^2 + \rho_e U_e^2)\right]\right\}\frac{\partial \eta}{\partial z} \\ &- \left[\frac{\partial}{\partial t}(\rho_i + \rho_e) + \frac{\partial}{\partial z}(\rho_i U_i + \rho_e U_e)\right]\frac{\partial \eta}{\partial t} = 0. \end{aligned} \tag{4.19}$$

Let us now analyse the wave propagation process with a wavelength λ in the range $R_* \ll \lambda \ll L_*$. We use notation $\epsilon \ll 1$ for the ratio of characteristic wavelength to characteristic scale in the longitudinal direction L_*. From the assumption that the wavelength $\lambda \gg R_*$, we obtain $\epsilon \gg \varepsilon = R_*/L_*$. The waves with the period much shorter than the temporal density variation scale are considered.

In order to have resonant damping, we should include a transitional layer. Further, it will shown, that the order of the damping length can be estimated as $l^{-1}\lambda$. At the same time, the effect of inhomogeneity becomes significant at the distance scales $\epsilon^{-1}\lambda$. To describe the amplitude of the wave, we would like to have an equation which takes into account both these effects with the same accuracy of approximation.

In what follows, we are keen to acquire the way to portray the wave amplitude that accounts at the same level of approximation for the both effects in the form of the equation. Therefore we let $l = \epsilon$. In what follows, we will show that $\mathcal{L}$ is of the order of ϵ^{-1}. Such an indicator leads us directly to considering stretched variables. Thus we let $\widetilde{\mathcal{L}} = \epsilon\mathcal{L}$. We assume that the ratio of the wave period to the characteristic time of density variation is also of the order ϵ. As a result, we have an opportunity to describe the temporal density variation in the same order approximation as the effects of damping and inhomogeneity.

In order to find solution to the Equation (4.19), we suppose that it has the form $\eta = S\exp(i\epsilon^{-1}\theta)$, with S as complex and θ as real (Bender and Orszag, 1978). In the second order approximation, we have

$$(\rho_i + \rho_e)\omega^2 - 2(\rho_i U_i + \rho_e U_e)k\omega + \left(\rho_i U_i^2 + \rho_e U_e^2 - \frac{2B_0^2}{\mu_0}\right)k^2 = 0, \tag{4.20}$$

where

$$\omega = -\frac{\partial\theta}{\partial t}, \quad k = \frac{\partial\theta}{\partial z}. \tag{4.21}$$

This approximation is usually called the approximation of geometrical optics.

Next, we collect terms proportional to ϵ^{-1}. This results in

$$\begin{aligned}(\rho_i + \rho_e)\left(S\frac{\partial\omega}{\partial t} \right. &+ \left. 2\omega\frac{\partial S}{\partial t}\right) + 2(\rho_i U_i + \rho_e U_e)\left(S\frac{\partial\omega}{\partial z} + \omega\frac{\partial S}{\partial z} - k\frac{\partial S}{\partial t}\right)\\ &- \left(\rho_i U_i^2 + \rho_e U_e^2 - \frac{2B_0^2}{\mu_0}\right)\left(S\frac{\partial k}{\partial z} + 2k\frac{\partial S}{\partial z}\right)\\ &- \left\{\frac{\partial}{\partial t}(\rho_i U_i + \rho_e U_e) + \frac{1}{R^4}\frac{\partial}{\partial z}\left[R^4(\rho_i U_i^2 + \rho_e U_e^2)\right]\right\}kS\\ &- \left[\frac{\partial}{\partial t}(\rho_i + \rho_e) + \frac{\partial}{\partial z}(\rho_i U_i + \rho_e U_e)\right]\omega S = ie^{-il^{-1}\theta}\widetilde{\mathcal{L}}. \end{aligned} \tag{4.22}$$

Multiplying this equation by SR^4 and using Equation (4.6) we obtain

$$\begin{aligned} R^4(\rho_i &+ \rho_e)\frac{\partial(\omega S^2)}{\partial t} - R^4(\rho_i U_i + \rho_e U_e)\left[\frac{\partial(kS^2)}{\partial t} - \frac{\partial(\omega S^2)}{\partial z}\right] \\ &- \frac{\partial}{\partial z}\left[\left(\rho_i U_i^2 + \rho_e U_e^2 - \frac{2B_0^2}{\mu_0}\right) kR^4 S^2\right] - kR^4 S^2 \frac{\partial}{\partial t}\left(\rho_i U_i + \rho_e U_e\right) \\ &- \left[\frac{\partial}{\partial t}\left(\rho_i + \rho_e\right) + \frac{\partial}{\partial z}\left(\rho_i U_i + \rho_e U_e\right)\right] \omega R^4 S^2 = ie^{-il^{-1}\theta} SR^4 \widetilde{\mathcal{L}}. \end{aligned} \tag{4.23}$$

We further transform this equation to

$$\begin{aligned} &\frac{\partial}{\partial t}\left\{R^4 S^2\left[(\rho_i + \rho_e)\omega - (\rho_i U_i + \rho_e U_e)k\right]\right\} \\ &+ R^4(\rho_i U_i + \rho_e U_e)\frac{\partial(\omega S^2)}{\partial z} - \frac{\partial}{\partial z}\left[\left(\rho_i U_i^2 + \rho_e U_e^2 - \frac{2B_0^2}{\mu_0}\right) kR^4 S^2\right] \\ &- \left[2\frac{\partial}{\partial t}\left(\rho_i + \rho_e\right) + \frac{\partial}{\partial z}\left(\rho_i U_i + \rho_e U_e\right)\right] \omega R^4 S^2 = ie^{-il^{-1}\theta} SR^4 \widetilde{\mathcal{L}}. \end{aligned} \tag{4.24}$$

We now transform the terms on the left-hand side of this equation that are not full derivatives. Using Equations (4.12) and (4.15) we obtain

$$\begin{aligned} &R^4(\rho_i U_i + \rho_e U_e)\frac{\partial(\omega S^2)}{\partial z} - \left[2\frac{\partial}{\partial t}\left(\rho_i + \rho_e\right) + \frac{\partial}{\partial z}\left(\rho_i U_i + \rho_e U_e\right)\right] \omega R^4 S^2 \\ &= R^4(\rho_i U_i + \rho_e U_e)\frac{\partial(\omega S^2)}{\partial z} + \left[2\left(\rho_i U_i + \rho_e U_e\right)\frac{\partial R^2}{\partial z} + R^2\frac{\partial}{\partial z}\left(\rho_i U_i + \rho_e U_e\right)\right] \omega R^2 S^2 \\ &= R^4(\rho_i U_i + \rho_e U_e)\frac{\partial(\omega S^2)}{\partial z} + \omega S^2\frac{\partial}{\partial z}\left[R^4(\rho_i U_i + \rho_e U_e)\right] = \frac{\partial}{\partial z}\left[(\rho_i U_i + \rho_e U_e)\omega R^4 S^2\right] \end{aligned} \tag{4.25}$$

Using this result we reduce Equation (4.24) to

$$\begin{aligned} &\frac{\partial}{\partial t}\left\{R^4 S^2\left[(\rho_i + \rho_e)\omega - (\rho_i U_i + \rho_e U_e)k\right]\right\} \\ &+ \frac{\partial}{\partial z}\left\{R^4 S^2\left[(\rho_i U_i + \rho_e U_e)\omega - \left(\rho_i U_i^2 + \rho_e U_e^2 - \frac{2B_0^2}{\mu_0}\right)k\right]\right\} = ie^{-il^{-1}\theta} SR^4 \widetilde{\mathcal{L}}. \end{aligned} \tag{4.26}$$

Finally, introducing

$$V = \frac{\omega}{k}, \quad \mathcal{E} = R^4 S^2\left[(\rho_i + \rho_e)\omega - (\rho_i U_i + \rho_e U_e)k\right], \tag{4.27}$$

and using Equation (4.20) we rewrite Equation (4.26) as

$$\frac{\partial \mathcal{E}}{\partial t} + \frac{\partial(V\mathcal{E})}{\partial z} = ie^{-il^{-1}\theta} SR^4 \widetilde{\mathcal{L}}. \tag{4.28}$$

Now, for the example of kink oscillation of cooling coronal loops we consider that the temporal variation of the density is follows we assume that the temporal variation

of the density is significantly time consuming. Following the report Aschwanden and Schrijver (2011) on observed cooling coronal loops, we have the series of estimated measurements. First, the cooling time is estimated to be 2050 s. The estimate for corresponding to fundamental frequency was 395 s and the estimate for the length of the coronal loop was 163 Mm. As a result, we can estimate the phase speed of the kink in that coronal loop to be 893 km/s. We assume that the estimated cooling time is the characteristic time that is employed in Equation (4.12). Moreover, we let the length of the coronal loop to be the characteristic length within the proposed model. Therefore, on basis of these characteristics variables we have the estimate for the internal flow speed $U_i \sim 80$ km/s. We should note the no information was given about the temperature outside of the coronal loop in Aschwanden and Schrijver (2011) report. Radiation is the main mechanism of cooling in the coronal loops under typical coronal conditions. Its intensity is directly proportional to the square of the plasma density. In the exterior outside of the loop, the plasma has much lower density than within the loop. As a result, variation of the plasma temperature in the external region might not have significant impact of the temperature within coronal loop on the proposed characteristic time scales. Thus, in case both external and internal plasma cools down, we are expecting $U_e \ll U_i$. Moreover, we conclude that in the event reported by Aschwanden and Schrijver (2011) the speed of the flow induced by cooling is much smaller than the phase speed.

On the basis of this example we introduce the definition that the temporal density variation is very slow if the flow speed induced by this variation is much smaller than the phase speed. The assumption that the temporal density variation is very slow enables us to neglect the terms containing U_i and U_e in Equation (4.20). In addition, we only consider waves propagating in the positive z-direction. Then Equation (4.20) reduces to

$$\omega = C_k k, \quad C_k^2 = \frac{2B^2}{\mu_0(\rho_i + \rho_e)}. \tag{4.29}$$

We also can neglect the terms proportional to U_i and U_e in the expression for $\mathcal{E}$ and write it in the approximate form as

$$\mathcal{E} = (\rho_i + \rho_e)\omega R^4 S^2. \tag{4.30}$$

§ 4.3 Derivation of expression for $\widetilde{\mathcal{L}}$

Below, we use static linear MHD equations in the transitional layer in order to illustrate plasma motions. It is possible to employ static version of equations rather than dynamic version of them due to temporal variation of density being significantly slow. Nevertheless, we consider plasma density being dependent on time. The plasma viscosity is added to MHD equation at the resonant surface in order to enable the system to exist without the singularity. Below, we use the system of equations derived by Shukhobodskiy and Ruderman (2018). In this system ψ is used as an independent variable instead of r. Since Shukhobodskiy and Ruderman (2018) considered a static problem with the density independent on time they took the perturbation of all variables proportional

to $e^{-i\omega t}$ to obtain:

$$P = -\frac{1}{\mu_0}\left(rB^2\frac{\partial w}{\partial \psi} + iB^2\frac{\xi_\varphi}{r} - B_r\frac{\partial w}{\partial z} + B_z\frac{w}{r}\right), \tag{4.31}$$

$$\begin{aligned}\omega^2 w &= -\frac{rB^2B_z}{\mu_0\rho}\frac{\partial}{\partial z}\left(\frac{B_z}{r^2B^2}\frac{\partial(rw)}{\partial z}\right) - \frac{B^2}{\rho}\left[B_r\frac{\partial}{\partial z}\left(\frac{P}{B^2}\right)\right. \\ &- \left. rB^2\frac{\partial}{\partial \psi}\left(\frac{P}{B^2}\right)\right] + i\nu\omega\left(r^2B_z^2\frac{\partial^2 w}{\partial \psi^2} - \frac{w}{r^2}\right),\end{aligned} \tag{4.32}$$

$$\omega^2\xi_\varphi = \frac{iP}{\rho r} - \frac{B_z}{\mu_0\rho r}\frac{\partial}{\partial z}\left[r^2B_z\frac{\partial}{\partial z}\left(\frac{\xi_\varphi}{r}\right)\right] + i\omega\nu\left(r^2B_z^2\frac{\partial^2\xi_\varphi}{\partial\psi^2} - \frac{\xi_\varphi}{r^2}\right). \tag{4.33}$$

We now restore the time dependence in this system of equations by substituting $\partial/\partial t$ for $-i\omega$. Thus, transform the original system to

$$P = -\frac{1}{\mu_0}\left(rB^2\frac{\partial w}{\partial \psi} + iB^2\frac{\xi_\varphi}{r} - B_r\frac{\partial w}{\partial z} + B_z\frac{w}{r}\right), \tag{4.34}$$

$$\begin{aligned}\frac{\partial^2 w}{\partial t^2} &= \frac{rB^2B_z}{\mu_0\rho}\frac{\partial}{\partial z}\left(\frac{B_z}{r^2B^2}\frac{\partial(rw)}{\partial z}\right) + \frac{B^2}{\rho}\left[B_r\frac{\partial}{\partial z}\left(\frac{P}{B^2}\right)\right. \\ &- \left. rB^2\frac{\partial}{\partial \psi}\left(\frac{P}{B^2}\right)\right] + \nu\frac{\partial}{\partial t}\left(r^2B_z^2\frac{\partial^2 w}{\partial \psi^2} - \frac{w}{r^2}\right),\end{aligned} \tag{4.35}$$

$$\frac{\partial^2\xi_\varphi}{\partial t^2} = -\frac{iP}{\rho r} + \frac{B_z}{\mu_0\rho r}\frac{\partial}{\partial z}\left[r^2B_z\frac{\partial}{\partial z}\left(\frac{\xi_\varphi}{r}\right)\right] + \nu\frac{\partial}{\partial t}\left(r^2B_z^2\frac{\partial^2\xi_\varphi}{\partial\psi^2} - \frac{\xi_\varphi}{r^2}\right). \tag{4.36}$$

In Equations (4.31) – (4.36), ξ_φ is the φ-component of the plasma displacement, ν is the kinematic viscosity and $w = B\xi_\perp$. In this system of equations r is a dependent on ψ and z variable. Equations (4.34) – (4.36) are applicable both within the magnetic flux tube as well as outside of it. We should note that we can neglect terms proportional to ν outside of the transitional layer. $l\varepsilon^{-1}R_* \gg R_*$ and $l\varepsilon^{-1}R_*/V_*$ are defining characteristic scale with the respect to z component and time with the respect to t component of variation of perturbations respectively. Here, V_* is the characteristic value of the phase speed. In what follows, we let $V_*^2 = B_*^2/(\mu_0\rho_*)$, where B_* is the characteristic value of the magnetic field and ρ_* is the characteristic value of the density. Employing these estimates, yields $P \sim l^{-2}\varepsilon^2V_*^2R_*^{-1}\xi_\varphi$. As a result, we can estimate the ratio of the LHS (left-hand side) of Equation (4.34) to the second term in the brackets in the same equation. This ratio has the order of $l^{-2}\varepsilon^2 \ll 1$. Therefore we can disregard LHS of Equation (4.34). Similarly, we can disregard the third term of Equation (4.34), since the ratio of the third term in the brackets on the RHS (right-hand side) of Equation (4.34) to the fourth term is $l^{-1}\varepsilon^2 \ll 1$. As a result, we transform Equation (4.34) to

$$r^2B\frac{\partial w}{\partial \psi} + iB\xi_\varphi + w = 0. \tag{4.37}$$

Finally, since in the core region the dependence of both B and $\xi_\perp$ on ψ can be neglected, in this region we also can drop the first term in Equation (4.37).

We put

$$w = \hat{w}e^{il^{-1}\theta}, \quad \xi_\varphi = \hat{\xi}_\varphi e^{il^{-1}\theta}, \quad P = \hat{P}e^{il^{-1}\theta}. \tag{4.38}$$

Using the relations $w = B\xi_\perp$, $\eta = \xi_{\perp i}/R$ and $\eta = S\exp(i\epsilon^{-1}\theta)$, and taking into account that the dependence of $\xi_\perp$ on ψ in the core region can be neglected we obtain the expression valid in the core region,

$$\hat{w}_i = BRS. \tag{4.39}$$

Substituting Equations (4.38) and (4.39) in Equation (4.34) with the small terms neglected, and in Equation (4.36) with $\nu = 0$, and collecting the leading terms with respect to l we obtain the following equations valid in the core region,

$$i\hat{\xi}_\varphi + RS = 0, \tag{4.40}$$

$$\hat{P} = -il^{-2}r\rho\left(\omega^2 - \frac{B^2k^2}{\mu_0\rho}\right)\hat{\xi}_\varphi. \tag{4.41}$$

Eliminating $\hat{\xi}_\varphi$ from these equations yields

$$\hat{P} = l^{-2}r\rho RS\left(\omega^2 - \frac{B^2k^2}{\mu_0\rho}\right). \tag{4.42}$$

In order to investigate propagating kink wave we need first to determine $\widetilde{\mathcal{L}}$. We start by reducing Equations (4.35)–(4.37). Similarly to Shukhobodskiy et al. (2018) in the transitional layer we can approximate $r(\psi, z) \approx R(z)$. Employing Equations (4.3) and (4.4), yeilds that we can approximate B_z as $B_z \approx B$. Thus, we can neglect the relationship of B on ψ. Moreover, $\psi_e - \psi_i = lBR^2$ is the characteristic scale of perturbations in the transitional region as well as is the characteristic scale of the density. With the aid of above estimates, we can conclude with ease that the second term in the square brackets in Equation (4.35) overshadows the first term. Furthermore, the first terms of the governing system in bracketed terms that are proportional to ν are significantly greater than the second terms. Lastly, l is the order of the ratio between the third and first term in Equation (4.37). As a result, we can disregard the third term. Finally, employing Equation (4.6) we simplify Equations (4.35)–(4.37) to yield

$$r^2\frac{\partial w}{\partial \psi} + i\xi_\varphi = 0, \tag{4.43}$$

$$\frac{\partial^2 w}{\partial t^2} = \frac{B^2}{\mu_0\rho R}\frac{\partial^2(wR)}{\partial z^2} - \frac{RB^2}{\rho}\frac{\partial P}{\partial \psi} + \nu R^2B^2\frac{\partial^3 w}{\partial t\partial\psi^2}, \tag{4.44}$$

$$\frac{\partial^2 \xi_\varphi}{\partial t^2} = -\frac{iP}{\rho R} + \frac{RB^2}{\mu_0\rho}\frac{\partial^2}{\partial z^2}\left(\frac{\xi_\varphi}{R}\right) + \nu R^2B^2\frac{\partial^3 \xi_\varphi}{\partial t\partial\psi^2}. \tag{4.45}$$

4.3.1 Solution outside of the dissipative layer

The method of the matched asymptotic expansions (e.g. Bender and Orszag, 1978) is applied to the governing equations in order to derive the solution in the transitional region. Following this methodology, we separate the the transitional layer in the magnetic flux tube, into three different layers. The dissiaptive layer, where we consider kinematic viscosity is placed between two adjacent layers, where kinematic viscosity is neglected. Next, we seek for the solution to the studied to the linear dissipative MHD in the sandwiched layer and to the linear ideal MHD on adjacent layers and everywhere outside of it. Than, in accordance to this method, we pair in the region of validity the solutions of the exterior layers. Solutions in the dissipative and non-dissipative layers are known as internal and external solutions.

Now, we seek solutions to the linear MHD equations outside of internal layer, enveloped by the surface $\psi = \psi_A$. Such surface is known as the resonance surface. We employ the condition $V_A(\psi_A) = C_k$ to define ψ_A . We replace $P_i(\psi = \psi_i)$ for P in Equation (4.45), as the order of variation of P in transitional region is lP_i.Then, we apply Equations (4.38) and (4.39) on Equations (4.43)–(4.45) in the leading order approximation in terms of l to enable us to derive expression for $\widetilde{\mathcal{L}}$. Finally, we arrive at

$$R^2 \frac{\partial \hat{w}}{\partial \psi} + i\hat{\xi}_\varphi = 0, \tag{4.46}$$

$$k^2 \left(C_k^2 - V_A^2\right) \hat{w} = \frac{l^2 R B^2}{\rho} \frac{\partial \hat{P}}{\partial \psi}, \tag{4.47}$$

$$\left(C_k^2 - V_A^2\right) \hat{\xi}_\varphi = \frac{i\rho_i}{\rho_A} RS \left(C_k^2 - V_{Ai}^2\right), \tag{4.48}$$

where $V_A = B(\mu_0 \rho)^{-1/2}$ is the Alfvén speed and $\rho_A = \rho(\psi = \psi_A)$. When deriving Equations (4.47) and (4.48) we used the relation $\omega = C_k k$. It follows from Equation (4.48) that

$$\hat{\xi}_\varphi = \frac{i\rho_i RS(C_k^2 - V_{Ai}^2)}{\rho_A (C_k^2 - V_A^2)}. \tag{4.49}$$

We see that there is a singularity of $\hat{\xi}_\varphi$ at $\psi = \psi_A(t, z)$. Substituting Equation (4.49) in Equation (4.46) and integrating the obtained equation yields

$$\hat{w} = \begin{cases} \hat{w}(\psi = \psi_i) + \displaystyle\int_{\psi_i}^{\psi} \frac{S(C_k^2 - V_{Ai}^2)}{R(C_k^2 - V_A^2)} d\psi_1, & \psi < \psi_A, \\ \hat{w}(\psi = \psi_e) - \displaystyle\int_{\psi}^{\psi_e} \frac{S(C_k^2 - V_{Ai}^2)}{R(C_k^2 - V_A^2)} d\psi_1, & \psi > \psi_A. \end{cases} \tag{4.50}$$

While $\hat{\xi}_\varphi$ has a singularity of the form $(\psi - \psi_A)^{-1}$, $\hat{w}$ only has a logarithmic singularity. Finally, substituting this result in Equation (4.47) and integrating the obtained

equation results in

$$\hat{\Phi} = \begin{cases} \hat{\Phi}(\psi=\psi_i) + \dfrac{k^2(C_k^2-V_{Ai}^2)}{l^2RB^2}\displaystyle\int_{\psi_i}^{\psi}\left(\hat{w}(\psi=\psi_i) + \int_{\psi_i}^{\psi_1}\frac{S(C_k^2-V_{Ai}^2)}{R(C_k^2-V_A^2)}d\psi_2\right)d\psi_1, & \psi<\psi_A, \\ \hat{\Phi}(\psi=\psi_e) - \dfrac{k^2(C_k^2-V_{Ai}^2)}{l^2RB^2}\displaystyle\int_{\psi}^{\psi_e}\left(\hat{w}(\psi=\psi_e) - \int_{\psi_1}^{\psi_e}\frac{S(C_k^2-V_{Ai}^2)}{R(C_k^2-V_A^2)}d\psi_2\right)d\psi_1, & \psi>\psi_A, \end{cases} \tag{4.51}$$

where $\hat{\Phi}$ is defined by the equation

$$\frac{\partial\hat{\Phi}}{\partial\psi} = \frac{1}{\rho}\frac{\partial\hat{P}}{\partial\psi}. \tag{4.52}$$

It is easy to see that $\hat{P}$ is continuous at $\psi=\psi_A$.

4.3.2 Solution inside the dissipative layer

Here, we seek for solution in the internal layer enveloping the resonant surface. Initially Ruderman et al. (1995) concluded that solution nature in this internal layer is significantly influenced by the value of viscosity. Furthermore, it was later also confirmed by later studies (see also Ruderman and Roberts, 2002, Goossens et al., 2011). Unless the values of the viscosity are not very small there is a monotonic dependence of variable perturbations in the dissipative layer. On the other hand, in case the values of viscosity are significantly small, the nature of the dependence is oscillatory. A planar problem, to determine the regions where one type of solution transforms to another was investigated by Ruderman et al. (1995). The conclusion was that two parameters were of the great importance namely, inverse Reynolds number and the ratio of the transitional layer thickness on the wavelength of oscillation. Additionally the temporal damping of kink waves was analysed in the mentioned studies. More importantly with a slight effort it is possible to generalise these results for spacial damping in cylindrical geometry. Once we shift to cylindrical geometry instead of two parameters being of significant importance, we now have three such parameters: $\varepsilon = R_*/L_*$, l and the inverse Reynolds number Re^{-1}, where $\mathrm{Re} = R_*V_*/\nu$. Furthermore, the nature of spatial variation of variable perturbations in the internal dissipative layer is defined by $l(\varepsilon\mathrm{Re})^{1/3}$. Moreover, whenever $l(\varepsilon\mathrm{Re})^{1/3} \ll 1$ or whenever$l(\varepsilon\mathrm{Re})^{1/3} \gtrsim 1$ the spatial dependence of variable perturbations in the dissipative layer is monotonic or oscillatory respectively. We take the value of $l \gtrsim 0.1$, $\varepsilon \gtrsim 0.01$, while $\mathrm{Re} \gg 10^6$. These values are typical for the solar atmosphere, which is the main point of interest and emplyability of current study. Furthermore, we can conclude that $l(\varepsilon\mathrm{Re})^{1/3} > 1$. As a result we end up with oscillatory character of perturbations within small dissipative layer. Nevertheless, currently the way to find solution is cloudy, as equations governing the oscillations in the transitional layer posses high level of complexity. Fortunately, in case we determine the jumps of P and w across the small dissipative layer, we are able to describe the oscillation of the system. It was concluded by Ruderman et al. (1995) that viscosity does not affect the jumps across the small dissipative layer, whenever RE is sufficiently

large, to ensure that the transitional layer is much thicker than the dissipative layer. Later consecutive analysis (see, e.g. the review by Goossens et al., 2011), validated these conclusions. Moreover, whenever $l(\varepsilon\mathrm{Re})^{1/3} \ll 1$ the solution that depict the plasma motion, is comparatively straightforward in comparison to one with oscillatory relationship. As a result, we assume that independence of jumps across transitional layer on $l(\varepsilon\mathrm{Re})^{1/3}$ is still valid even for a non-stationary and expanding magnetic flux tube.

Now, let $l(\varepsilon\mathrm{Re})^{1/3} \ll 1$. Furthermore, the transitional layer is significantly thicker than dissipative layer. This allows to use first non-zero terms of Taylor expansion with respect to $\psi - \psi_A$ in order to approximate all equilibrium quantities. Particularly we substitute $\rho_A = \rho(\psi = \psi_A)$ for ρ and consider

$$C_k^2 - V_A^2 = -\Delta(\psi - \psi_A), \quad \Delta = \left.\frac{\partial V_A^2}{\partial \psi}\right|_{\psi=\psi_A}. \tag{4.53}$$

Since we assume that the density monotonically decreases in the radial direction in the transitional layer, it follows that $\Delta > 0$. Now, substituting Equation (4.38) in Equation (4.45), collecting terms of the order of l^{-2}, using Equations (4.42) and (4.53), and substituting $P(\psi = \psi_i)$ for P we obtain

$$\Delta(\psi - \psi_A)\hat{\xi}_\varphi + il\nu k^{-1} C_k R^2 B^2 \frac{\partial^2 \hat{\xi}_\varphi}{\partial \psi^2} = -\frac{i\rho_i}{\rho_A} RS\left(C_k^2 - V_{Ai}^2\right). \tag{4.54}$$

When deriving this equation we took into account that $\omega = C_k k$.

The thickness of the dissipative layer is defined by the condition that the two terms on the left-hand side of Equation (4.54) are of the same order. Using Equations (4.2) and (4.4) we easily obtain that this thickness is

$$\delta_A = \left(\frac{l\nu C_k}{kRB\Delta}\right)^{1/3} \sim lR_*(\varepsilon\mathrm{Re})^{-1/3}. \tag{4.55}$$

Then the condition that the thickness of the dissipative layer is much smaller than the thickness of the transitional layer reduces to $\varepsilon\mathrm{Re} \gg 1$. For typical conditions in the solar atmosphere this inequality is definitely satisfied. Together with the condition that the spatial behaviour of variable perturbations in the dissipative layer is non-oscillatory this gives

$$1 \ll \varepsilon\mathrm{Re} \ll l^{-3}. \tag{4.56}$$

The solution in the dissipative layer has to match the solution outside of this layer in the overlap layer defined by $\delta_A \ll |r - r_A| \ll lR_*$. Using Equation (4.49) we obtain that the solution in the overlap layer has the form

$$\hat{\xi}_\varphi = -\frac{i\rho_i RS(C_k^2 - V_{Ai}^2)}{\rho_A \Delta(\psi - \psi_A)} + \mathcal{O}\big((\psi - \psi_A)^{-2}\big). \tag{4.57}$$

Hence, the solution to Equation (4.54) must have this form for $|\psi - \psi_A| \gg R_* B_* \delta_A$. The solution to Equation (4.54) satisfying this condition is obtained in Appendix D.

It is given by Equation (D.6). Using Equation (D.1) we rewrite it as

$$\hat{\xi}_\varphi = -\frac{\rho_i S(C_k^2 - V_{Ai}^2)}{\rho_A B \Delta \delta_A} F(\Psi), \tag{4.58}$$

where

$$\Psi = \frac{\psi - \psi_A}{RB\delta_A}, \quad F(\Psi) = \int_0^\infty \exp\left(i\sigma\Psi - \tfrac{1}{3}\sigma^3\right) d\sigma. \tag{4.59}$$

Using Equations (4.58) and (4.59) we obtain from Equation (4.46)

$$\hat{w} = \frac{\rho_i S(C_k^2 - V_{Ai}^2)}{\rho_A R \Delta} G(\Psi), \tag{4.60}$$

where

$$G(\Psi) = \int_0^\infty \frac{e^{i\sigma\Psi} - 1}{\sigma} e^{-\sigma^3/3} d\sigma. \tag{4.61}$$

The functions $F(\Psi)$ and $G(\Psi)$ were introduced by Goossens et al. (2011).

Finally, substituting Equation (4.38) in Equation (4.44), collecting terms of the order of l^{-2}, and using the relation $\omega = C_k k$, and Equations (4.53) and (4.55), and (4.59)–(4.61) we obtain

$$\frac{\partial \hat{\Phi}}{\partial \Psi} = \frac{\rho_i k^2 S \delta_A^2 (C_k^2 - V_{Ai}^2)}{l^2 \rho_A} \left(\frac{dF}{d\Psi} - \Psi G(\Psi) \right). \tag{4.62}$$

4.3.3 Matching solutions

Here, we describe the matching method. We begin by considering the internal solution and seeking the asymptotic expansion that are valid for $\Psi \gg 1$. Then, similarly we seek for expansion of the external solution that is valid $|\psi - \psi_A| \ll BR^2$ and we substitute $\psi - \psi_A = RB\delta_A\Psi$ in this expansion. The condition that two solutions match is that the both obtained expansions agree with each other under approximation in the leading terms.

The performed analysis suggests that it is more beneficial jumps across the internal dissipative layer, rather than asymptotic expansions. Employing the condition $w(\Psi) - w(-\Psi)$ with $\Psi \gg 1$, we define the jump across the small dissipative layer w. Thus, we have

$$\begin{aligned} G(\Psi) - G(-\Psi) &= 2i \int_0^\infty \frac{\sin(\sigma\Psi)}{\sigma} e^{-\sigma^3/3} d\sigma \\ &= 2i \int_0^\infty \frac{\sin\sigma}{\sigma} \left[1 + \left(e^{-\sigma^3/3\Psi^3} - 1 \right) \right] d\sigma \\ &= \pi i + 2i \int_0^\infty \frac{\sin\sigma}{\sigma} \left(e^{-\sigma^3/3\Psi^3} - 1 \right) d\sigma. \end{aligned} \tag{4.63}$$

It is obvious that the second term in this expression tends to zero as $\Psi \to \infty$. Using this result we obtain from Equation (4.60) that the jump of $\hat{w}$ across the dissipative

layer is

$$\hat{w}(\Psi) - \hat{w}(-\Psi) = \frac{\pi i \rho_i S(C_k^2 - V_{Ai}^2)}{\rho_A R \Delta}[1 + o(1)]. \tag{4.64}$$

Using Equation (4.50) we obtain another asymptotic expression for the jump of $\hat{w}$ across the dissipative layer,

$$\hat{w}(\psi - \psi_A) - \hat{w}(\psi_A - \psi) = \delta\hat{w} - \mathcal{P}\int_{\psi_i}^{\psi_e} \frac{S(C_k^2 - V_{Ai}^2)}{R(C_k^2 - V_A^2)} d\psi + o(1), \tag{4.65}$$

where $\delta\hat{w} = \hat{w}(\psi = \psi_e) - \hat{w}(\psi = \psi_i)$ and $\mathcal{P}$ indicates the principal Cauchy part of an integral. This asymptotic expression is valid for $|\psi - \psi_A| \ll 1$. The leading terms of the two asymptotic expressions, one given by Equation (4.64) and the other by Equation (4.65), must coincide. It follows from this condition that

$$\delta\hat{w} = \frac{\pi i \rho_i S(C_k^2 - V_{Ai}^2)}{\rho_A R \Delta} + \mathcal{P}\int_{\psi_i}^{\psi_e} \frac{S(C_k^2 - V_{Ai}^2)}{R(C_k^2 - V_A^2)} d\psi. \tag{4.66}$$

Now we calculate $\delta\hat{\Phi} = \hat{\Phi}(\psi = \psi_e) - \hat{\Phi}(\psi = \psi_i)$. Using Equation (4.62) we obtain that the jump of P across the dissipative layer is given by

$$\hat{\Phi}(\Psi) - \hat{\Phi}(-\Psi) = \frac{\rho_i k^2 S \delta_A^2 (C_k^2 - V_{Ai}^2)}{l^2 \rho_A} \int_{-\Psi}^{\Psi} \left(\frac{dF}{d\Psi_1} - \Psi_1 G(\Psi_1) \right) d\Psi_1. \tag{4.67}$$

The integral on the right-hand side of this equation is evaluated in Appendix E. Using Eq. (E.8) we obtain

$$\hat{\Phi}(\Psi) - \hat{\Phi}(-\Psi) = -\frac{\pi i \rho_i k^2 S \delta_A (C_k^2 - V_{Ai}^2)\Psi^2}{2 l^2 \rho_A}[1 + o(1)]. \tag{4.68}$$

This result and the matching condition imply that the expansion with respect to $\psi - \psi_A$ of the jump of P across the dissipative layer calculated using the external solution must start from the term proportional to $(\psi - \psi_A)^2$. In particular, it follows from this condition that the term in this expansion proportional to unity must be zero. Using Equation (4.51) we write this condition as

$$\begin{aligned} \delta\hat{\Phi} &= \frac{k^2 (C_k^2 - V_{Ai}^2)}{l^2 R B^2} \Bigg[\int_{\psi_A}^{\psi_e} \left(\hat{w}(\psi = \psi_e) - \int_{\psi}^{\psi_e} \frac{S(C_k^2 - V_{Ai}^2)}{R(C_k^2 - V_A^2)} d\psi_1 \right) d\psi \\ &+ \int_{\psi_i}^{\psi_A} \left(\hat{w}(\psi = \psi_i) + \int_{\psi_i}^{\psi} \frac{S(C_k^2 - V_{Ai}^2)}{R(C_k^2 - V_A^2)} d\psi_1 \right) d\psi \Bigg]. \end{aligned} \tag{4.69}$$

where $\delta\hat{\Phi} = \hat{\Phi}(\psi = \psi_e) - \hat{\Phi}(\psi = \psi_i)$. Since $\delta\hat{w}/\hat{w} = \mathcal{O}(l)$ and we only need to calculate $\delta\hat{\Phi}$ in the leading order approximation with respect to l, we can substitute $\hat{w}(\psi = \psi_e) \approx \hat{w}(\psi = \psi_i) = RBS$. Then, noticing that the only quantity that depends on ψ in Equation (4.69) is V_A, each single integral is of the order of l, and each double

integral is of the order of l^2, we reduce this equation in the leading order approximation with respect to l to

$$\delta\hat{\Phi} = \frac{k^2 S(C_k^2 - V_{Ai}^2)(\psi_e - \psi_i)}{l^2 B}. \tag{4.70}$$

In case we initially disregard the jump of the pressure perturbations across the small transitional layer, the identical expression for $\delta\hat{\Phi}$ would be derived. Hollweg and Yang (1988) was the first to consider such an assumption as an *ad hoc*. More recently such proposition was formally validated in 1D plasma equilibrium by Goossens et al. (2011).

The value Φ is not changed across the transitional layer. Therefore, with the aid of the derived expression for Ψ and employing the ideal MHD equations. We conclude that Ψ is a continuous function in the whole transitional layer. As a result, applying Equation (4.70) on Equation (4.51) proves that the expression in the leading order approximation with the respect to l is applicable within whole transitional layer and is given by

$$\hat{\Phi} = \hat{\Phi}(\psi = \psi_i) + \frac{k^2 S(C_k^2 - V_{Ai}^2)(\psi - \psi_i)}{l^2 B}. \tag{4.71}$$

When deriving this expression we neglected the second terms in the brackets in Equation (4.51) because their ratios to the first terms are of the order of l. Using Equation (4.52) we obtain

$$\delta\hat{P} \equiv \hat{P}(\psi = \psi_e) - \hat{P}(\psi = \psi_i) = \frac{k^2 S(C_k^2 - V_{Ai}^2)}{l^2 B} \int_{\psi_i}^{\psi_e} \rho(\psi)\, d\psi. \tag{4.72}$$

Now we proceed to calculating $\widetilde{\mathcal{L}}$. We substitute $\eta = Se^{i\epsilon^{-1}\theta}$, $\delta\eta = (\delta\hat{w}/RB)e^{i\epsilon^{-1}\theta}$, and $\delta P = \delta\hat{P}\, e^{i\epsilon^{-1}\theta}$ in Equation (4.17). Then, using Equation (4.29) and the condition of very slow temporal density variation implying that $U_e \ll C_k$ we obtain

$$\widetilde{\mathcal{L}} = e^{i\epsilon^{-1}\theta}\left[l\frac{\delta\hat{P}}{R^2} - \frac{1}{2}(\rho_i - \rho_e)\omega^2 \left(S + l^{-1}\frac{\delta\hat{w}}{RB} \right) \right]. \tag{4.73}$$

Finally, using Eqs. (4.66) and (4.70) we arrive at

$$\widetilde{\mathcal{L}} = 2e^{i\epsilon^{-1}\theta}\omega C_k S(\rho_i + \rho_e)(\Upsilon - i\gamma), \tag{4.74}$$

where

$$\gamma = \frac{\pi k C_k^2 (\rho_i - \rho_e)^2}{8 l \rho_A B R^2 \Delta(\rho_i + \rho_e)}, \tag{4.75}$$

$$\Upsilon = \frac{k(\rho_i - \rho_e)}{4(\rho_i + \rho_e)} \left(-1 + \frac{C_k^2}{l\rho_i B R^2}\, \mathcal{P}\!\int_{\psi_i}^{\psi_e} \frac{\rho - \rho_i}{C_k^2 - V_A^2}\, d\psi \right). \tag{4.76}$$

§ 4.4 Derivation of governing equation for the wave amplitude

The wave evolution is described by Eq. (4.28) with $\mathcal{E}$ and $\widetilde{\mathcal{L}}$ given by Equations (4.30) and (4.74), respectively. We write $S = Ae^{i\chi}$. Then, substituting Equations (4.30) and

(4.74) in Equations (4.28), multiplying the obtained equation by $e^{-2i\chi}$, and separating the real and imaginary parts yields

$$\frac{\partial Q}{\partial t} + \frac{\partial (C_k Q)}{\partial z} = -2\gamma C_k Q, \tag{4.77}$$

$$\frac{\partial \chi}{\partial t} + C_k \frac{\partial \chi}{\partial z} = C_k \Upsilon, \tag{4.78}$$

where $Q = (\rho_i + \rho_e)\omega R^4 A^2$. Equation (4.77) determines the temporal and spatial dependence of the wave amplitude, while Equation (4.78) describes a small phase shift. We are mainly interested in the variation of the wave amplitude in space and time, so we do not use Equation (4.78) below.

§ 4.5 Wave propagation along a static and non-expanding waveguide

In this section we reproduce the results previously obtained for static and non-expanding waveguides. Hence, we assume that the tube radius is constant and equal to R.

4.5.1 Waveguide homogeneous in the axial direction

Below we investigate similar problem as the one considered Terradas et al. (2010). We study the resonant damping of kink waves propagating along a magnetic tube homogeneous in the axial direction. Radial direction, is the only one, for which density is assumed to be varied. In what follows we consider a driven harmonic wave at $z = 0$. This wave propagates in the region $z > 0$. In such scenario A is not dependent of time. Furthermore, employing Equation (4.77) yields $A = A_0 e^{-\gamma z}$.0 Here A_0 is the amplitude at $z = 0$. Applying the relation $\psi = \frac{1}{2} B r^2$ on equation Equation (4.53), leads to

$$\Delta = -\frac{B}{\mu_0 \rho_A^2 R} \frac{d\rho}{dr}\bigg|_A. \tag{4.79}$$

In this case both k and ω are constant. Hence, $\theta = kz - \omega t$, which implies that the wavenumber is $k_* = l^{-1}k$. Now, using Equation (4.79) and the relation $C_k = V_A(r_A)$ yields

$$\frac{\gamma}{k_*} = \frac{\pi(\rho_i - \rho_e)^2}{8R(\rho_i + \rho_e)|d\rho/dr|_A}. \tag{4.80}$$

This expression coincides with that obtained by Terradas et al., 2010 (see their equation (10) with $m = 1$).

4.5.2 Waveguide with the density varying in the axial direction

Resonant damping of a propagating along the expanding magnetic flux tube is examined in this section. Soler et al. (2011c) was the fist one to investigate such problem. The aim is reproduce the results obtained previously. In what follows, we suppose that $\rho_i(z)/\rho_e(z) = \zeta = \text{const}$ and $\rho(r, z)/\rho_e(z) = f(r)$. Formerly, these assumption were made by Dymova and Ruderman (2006) and by Soler et al. (2011c) in order to study

resonant damping of standing and propagating kink waves, respectively. Furthermore, we suppose that at $z = 0$ both amplitude A_0 of the kink wave with and the constant frequency ω are driven. We now have C_k as a function of z. As a result we can conclude that the wavenumber, $k(z) = \omega/C_k(z)$, is also the function of z. We should note that in original non-scaled variables the wavenumber can be written as $k_*(z) = l^{-1}k(z)$.

Since Q is again independent of t it immediately follows from Equation (4.77) that

$$A = A_0\sqrt{\frac{C_k}{C_f}}\exp\left(-\int_0^z \gamma(z_1)\,dz_1\right). \tag{4.81}$$

When deriving this equation we used the relation $\rho_i C_k^2 = \rho_f C_f^2$. Equation (4.79) remains valid. Then, using the relation $\rho(r, z) = f(r)\rho_e(z)$ we obtain from Equation (4.75)

$$\gamma = \frac{\omega(\zeta - 1)}{2\pi\mathcal{G}(\zeta + 1)C_k(z)}, \tag{4.82}$$

where

$$\mathcal{G} = \frac{4lR|f'(r_A)|}{\pi^2(\zeta - 1)}. \tag{4.83}$$

$\mathcal{G} = 4/\pi^2$ for the linear density profile, and $2/\pi$ for the sinusoidal density profile. After substituting Equation (4.82) in Equation (4.81) we obtain the equation coinciding with equation (38) in Soler et al. (2011c).

§ 4.6 Wave propagation along an expanding and non-stationary waveguide

As an example of application of the general theory we consider a generalisation of the same problem that was studied by Soler et al. (2011c), and take the loop expansion and cooling into account. We first describe the general method for studying the wave propagation, and then apply it to a particular loop with given cross-section radius and density variation along the tube, and the temporal density variation.

4.6.1 General theory

We assume that a kink wave is driven at one of the loop footpoins and impose the boundary condition

$$\omega = \omega_0, \quad A = A_0 \quad \text{at} \quad z = 0. \tag{4.84}$$

Driving starts at $t = 0$. Before that the loop is at rest, so we also have the initial condition

$$A = 0 \quad \text{at} \quad t = 0. \tag{4.85}$$

The equations describing the wave propagation are solved for $t > 0$ and $z > 0$.

We start from calculating $\theta(t, z)$. It follows from the dispersion equation $\omega = C_k k$ that $\theta(t, z)$ satisfies the equation

$$\frac{\partial\theta}{\partial t} + C_k(t, z)\frac{\partial\theta}{\partial z} = 0. \tag{4.86}$$

Since $\theta(t,z)$ is defined with the accuracy up to an additive constant we can take $\theta(0,0) = 0$. Then it follows from Eq. (4.84) that

$$\theta = -\omega_0 t \quad \text{at} \quad z = 0. \tag{4.87}$$

Since the loop is at rest at $t = 0$ we can take

$$\theta = 0 \quad \text{at} \quad t = 0. \tag{4.88}$$

The equation of characteristics of Equation (4.86) is

$$\frac{dz}{dt} = C_k(t,z). \tag{4.89}$$

With the aid of Equation (4.86) we have $\theta = \text{const}$ along a characteristic. To proceed further, characteristic is considered to begin at origin of coordinate system. We assume that such characteristic is defined by equation $z = z_b(t)$, where $z_b(0) = 0$. Such characteristic separates two region namely: the perturbed and unperturbed regions in the (t,z)-plane. Therefore, in what follow it will be called the boundary characteristic. Now we can study a point with coordinates (t_1, z_1), where $z_1 > z_b(t_1)$. Therefore, this point is above the boundary characteristic that. As a result the characteristic passing through point (t_1, z_1) would originate from z-axis, as it cannot cross the boundary characteristic. Thus, employing Equation (4.88) yields $\theta(t_1, z_1) = 0$.

Then we consider another point (t_1, z_1), where $z_1 < z_b(t_1)$. That means that (t_1, z_1) is placed below the characteristic boundary. We now consider the characteristic $t = \tau(t_1, z_1)$ that pass through this point and is originated on the t-axis. Thus, $\theta(t_1, z_1) = -\omega_0\tau(t_1, z_1)$. Therefore, we able to determine $\theta(t,z)$ in the whole region $t > 0$, $z > 0$. We differentiate $\theta(t,z)$ with respect to t to derive ω. As a result, $k = \omega/C_k$.

Next we proceed to solving Equation (4.77). The equation of characteristics of this equation is also Eq. (4.89). The variation of Q along the characteristic is defined by

$$\frac{dQ}{dt} = -\left(2\gamma C_k + \frac{\partial C_k}{\partial z}\right) Q. \tag{4.90}$$

After substituting in this equation a solution to Equation (4.89) found when calculating $\theta(t,z)$, Equation (4.90) becomes the equation determining the variation of Q along a characteristic. The solution to this equation must satisfy the initial condition

$$Q = (\rho_i + \rho_e)\omega_0 R^4 A_0^2 \quad \text{at} \quad t = \tau(t_1, z_1). \tag{4.91}$$

In this equation the equilibrium quantities are calculated at $t = \tau$ and $z = 0$.

We now consider (t_1, z_1) with $z_1 > z_b(t_1)$, which implies that it is above the boundary characteristic. In that case the characteristic that contains this point starts at the z-axis where $A = 0$. Then it follows that $A(t_1, z_1) = 0$, that is the tube is at rest for $z > z_b(t)$. Hence, the equation $z = z_b(t)$ describes the propagation of the wave front along the magnetic tube. Below we apply the general theory to particular cases.

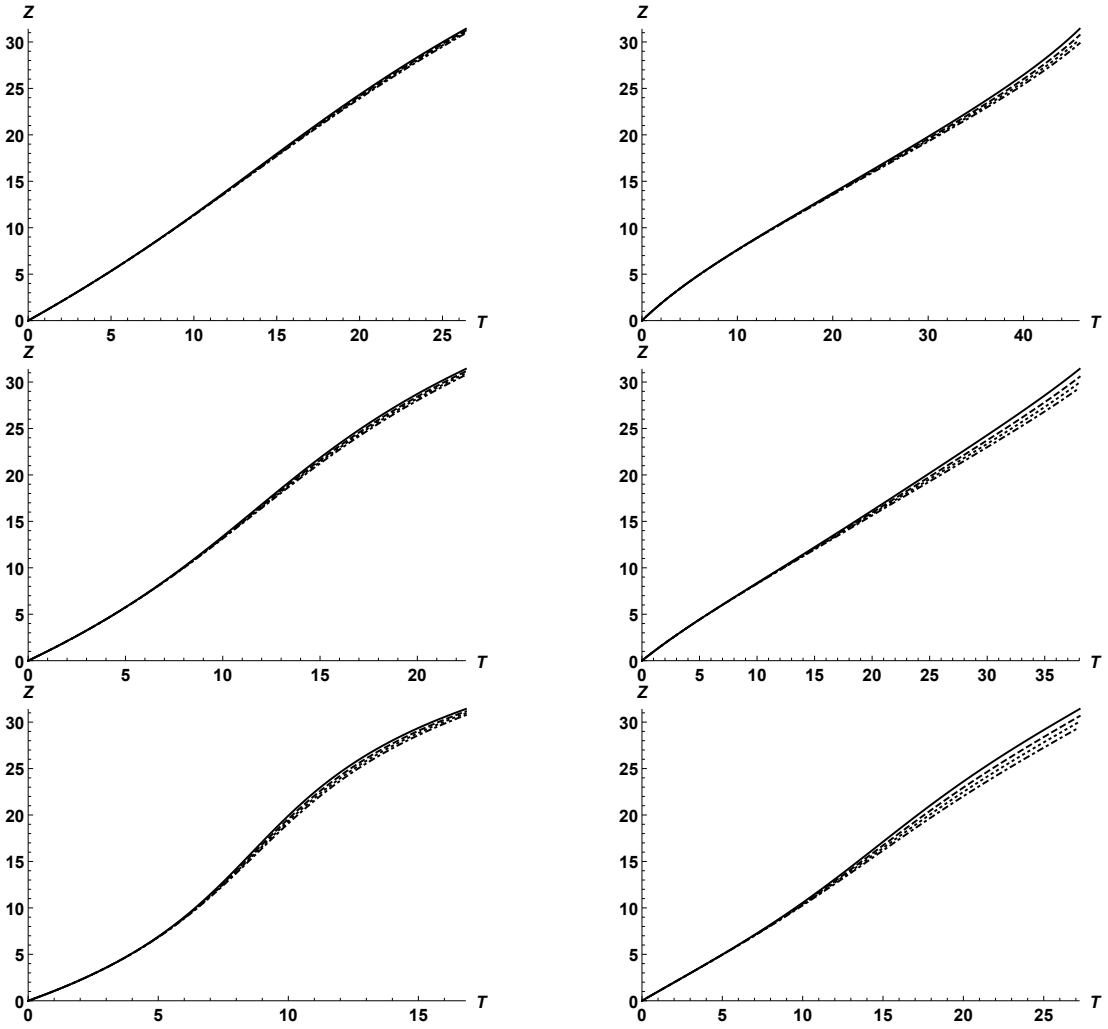

Figure 4.2: Dependence of the wave front position on time. The calculations continued until the wave front reaches the other end of the magnetic tube. The left panels correspond to $\lambda = 1$ and the right to $\lambda = 1.5$. The upper, middle, and lower panels correspond to $\kappa = 0.5$, $\kappa = 1$, and $\kappa = 2$, respectively. The solid, dashed, dotted, and dash-dotted curves correspond to $\mathcal{N} = 1/3$, $\mathcal{N} = 0.2$, $\mathcal{N} = 0.1$, and $\mathcal{N} = 0$, respectively.

4.6.2 Wave propagation in cooling and expanding coronal loop

Below coronal loop is located in isothermal atmosphere is assumed to be of half-circle shape. Furthermore, we consider propagation of the kink wave. Moreover, the coronal loop is considered to be in a vertical plane. We assume that cooling occurs inside the expanding magnetic flux tube only, whereas outside the loop the temperature remains constant. We recall that cooling outside the expanding magnetic flux tube is much slower than inside the expanding magnetic flux tube, making such assumption viable.

that outside the loop. Then we use barometric formula to determine density both inside and outside the expanding magnetic flux tube, by

$$\rho_i = \rho_f \exp\left(- \frac{L}{\pi H(t)} \sin \frac{\pi z}{L} \right), \quad \rho_e = \frac{\rho_f}{\zeta} \exp\left(- \frac{L}{\pi H_0} \sin \frac{\pi z}{L} \right), \tag{4.92}$$

where L is the length of the loop. Following to Aschwanden and Terradas (2008) and Ruderman (2011b,c) we assume that the plasma density inside the loop decreases exponentially, so that

$$H(t) = H_0 e^{-t/t_c}. \tag{4.93}$$

Although mechanism of coronal loops cooling are important they are not discussed in this section, as we concentrate more on seismological results. Furthermore, we should note that radiation is the main mechanism of heat exchange in typical coronal loops with the temperature of the around or below 1.5 MK. Transverse oscillations of coronal loops in the presence of radiative cooling were investigate numerically by Magyar et al. (2015). There was no information about the temporal dependence of temperature. Despite that fact, the results presented in that work with regards temporal dependence of kink oscillations amplitude are generally in agreement with the one presented by Ruderman (2011b,c). The later investigations considered magnetic flux tube with exponentially decaying temporal dependence. Therefore, we have additional validation to use exponential decay temporal dependence as acceptable approximation. Moreover, we suppose that the pressure in surrounding plasma and within the loop is in equilibrium. Such assumption does not add any considerable additional restriction on plasma parameters, as magnetic forces are dominant under typical coronal conditions.

Now, we generalise a model of expanding coronal loop first introduced by Ruderman et al. (2008), and then adopted by Shukhobodskiy and Ruderman (2018) and Shukhobodskiy et al. (2018). In such configuration the cross-section radius of the expanding magnetic flux tube can be taken to be

$$R(z) = R_f \lambda \sqrt{\frac{\cosh(L/2l_c) - 1}{\cosh(L/2l_c) - \lambda^2 + (\lambda^2 - 1)\cosh(z/l_c - L/2l_c)}}, \tag{4.94}$$

where $\lambda = R(L/2)/R_f$ is expansion factor and l_c is a arbitrary parameter with the dimension of length. In order to perform numerical analysis we take $l = 0.2$ and $L/l_c = 6$. Furthermore, our numerical model must satisfy the condition $\mathcal{N} = L(t_c C_f)^{-1} \ll 1$. That means the previously made assumption that the flow speed induced by cooling is much lower than the phase speed is satisfied

The goal of this section is to determine the effect of cooling on the kink wave propagation in the expanding coronal loop. As cooling act in reduction of value of ρ_i at the same time it influence the increase of the value C_k. As a result, the increase in the cooling speed amplifies the speed the wave perturbation driven at one footpoint at $t = 0$. Thus the wave reaches the opposite footpoint in faster pace. We have investigated numerically the kink wave propagation for in four scenarios: no cooling , slow cooling, moderate cooling and strong cooling with $\mathcal{N} = 0$, $\mathcal{N} = 0.1$, $\mathcal{N} = 0.2$ and

$\mathcal{N} = 1/3$ respectively. When $\mathcal{N} = 1/3$, so that we have strong cooling, we suppose that the wave front reaches at the opposite footpoint at the time $t = t_{\rm end}$. As a result, for other cases the wave front reaches at the other footpoint later so that $t > t_{\rm end}$. We numerically found the spatial dependence of the wave frequency at $t = t_{\rm end}$. We also numerically calculated wavenumber at $t = t_{\rm end}$. We have also calculated the amplitude at $t = t_{\rm end}$. It follow from Equation. (4.21) and characteristic oscillation time that at $z = 0$ the wave frequency is $l^{-1}\omega_0$ and the wavenumber is $l^{-1}\omega_0/C_f$. In our calculation we assumed the wavelength at $z = 0$ to be equal to one fifth of L. Thus we have $L = 10\pi l C_f/\omega_0 = 2\pi C_f/\omega_0$.

We introduce the dimensionless variables and parameters,

$$T = \frac{t\omega_0}{l},\ Z = \frac{z\omega_0}{lC_f},\ \Omega = \frac{l\omega}{\omega_0},\ K = \frac{lkC_f}{\omega_0},\ T_{\rm end} = \frac{t_{\rm end}\omega_0}{l},$$
$$\kappa = \frac{L}{\pi H_0},\ \alpha = \frac{\mathcal{N}}{10\pi} = \frac{L}{10\pi t_c C_f}. \tag{4.95}$$

Using the relation $BR^2 = \text{const}$ we obtain

$$C_k^2 = \frac{C_f^2 R_f^4(\zeta+1)}{R^4[\zeta\exp(-\kappa e^{\alpha T}\sin(0.1Z)) + \exp(-\kappa\sin(0.1Z))]}. \tag{4.96}$$

Then the characteristic Eq. (4.89) reduces to

$$\frac{dZ}{dT} = \frac{R_f^2\sqrt{\zeta+1}}{R^2\sqrt{\zeta\exp(-\kappa e^{\alpha T}\sin(0.1Z)) + \exp(-\kappa\sin(0.1Z))}}. \tag{4.97}$$

Equation $Z_b(T_{\rm end}) = \omega_0 L(lC_f)^{-1}$, where $Z_b(T)$ is the solution to Equation (4.97) with $\alpha = 1/30\pi$ satisfying the initial condition $Z_b(0) = 0$ is employed to determine the $T_{\rm end}$. Employing Equation (4.97) we found numerically the temporal dependence of the wave front position for various values of κ and λ. Such dependence presented in Fig. 4.2. Thus, we can conclude that faster is the cooling the greater is the speed of the wave front. Such result was expected since cooling enhances the phase speed C_k see Fig. 4.3. As time passes the density in the loop deceases. That means less energy is required for propagating wave to reach the end of the magnetic flux tube. We can also see that the effect of cooling is rather weak, although the tube expansion makes it more pronounced.

Now, numerically calculated spacial dependence of the of the dimensionless frequency Ω for various values of λ, Ω, and κ is presented in Figs. 4.4. Similarly, the spacial dependence of the wavenumber K for various values of λ, Ω, and κ is depicted on 4.5. In case there is no cooling the frequency remains constant, as it should be. Moreover, in case cooling is present the frequency grows with as the distance between waves and footpoints increase, whenever the loop has a constant cross-section. Moreover, the general conlcusion is the faster is the cooling rate the more definite such phenomenon is. Despite this, such effect is very moderate or weak. On the other hand

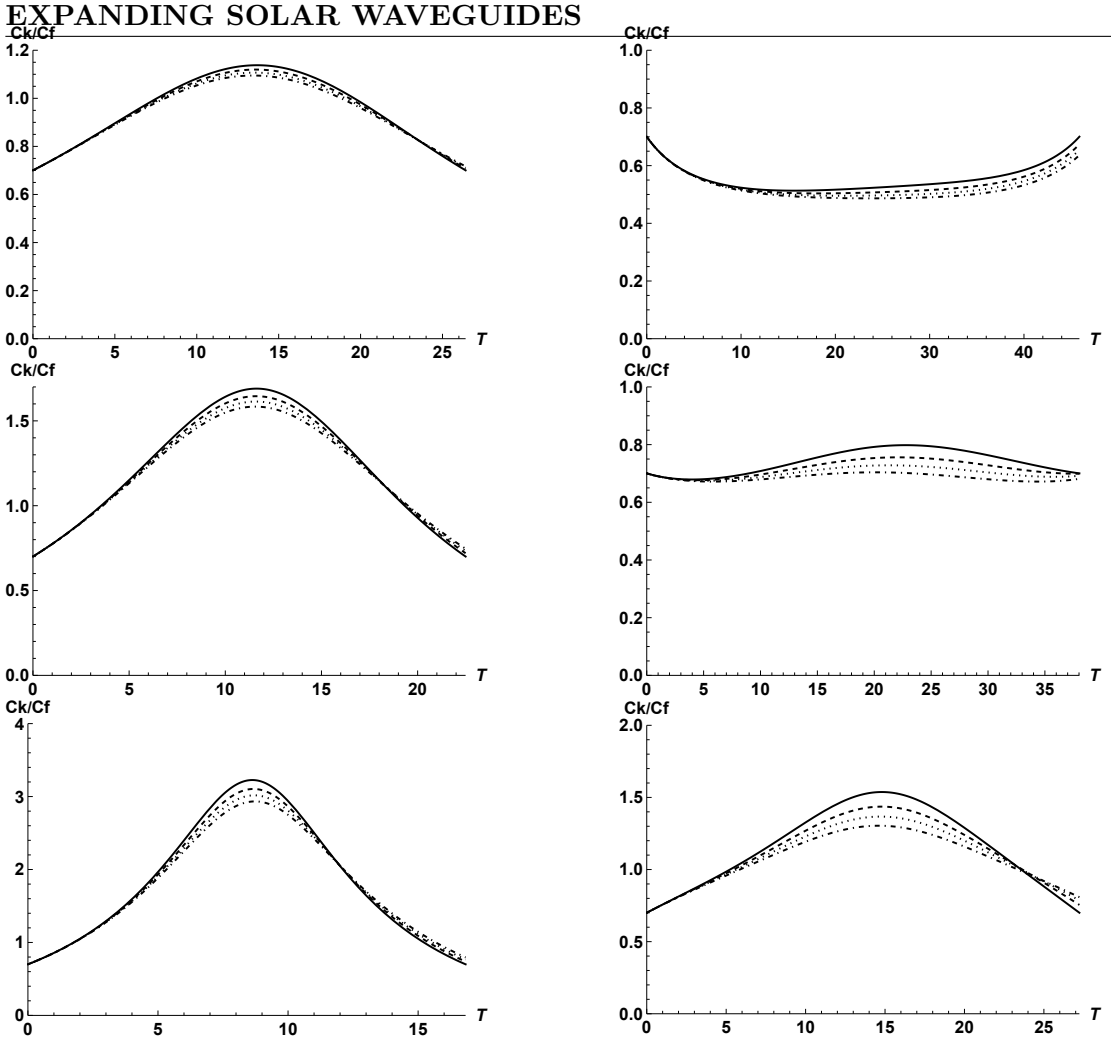

Figure 4.3: Dependence of the dimensionless phase speed on the distance along the loop for $t = t_{\rm end}$. The left panels correspond to $\lambda = 1$ and the right to $\lambda = 1.5$. The upper, middle, and lower panels correspond to $\kappa = 0.5$, $\kappa = 1$, and $\kappa = 2$, respectively. The solid, dashed, dotted, and dash-dotted curves correspond to $\mathcal{N} = 1/3$, $\mathcal{N} = 0.2$, $\mathcal{N} = 0.1$, and $\mathcal{N} = 0$, respectively.

the dependence of frequency on the cooling strength is significantly more pronounced in a loop undergoing expansion.

We can conclude that such effect is more powerful whenever we consider an expanding magnetic flux tube with loop been significantly higher than the atmospheric scale height. The similar pattern could be noticed in the numerical results for the wavenumber computation. Cooling of the magnetic flux tube almost does not affect the propagating wave unless the loop has expansion, where such effect is notable.

Finally, the variation of the amplitude along the loop is presented on Fig. 4.6. We

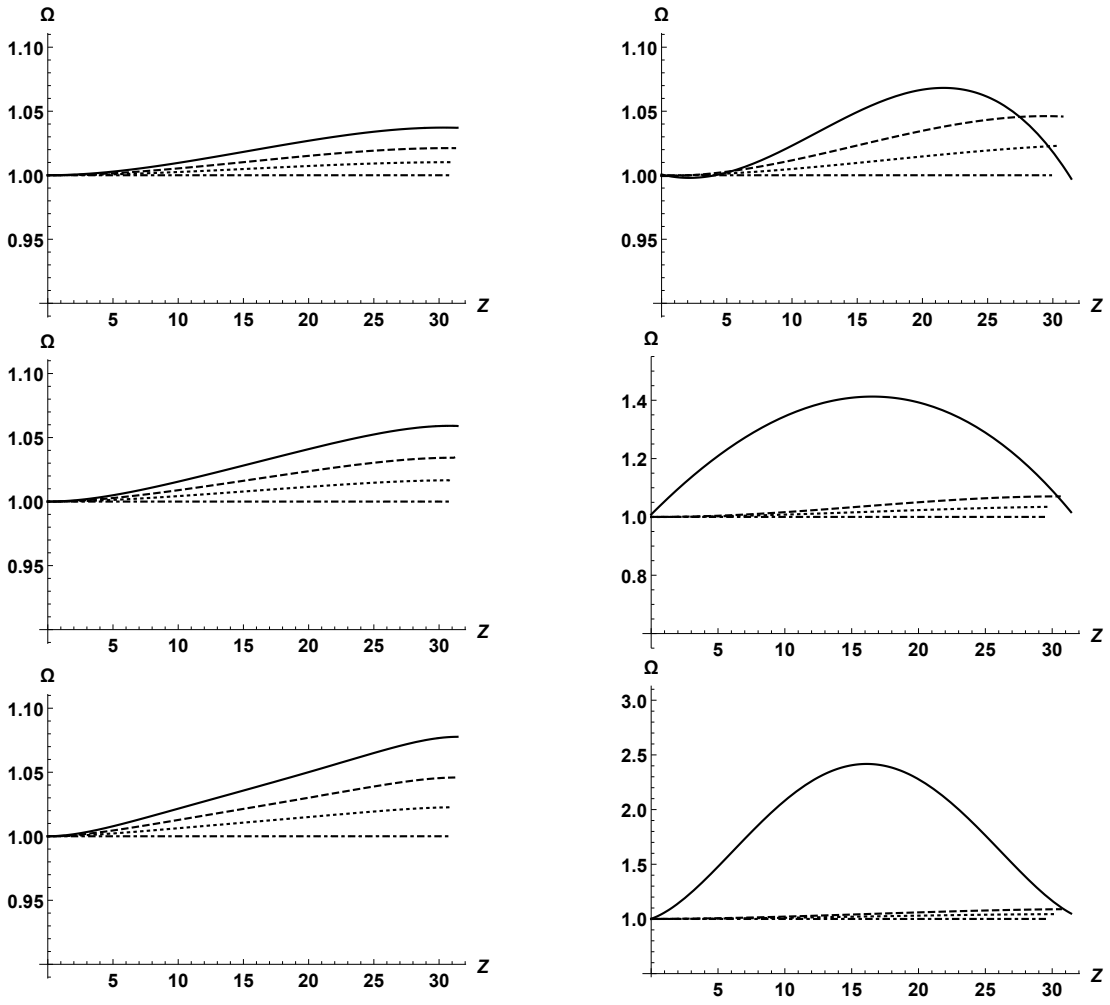

Figure 4.4: Dependence of the frequency on the distance along the loop for $T = T_{\rm end}$. The left panels correspond to $\lambda = 1$ and the right to $\lambda = 1.5$. The upper, middle, and lower panels correspond to $\kappa = 0.5$, $\kappa = 1$, and $\kappa = 2$, respectively. The solid, dashed, dotted, and dash-dotted curves correspond to $\mathcal{N} = 1/3$, $\mathcal{N} = 0.2$, $\mathcal{N} = 0.1$, and $\mathcal{N} = 0$, respectively.

draw the conclusion that, in the majority of instances there is initial increase of the amplitude followed by later decay. We can see that similarly to Ruderman (2011b,c), Ruderman et al. (2017), and Shukhobodskiy et al. (2018) where standing kink waves were considered, the amplitude increase due to stratification constitute a competition with decay due to resonant damping. Furthermore, the same conclusion is drawn, that cooling always results in kink waves amplification.

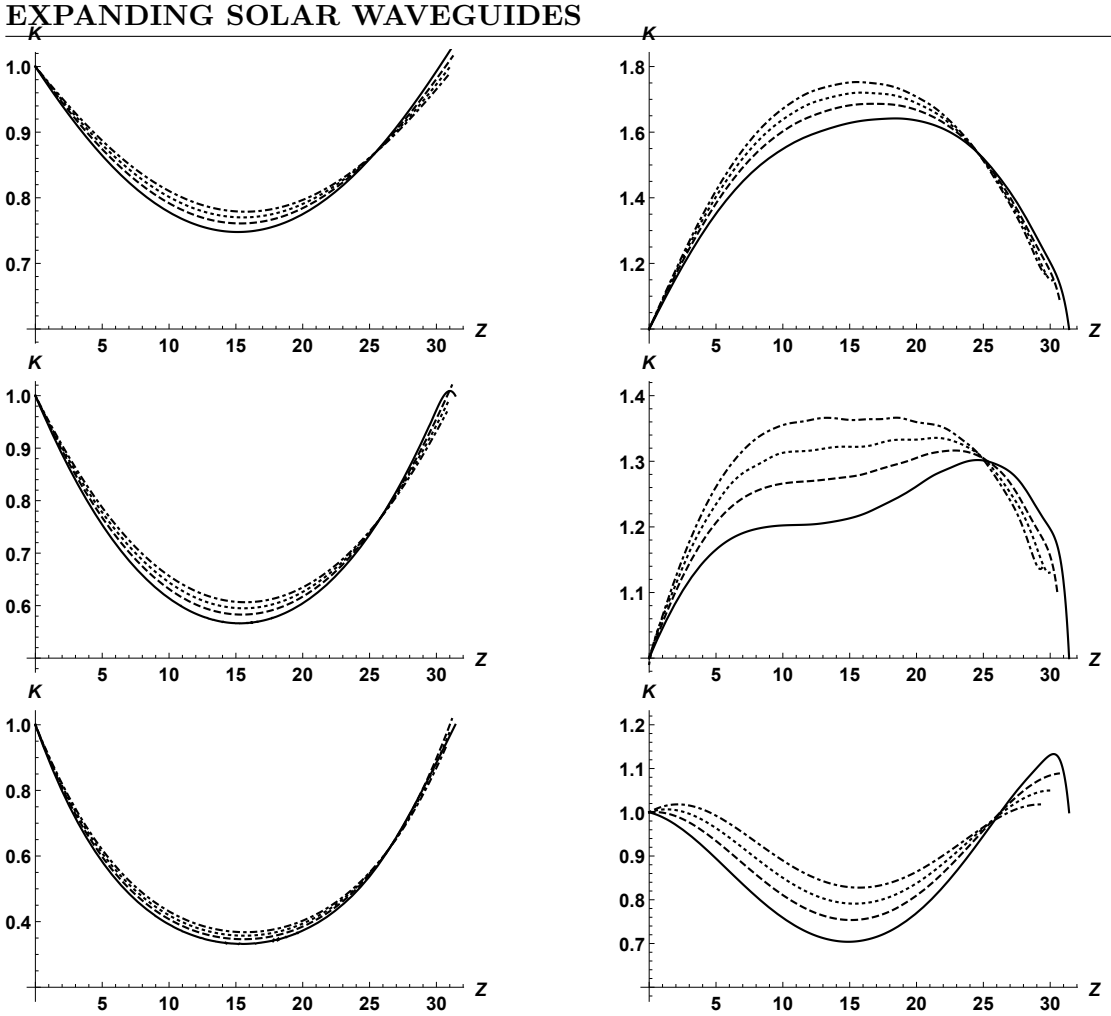

Figure 4.5: Dependence of the wave number on the distance along the loop for $t = t_{\rm end}$. The left panels correspond to $\lambda = 1$ and the right to $\lambda = 1.5$. The upper, middle, and lower panels correspond to $\kappa = 0.5$, $\kappa = 1$, and $\kappa = 2$, respectively. The solid, dashed, dotted, and dash-dotted curves correspond to $\mathcal{N} = 1/3$, $\mathcal{N} = 0.2$, $\mathcal{N} = 0.1$, and $\mathcal{N} = 0$, respectively.

§ 4.7 Summary

In this chapter the effect of the kink wave propagating along the expanding magnetic flux tube, with spacial and temporal variation of density was investigated. The double layered expanding magnetic flux tube is composed of the internal core layer and external transitional layer. Within the core layer the density dependence on the radial coordinate is almost non-existent. However, the density decreases from its values in the core layer the the surrounding plasma within transitional region. Moreover, the

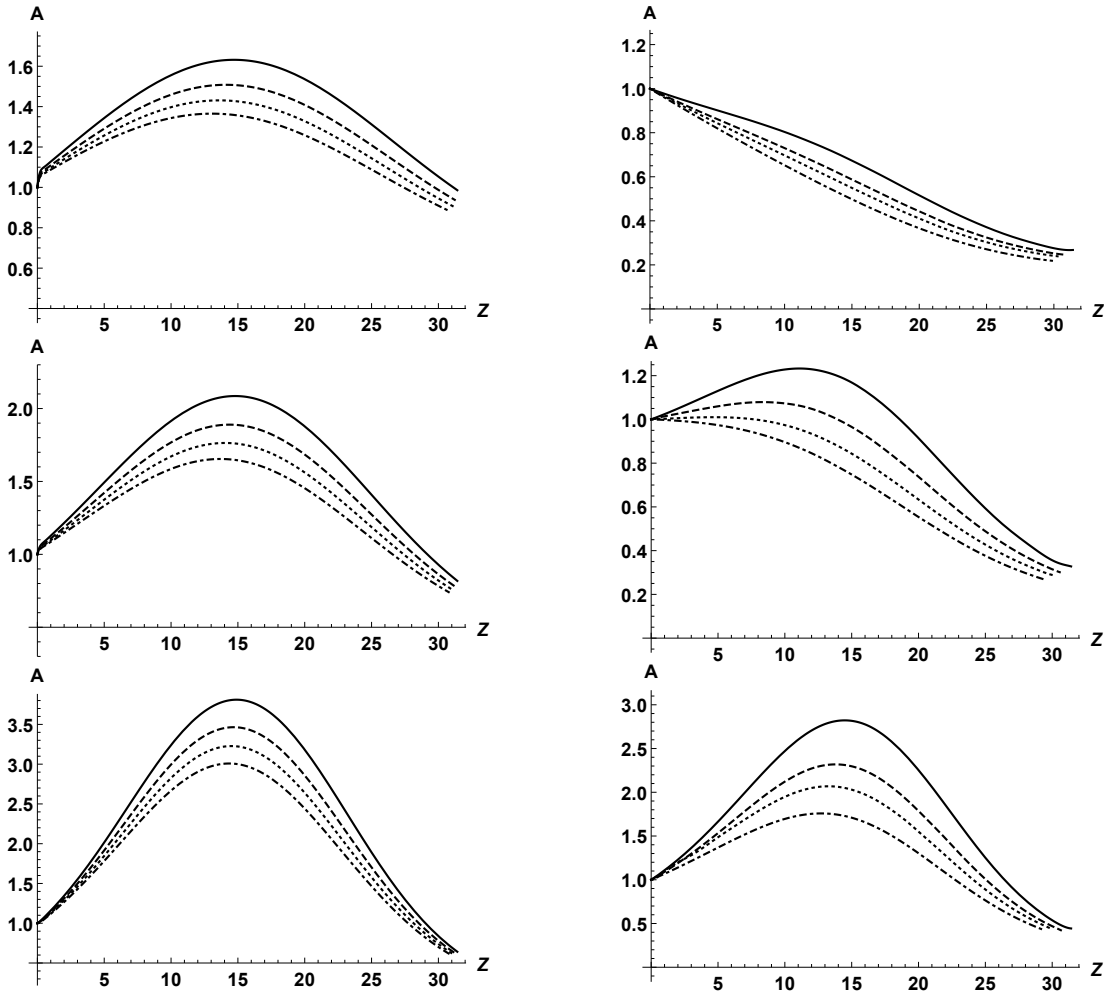

Figure 4.6: Dependence of the amplitude on the distance along the loop for $t = t_{\rm end}$. The left panels correspond to $\lambda = 1$ and the right to $\lambda = 1.5$. The upper, middle, and lower panels correspond to $\kappa = 0.5$, $\kappa = 1$, and $\kappa = 2$, respectively. The solid, dashed, dotted, and dash-dotted curves correspond to $\mathcal{N} = 1/3$, $\mathcal{N} = 0.2$, $\mathcal{N} = 0.1$, and $\mathcal{N} = 0$, respectively.

thickness of the transitional layer is assumed to be much thinner than the radius of the magnetic flux tube. We have employed both the cold plasma, thin tube and short wave approximations. Thus, the wavelength is both much larger than the tube radius and on contrary the characteristic scale of the density and tube variation along the expanding magnetic flux tube are much larger than the wavelength. With the aid of WKB method we derived the equation governing such system as well as found the expressions that could be numerically solved in order to find the spacial and temporal relations of the wave amplitude.

Initially we considered the kink wave propagation in a homogeneous in the axial direction magnetic flux. That allowed us to replicate and validate the results previously reported by Terradas et al. (2010). That allowed us to conclude that there was only one phenomenon that influences the wave damping and it is the resonsant absorption.

Afterwards, we investigated the kink wave propagation in a magnetic flux tube where the density had axial spacial dependence. In this scenario we were able to reproduce the results and the analysis of Soler et al. (2011c) and conclude that wave propagation has influence both from the axial ingomogeneity and the resonance absorption

Lastly, the kink wave propagation in an expanding and non-stationary magnetic flux tube, was considered and studied. First of all, we obtained the general expressions for longitudinal and time variation of and amplitude. We also derived the expression of spacial and temporal dependence for the phase speed. Furthermore, we have derived such expressions both for wave frequency and wavenumber. Afterwards, we employed on the particular case of a kink wave propagation along the a cooling coronal loop the general theory. The loop was considered to be present in an isothermal atmosphere and to have a half-circle shape. We also assumed that the temperature of plasma within the loop decays exponentially. On the other hand, the temperature of the exterior plasma remains constant. We employed the dependence of the loop cross-section on the distance along loop as in Ruderman et al. (2008, 2017) and Shukhobodskiy et al. (2018). This dependece is only valid for non-twisted coronal loops, with potential background magnetic field. Then, the governing equations of the model, were solved numerically. We considered that the driver of the was is located in one of the footpoints and in the same time cooling is initialised. The fundamental goal of this chapter was to investigate the dependence of the wave properties on the cooling strength. The temporal dependence of the distance that the wavefront travels was investigated initially. We concluded the more intense the cooling is the further wavefront migrates at a given time. Furthermore, we showed that the phase speed is amplified by cooling. Thus making the results for the wavefront to be anticipated as phase speed would move wavefront faster. Moreover, the dependence of both the wave frequency and the wavenumber on the distance along the tube, was numerically computed and presented. In order to present such information, we have specifically selected the moment of time whenever the wavefront in the strondest colling scenario arrives at the footpoint on the other side As a result, we have confirmed that the cooling enhances the frequency of the propagating wave. However, the results are inconclusive for the effect of cooling on the wavenumber. At the end, we studied the longitudinal dependence of the wave amplitude. The results to be found were analogous to one formerly obtained for standing kink waves. The result is that the cooling is enhancing the wave amplitude and competing with the effect of resonant damping.

Chapter 5

Significance of Cooling Effect On Comprehension of Kink Oscillations of Coronal Loops

§ 5.1 Observations - Event Selection and Model Fitting

The aim of this chapter is to understand whether a range of damping profiles of kink mode oscillations can be explained by the effects of cooling and to compare this model to several other previously studied models. To tackle this aim, we selected 10 events randomly from the sample identified to damp with both exponential and non-exponential components in the statistical study of Goddard et al. (2016) for analysis. The combination of exponential and non-exponential components implies a level of complexity in the amplitude profiles through time which could be an observational signature of cooling. Each of these 10 examples of kink-mode oscillations were sampled by the SDO/AIA instrument at discrete times between 3rd November 2010 and 18th July 2013, with the periods of these oscillations ranging from slightly over 2 minutes up to nearly 16 minutes. Here, we specifically study data from the 171 Å filter which samples the coronal plasma at temperatures of around 0.6 MK with a cadence of 12 s and a pixel scale of 0.6". A 300" $\times$ 300" field-of-view (FOV) around each oscillation was downloaded for a one-hour time-series beginning 15 minutes before the oscillation was deemed to have begun in Goddard et al. (2016) using the *ssw_cutout_service.pro* routine. Frames from the SDO/AIA instrument can have reduced exposure times during flares resulting in frames being dropped during download. Therefore, we filled any gaps in the time-series with synthetic images generated by averaging the intensities in the previous and following frames at each pixel. Since no consecutive frames were dropped, this should have no effect on the identification and analysis of oscillations with periods of the order minutes. Time-distance diagrams were then constructed to mimic the slits studied in Goddard et al. (2016), with a width of 5 pixels. In Tab. 5.1, we detail the basic information of the 10 oscillations studied in this chapter. We should also note that Pascoe et al. (2017) have extensively studied density contrast for the event 40 02.

Event ID	Loop ID	Slit position [x1, y1, x2, y2] (arcsec)	Date	Time UT	Period (min)	Osc amp (Mm)
03	01	$-977, -383, -988, -368$	2010-Nov-03	12:13:48	2.46 ± 0.03	4.7
03	02	$-970, -416, -1001, -393$	2010-Nov-03	12:14:35	3.62 ± 0.08	9.7
04	01	$912, 405, 889, 433$	2011-Feb-09	01:30:02	2.29 ± 0.03	4.4
26	01	$1098, 13, 1126, 51$	2012-Jan-16	00:08:28	11.95 ± 0.13	9.2
40	02	$-1077, -121, -1065, -96$	2012-Oct-20	18:09:33	5.61 ± 0.03	4.4
40	04	$-1045, -114, -1020, -110$	2012-Oct-20	18:10:08	5.53 ± 0.04	2.5
40	07	$-1107, -153, -1094, -121$	2012-Oct-20	18:11:11	5.72 ± 0.06	3.4
40	08	$-1036, -217, -1066, -194$	2012-Oct-20	18:08:39	4.33 ± 0.08	12.1
43	05	$801, 608, 812, 631$	2013-Jan-07	06:37:11	4.5 ± 0.02	2.2
48	01	$-1076, 77, -1044, 111$	2013-Jul-18	17:59:56	15.28 ± 0.16	22

Table 5.1: Properties of the kink-mode oscillations studied here. The information given is in the same format as in Tab. A1 from Goddard et al. (2016) for consistency with the previous literature. Note the estimation of period and apparent oscillation amplitude (later in the text we do not use the word "apparent" in front of the amplitude) are from Goddard et al. (2016) and are not estimated directly in this chapter. These are included for comparison with Fig. 5.2.

Furthermore, comprehensive temporal analysis was performed by Goddard and Nisticò (2020) for the event 03 01.

In Fig. 5.1, we plot the time-distance diagrams constructed for each of the events studied here (using the routine detailed in Krishna Prasad et al. 2012) over the course of one hour. Each slit has a different length, however, they have all been scaled to the same y-axis to emphasise the oscillations. The blue dots over-laid on each panel indicate the edges of the loop, identified using the Canny edge-detection method in Wolfram Mathematica 12. The red dots in each panel indicate the mid-points between the detected edges that we infer to be the central axis of the oscillating loop here. The background trend was then accounted for by fitting a function, using spline fitting, through the averages between local extremum points, similar to the method described in Pascoe et al. (2016c). Once the background trend had been subtracted, the amplitudes of the oscillations were normalised and fitted with a sum of Gaussian profiles of the form:

$$f(amp) = \sum_{i=1}^{n} A_i \exp[-(\mu_i + t)^2/(2\sigma_i^2)]/\sqrt{2\pi}/\sigma_i^2, \tag{5.1}$$

where A_i and μ_i, and σ_i are the amplitude, shift, and width of the profile fitted to each peak. The value of n corresponds to the number of extrema identified for each oscillation. To ensure that the summed functions maintain continuity, we used the Wolfram Mathematica 12 function *Non-linearModelFit*. The benefit of fitting Gaussians to each extrema profile independently is that no implicit periodicity needs to be assumed for the oscillations. All of these steps allow us now to estimate the damping profile of each oscillation that can be modelled using the theories described in Shukhobodskiy

et al. (2018). The procedure described here is essentially similar to that used in Nelson et al. (2019), but with the exception of an updated background trend approximation.

§ 5.2 Results

5.2.1 Theoretical Model

In this chapter, we expand on the work of Nelson et al. (2019) by applying the model proposed by Shukhobodskiy et al. (2018) to analyse 10 complex kink-mode oscillations. Here, let us provide a brief summary of the theoretical model for completeness. We consider an expanding and cooling loop of semi-circular shape surrounded by an annulus layer which is fixed in the dense photosphere. We note that the effects of curvature are only applied to the density distribution meaning, essentially, we consider the loop to be a straight magnetic flux tube with radius $R(z)$ (including the annulus layer) and length L. The temperature of the loop is assumed to decay exponentially through time (similarly to, for example, Aschwanden and Terradas 2008, Morton and Erdélyi 2010, Ruderman et al. 2017, Ruderman et al. 2019) following:

$$T(t) = T_0 \exp(-t/t_{cool}), \tag{5.2}$$

where T_0 is the constant external temperature and t_{cool} is the cooling time. We assume similarly to theoretical the works of e.g. Ruderman 2017; Shukhobodskiy et al. 2018; Ruderman et al. 2019 that the cooling time is equal to the total lifetime of the oscillation in each case studied. That means that the cooling stops as soon as the oscillation event ceases to exist.

The variation of the loop cross-section, $R(z)$, is defined by the relation:

$$R(z) = R_f \lambda \sqrt{\frac{\cosh(L/2l_c) - 1}{\cosh(L/2l_c) - \lambda^2 + (\lambda^2 - 1)\cosh(z/l_c)}}, \tag{5.3}$$

where z is the height of the tube (set to be equal to 0 at the apex), R_f is the radius of the magnetic flux tube at the foot-point, $\lambda = R(0)/R_f$ is the expansion factor of the loop, and l_c is an arbitrary constant. This radius profile was also considered by Ruderman et al. (2008, 2017) and Nelson et al. (2019). The density is set to transition from the internal value to the external value in the annulus layer. We follow Goossens et al. (2002) and Shukhobodskiy and Ruderman (2018) and assume that density in the annulus region where resonant absorption can occur, ρ_t, can be modelled linearly as:

$$\rho_t = \frac{\rho_i + \rho_e}{2} + (\rho_i - \rho_e)\frac{R - r}{lR}, \tag{5.4}$$

where ρ_i is internal density, ρ_e is external density, r is the radial coordinate, where $r = 0$ at the center of the magnetic flux tube, and l is a dimensionless parameter, such that $lR(z)$ is the thickness of the transitional layer.

With the aid of Eqs. (5.2) – (5.4), Shukhobodskiy et al. (2018) derived the relation for the dimensionless amplitude, $A(t)$, where $A(0) = 1$, of the kink mode under the

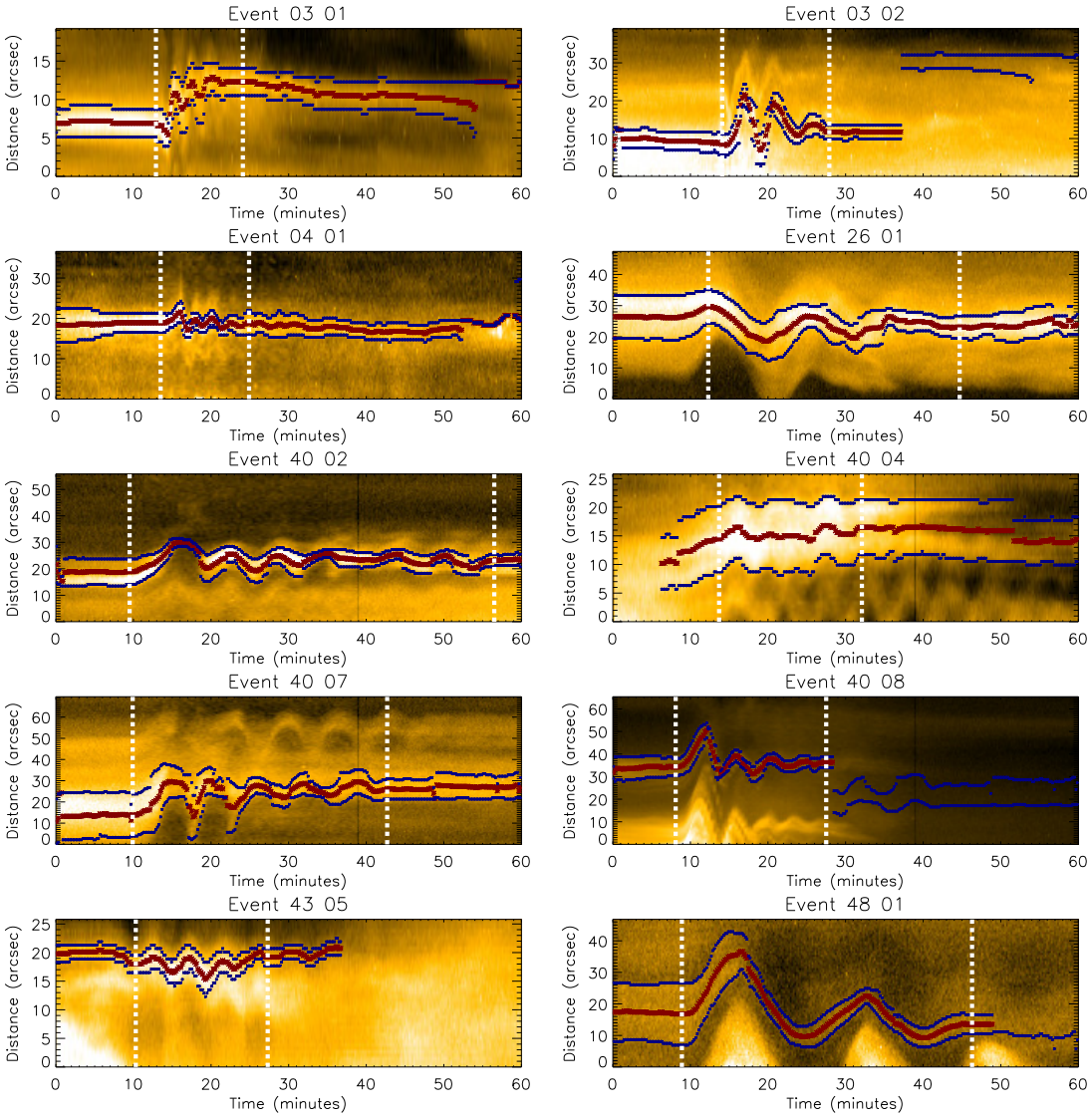

Figure 5.1: Time-space diagrams for each of the selected events studied here. Data was sampled by the SDO/AIA. The x-axis of each panel corresponds to one hour. The y-axes are all different in lengths but are scaled independently to improve the visibility of the oscillations. Exact timing and distance information is provided in Tab. 5.1. The results of the Canny edge-detection algorithm are over-laid as blue crosses. The central position between these points, assumed to be the centre of the loop axis through time, is signified by the red crosses. The vertical white dashed lines denote the time-period plotted in Fig. 5.2. We note that Event 40 04 could correspond to two individual loops over-lying each other, however, we do not remove it as the complex amplitude profile allows us to show-case both the strengths and limitations of the method.

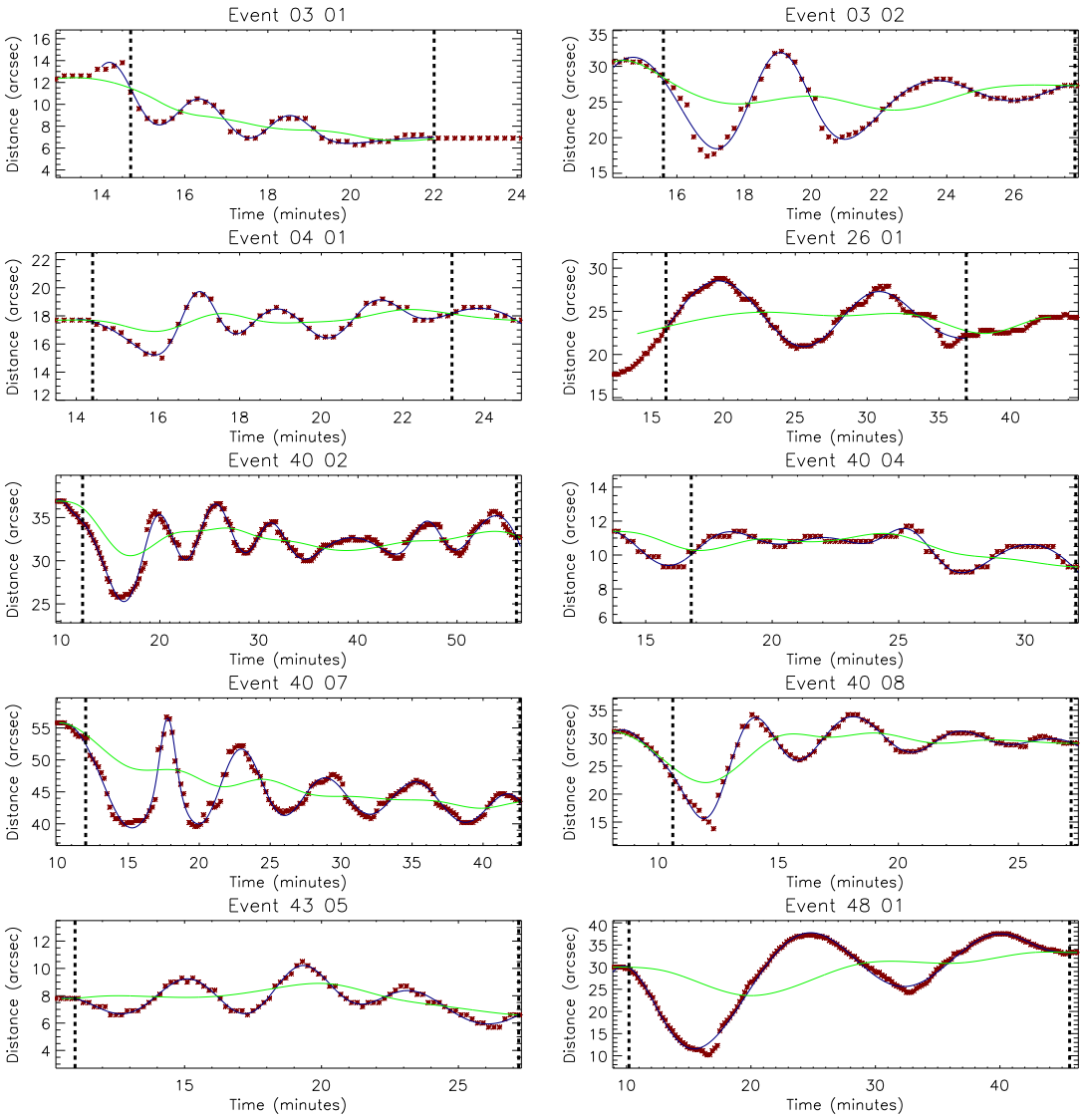

Figure 5.2: Displacement profile of each coronal loop studied in this chapter. The red points correspond to the red points over-laid on Fig. 5.1 and track the measured amplitudes of the oscillation. The green lines display the background trend estimated using spline fitting. The blue lines are the results of fitting Eq. (5.1) to each oscillation. Note the ability of this method to deal with variable periodicities, best seen in Events 40 02 and 40 07. The dashed black vertical lines on each panel outline the time-period plotted in Fig. 5.3 and correspond to oscillation lifetime.

thin tube and thin boundary approximation. In addition to λ, below are the most important parameters in the model:

$$\zeta = \frac{\rho_i(\pm\frac{L}{2})}{\rho_e(\pm\frac{L}{2})}, \quad \kappa = \frac{L}{\pi H_0} \quad \text{and} \quad \alpha = \frac{\pi l C_f t_{cool}}{4L}, \tag{5.5}$$

where H_0 is the scale height in the exterior plasma and C_f is the kink speed at the foot-points of the loop. The parameter ζ corresponds to the ratio between the internal and external densities at the loop foot-points, κ corresponds to the ratio between the coronal loop length and the plasma scale height in the region outside the loop, and, finally, α represents the relative strength between damping due to resonant absorption and amplification due to cooling. In the case where $\alpha = 0$ there is no damping. Furthermore, the ratio of densities at any point of the loop is defined by equations (71) – (73) derived by Shukhobodskiy et al. (2018).

We note that to obtain results for comparison with observed amplitude profiles, the arbitrary constant, l_c should be carefully selected such that the expansion factor be in line with observed values ($1 < \lambda < 1.5$; Klimchuk 2000; Watko and Klimchuk 2000). Here, we set $L/l_c = 6$ (similarly to Ruderman et al. 2008, Shukhobodskiy et al. 2018 and Nelson et al. 2019) to achieve this aim. We also set $A_t = A(0)A_{Ob}(0)$, where A_{Ob} is the initial amplitude measured of the observed oscillation and A_t is the scaling factor for the dimensionless amplitude. This would enable us to compare analytical and theoretical results within comparable scale.

5.2.2 Results of the Model Fitting

In order to fit these observations with the model, we first need to obtain the damping profiles for each of the 10 events studied here. In Fig. 5.2, we plot each of the oscillations identified in Fig. 5.1 with red dots. Each of these oscillations appears to be qualitatively different with different periods and amplitudes, with some having large amplitudes and some only appearing to have small amplitudes (only several pixels). This variety in the studied oscillations allows us to test the model in a more dynamic way than if all oscillations displayed similar behaviour. With this in mind, we keep the fitting of Event 40 04 despite the apparent overlap between two independent loops in the slit and label this as a 'low-confidence' [LC] event in the remainder of this chapter. The green and blue lines in Fig. 5.2 mark the spline fits (following the method of Pascoe et al. 2016c) and the results of applying Eq. 5.1, respectively, for each of the events. The dashed black vertical lines indicate the temporal regions of interest within which the oscillations were studied in the remainder of this chapter. The next step in our analysis was to remove the effects of the background trends and normalise the amplitudes such that the damping profiles could be calculated. The results of this procedure are plotted in Fig. 5.3. It is immediately evident that the damping profiles of Events 03 01, 04 01, 40 02, 40 04 (LC), 40 07, 40 08 and 43 05 clearly deviate from both typical exponential and Gaussian damping. Some of these events display an increase in the amplitude through time whilst some others have stagnation periods where the amplitude remains

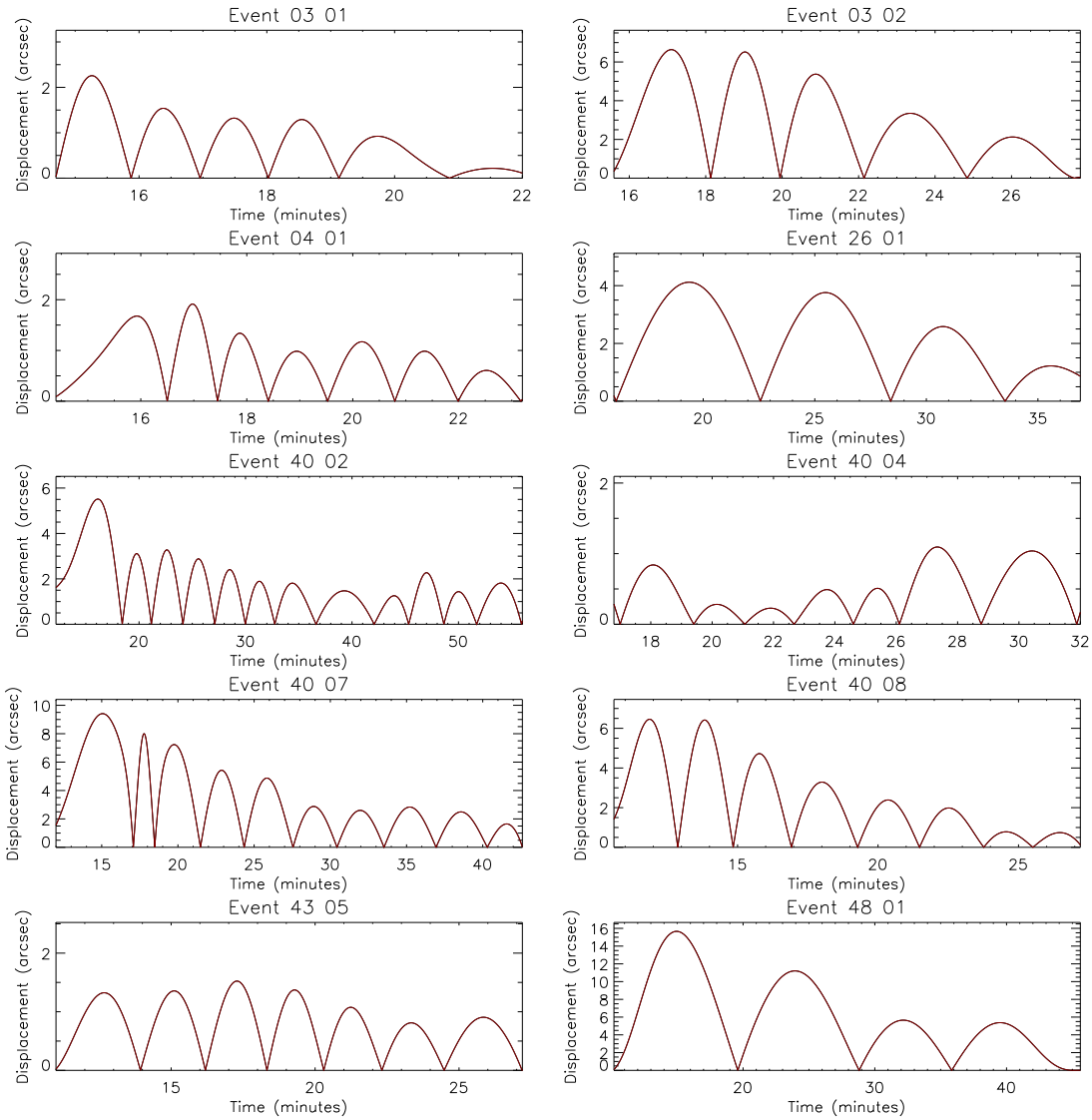

Figure 5.3: The absolute value of the displacement of the Gaussian fitted position profiles (blue line from Fig. 5.2) from the spline fitted background trend (green line from Fig. 5.2) through time for each of the events studied here.

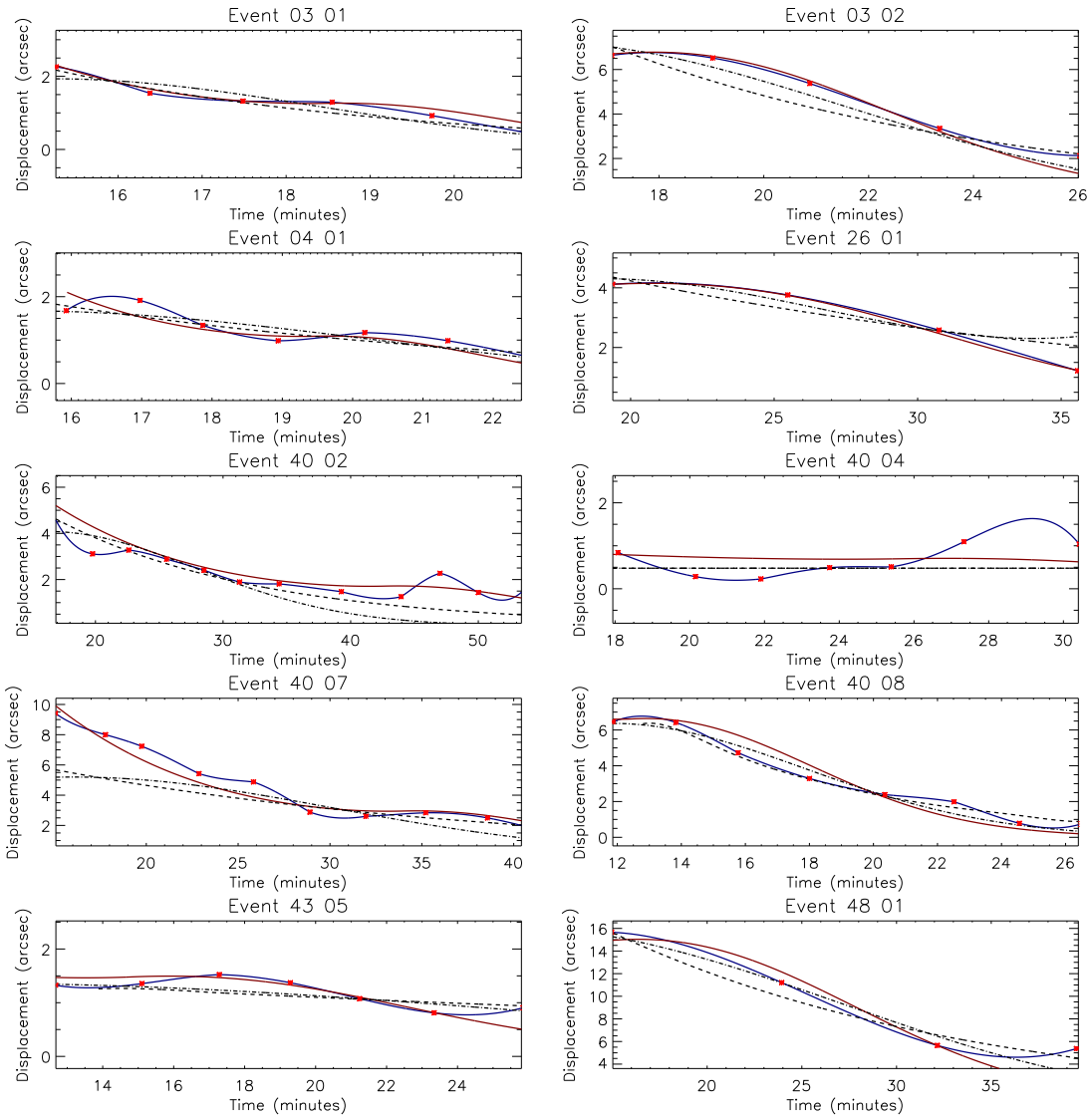

Figure 5.4: The fitting of the model, introduced by Shukhobodskiy et al. (2018), to the coronal loop oscillations studied here. The blue lines plot spline fits through the maxima of each peak plotted in Fig. 5.3. The red lines plot the approximation of the oscillations obtained through fitting the theoretical model. Reasonable fits are achieved for all events except Event 40 04 (LC). The dot-dashed lines represents Gaussian fit and the dashed lines correspond to exponential fits. Finally, the red crosses indicate the peaks from Fig. 5.3.

constant for a while before further amplitude reduction takes place. Such damping profiles are difficult to explain using standard methods.

Next, we applied the model proposed by Shukhobodskiy et al. (2018) to the damping profiles, varying the four parameters discussed in the previous section to minimise the

departure from the measured amplitude profile (as was previously done by Nelson et al. 2019). In Fig. 5.4 we plot the amplitudes of each peak of each oscillation as red dots, with spline fits over-laid as blue lines. The optimised results of the model fitting are over-laid as red lines. In order to compare with other single models, we also plot fits calculated using both exponential (dashed) and Gaussian (dot-dashed) profiles, as discussed in Pascoe et al. (2016c), which study the damping of a fundamental mode. The parameters used for the cooling model provide sufficiently good fits in a qualitative sense in the majority of cases, as can be seen in Fig. 5.4, with only Event 40 04 (LC) being visually poorly fitted. Essentially, including the effects of cooling in the fitting of kink-mode damping profiles can produce good fits for a wide variety of profiles but even this method can struggle when low amplitude, highly variable damping profiles are considered. Deviations from standard Gaussian or exponential damping profiles are most prominent in Events 03 01, 03 02, 04 01, 26 01, 40 07 and 43 05 where several saddle points are evident in the fits. It is worth noting that this model is also capable of capturing features of both the Gaussian and exponential damping profiles by varying its parameters, with near-Gaussian damping profiles being returned for Events 40 08 and 48 01 and near-exponential damping being returned for Event 40 02. We note that Gaussian damping profiles can only be obtained for low values of ζ (< 1.2) whereas exponential damping profiles can only be obtained with values of ζ higher than 4.5 when values of κ, λ, and α are not extreme. For values of α closer to 0, the effect of damping due to resonant absorption would be completely cancelled out by the amplification due to cooling with overall amplification present. On the other hand, high values of α would result in profiles very similar to exponential decay, due to strong damping accountable for resonant absorption and weak cooling, though small increases in amplitude would be still present. The specific value of α that would make this change is dependent on the loop itself. Lowering the loop length by making κ smaller will compensate the increase in α. Furthermore, higher loop expansion favours amplification, therefore, to reduce the damping profile to an exponential profile one would need to consider values of $\zeta > 7$.

Highly complex amplitude profiles, for example Event 43 05, display both decreases and increases in the amplitude through time. Fortunately, this complexity can be explained by theory once cooling is considered. For lower values of ζ less than 1.2 the theoretical profile reduces to Gaussian decay. Whereas, for higher values of density ratios, the initial part would start with exponential decrease first and then after some time the local increase may appear after which the Gaussian decay profile appears. This behaviour provides higher degrees of freedom in fitting the observations meaning more amplitude profiles are now theoretically permitted. This fact makes it ultimately both convenient and useful to consider the evolution of temperature during oscillations for accurate approximation of seismological parameters. Goddard and Nakariakov (2016) discussed the importance of the projection angle in order to obtain more accurate information about coronal loops, which could cause a cascade of associated errors and require the need to perform multiple angle analysis of the same phenomena. Despite this fact, the model used in this chapter is not dependent on the absolute values of the damping profile, rather it depends on the normalised shape of oscillation, making it

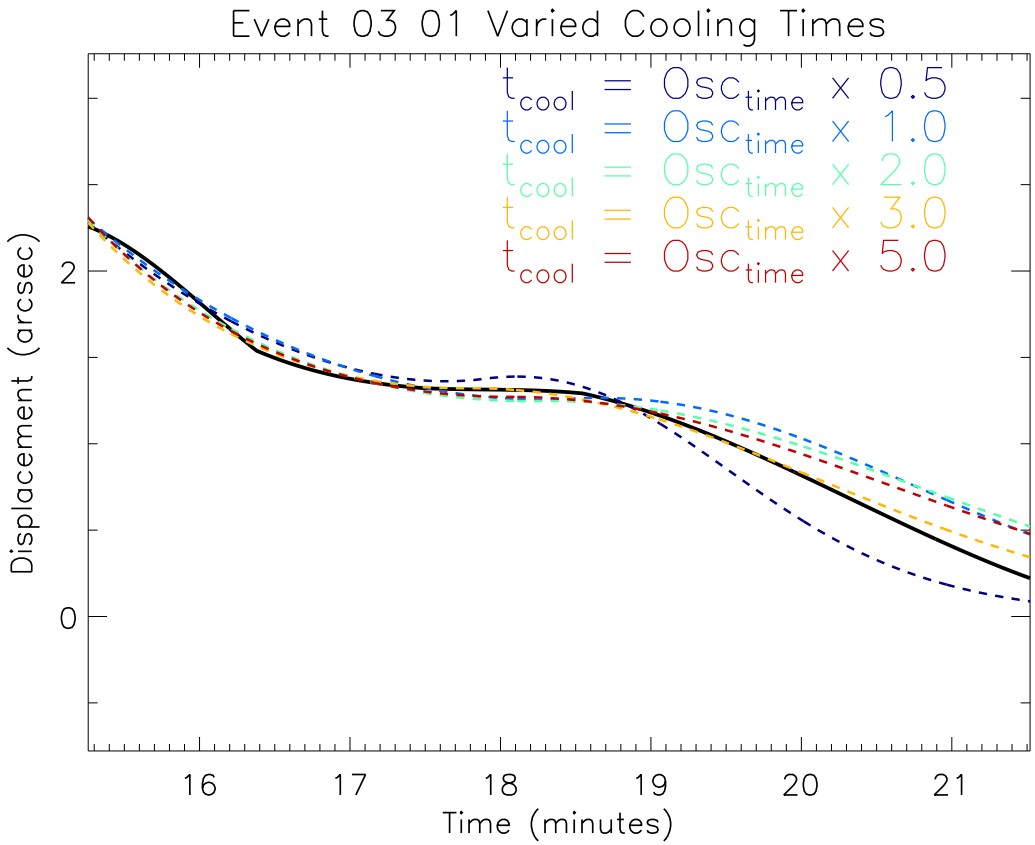

Figure 5.5: Examination of the effect of cooling time on the fits of the analytical model to observations. The κ values for each of the cooling times (from quickest to slowest) are $1.3, 2.9, 5.6, 5.7, 10.9$, respectively, and the corresponding ζ values are $3.7, 3, 1.7, 1.35, 1.2$. We should note the condition of applicability of Shukhobodskiy et al. (2018) is $t_{cool} \gg P/6$, where t_{cool} is the cooling time and P is oscillation period.

resistant to the above errors in obtaining the dimensionless parameters. As such, that could lead to faster analysis of kink oscillations of coronal loops. However, such an error does limit the estimation of parameters with dimensions in the model used here.

We should note that ζ is responsive to the position where the analytical solution changes it shape (e.g., where amplitude increases are detected). Any increases in the assumed cooling time results in a stretching of the analytical solution and lowers the value of ζ, however, such effects becomes slower or negligible as ζ becomes closer to 1 as seen in Figure 5.5. Additionally, increases in the cooling time lead to increases of κ in order to fit the observed shape. Nevertheless, in all occasions the model is able to capture the observed profile for various lengths of cooling. Essentially, this introduces some degeneracy in our solutions which will need to be further studied through future research. Moreover, oscillations with low values of ζ are barely affected by the cooling

Event	03 01	03 02	04 01	26 01	40 02	40 04	40 07	40 08	43 05	48 01
ζ	3	1.03	2.6	1.01	4	3	4.5	1.1	1.35	1.01
λ	1.01	1.21	1.01	1.05	1.1	1.05	1.01	1.05	1.3	1.05
κ	2.9	2.6	2	1.7	1.6	1.8	2.5	3.5	2.2	2.95
α	1	0.9	1.6	1	1.6	0.5	1.1	1.1	1.01	0.8

Table 5.2: Best-fit parameters fitted by the theoretical model for each of the loop oscillations studied here. Note that ζ is rather sensitive to the selection of the starting time of the oscillation and we assume that the cooling time is equal to oscillation time. Whilst conducting the fits, virtually any values of $\zeta \pm 0.2$, $\lambda \pm 0.05$, $\kappa \pm 0.2 \pm \epsilon_\kappa$, $\alpha \pm 0.1 \pm \epsilon_\alpha$, where ϵ with subscript denotes the errors associated with variation of ζ provided sufficiently good approximations to the observed values, however, the above particular values were chosen to follow the measured damping trend better. Given that there might be an error in the estimation of the starting time of damping, one should pay extra care of determining ζ in the vicinity of $\zeta = 1$, due to the ratio of internal and external densities being susceptible to changes in this interval. The combination of λ, κ, and α are key for the speed of decay of the amplitude. In this study, these values were treated as parameters and further measurements should be made to accurately determine κ and α in the future. We note that Event 40 02 was studied previously by Nelson et al. (2019), however, here we analysed a longer time-period, therefore, explaining the difference in ζ.

time, where kink oscillations with high values of ζ could lead to overestimation of this parameter and require additional measurements to determine t_{cool} or κ. Once t_{cool} or κ is known or measured the model provides quick and accurate estimate for ζ. Furthermore, in the case where values of ζ are in the range 1–1.7 existing estimates of damping profiles are sufficiently good even without knowing t_{cool} and κ. We should note that the theoretical model studied here explains deviations from typical exponential or Gaussian damping profiles due to cooling, which causes plasma flows towards footpoints of the coronal loop. As a result, the upper parts of the coronal loops become lighter, however the impulse is preserved. The lighter the loop with comparison to surroundings the less effect will be visible by cooling. That could be seen that for values of $\zeta < 1.2$ the damping profile is almost Gaussian. Furthermore the effect on heavier loops with $\zeta > 7$ is the similar, since the cooling time is not sufficient to affect the initial impulse of the oscillation. As a result, an exponential damping profile is preserved. Despite that, the introduction of cooling to the system might still provide better approximation for oscillations, however, at this time it is difficult to test this observationally. Furthermore, the most interesting analysis occurs for values of $1.2 \leq \zeta \leq 7$, where cooling plays a significant role in determining oscillation profiles. It is in this density range that future analyses could be focused.

Event	χ_t^2	χ_g^2	χ_e^2	$\tilde{\chi}_t^2$	$\tilde{\chi}_g^2$	$\tilde{\chi}_e^2$
03 01	0.5692	0.6857	0.4702	3.8990	5.6609	4.1022
03 02	0.5312	1.1218	1.3095	7.7526	26.8841	26.8841
04 01	0.4909	0.2764	0.2810	5.4039	7.3583	5.3894
26 01	0.0086	0.0446	0.1781	0.9976	38.5140	33.9762
40 02	1.5567	9.7141	7.0435	110.7415	646.3610	242.6087
40 04	3.6473	2.7641	2.7642	150.7310	99.0152	99.0189
40 07	1.0192	9.4239	7.9315	50.3733	314.3506	292.3057
40 08	2.2148	0.9184	0.6627	68.0517	25.3550	28.0358
43 05	0.3280	0.2262	0.3118	4.6998	8.6158	12.9752
48 01	3.9506	2.5507	1.1667	168.46012	61.3025	89.8005

Event 03 01	χ_t^2	$\tilde{\chi}_t^2$
Cooling time is equal to Oscillation time × 0.5	0.2277	4.8311
Cooling time is equal to Oscillation time × 2.0	0.7294	3.0602
Cooling time is equal to Oscillation time × 2.5	0.1197	0.2886
Cooling time is equal to Oscillation time × 3.0	0.1180	0.2628
Cooling time is equal to Oscillation time × 3.5	0.1958	0.4912
Cooling time is equal to Oscillation time × 4.0	0.2545	0.7012
Cooling time is equal to Oscillation time × 5.0	0.5357	1.8411

Table 5.3: Comparative analysis for goodness of fit from the observed data for the theoretical model presented by Shukhobodskiy et al. (2018) and for Gaussian and exponential fits presented by Pascoe et al. (2016c). χ_t^2, χ_g^2 and χ_e^2, correspond to χ^2 goodness of fit calculations for the cooling, Gaussian, and exponential models, respectively, only by comparing extremum points (i.e. peaks of the amplitudes). $\tilde{\chi}_t^2$, $\tilde{\chi}_g^2$ and $\tilde{\chi}_e^2$, correspond to $\tilde{\chi}^2$ goodness of fit for the cooling, Gaussian, and exponential models comparing overall fit at all times during the damping. The top panel exhibit the analysis for all studied events with cooling time been equal to oscillation time and bottom panel corresponds to the event 03 01 for various cooling times.

The inferred, best fit, parameters (defined in the previous section) for each of the oscillations are presented in Tab. 5.2. To obtain accurate approximations for ζ, care should be taken in accurately positioning the dashed black lines in Fig. 5.2 due to its high sensitivity to temporal variations. In Fig. 5.6, we plot the relationship between the density ratio at the loop foot-points, ζ, and the oscillation amplitudes (left panel) and periods (right panel) as measured by Goddard et al. (2016). It is immediately evident that the higher amplitude and longer period oscillations appear to have lower density ratios between the loop and the external environment at the foot-points. Although we are hesitant to draw strong conclusions about this due to the small statistical size and lack of direct density diagnostics, this result does suggest further research should be done to investigate such links in the future. Some important steps forward could come through analysing the ratios between the O_{IV} lines sampled by the Interface Region Imaging Spectrograph (IRIS; De Pontieu et al. 2014) at the foot-points of oscillating

loops. Some limitations of this model are evident in Fig. 5.4 where deviations between the fitted theoretical model and the measured observed values are evident. It is unclear at this stage whether these limitations are caused by differences in the observed and modelled structures or due to measurement errors. It should be noted that the recent work of Goddard et al. (2017) shows that some of the loops might not have thin boundaries, with Pascoe et al. (2019) discussing the possible limitations of the thin boundary approximation used within theoretical approach. This could possibly lead to underestimation of ζ, with the current model supporting $l \leq 0.5$. However, the effect of the transitional layer changes have not yet being studied in this configuration for cooling loops to provide accurate estimates of possible errors for kink oscillations of cooling coronal loops with $l \geq 0.5$. Future observational and analytical work will be needed to better understand this. We also note that since the analytical model is very sensitive in a non-linear way to the position of local oscillation amplification, without significant improvement in image resolution, it would be impossible to obtain the estimate of an error of given ζ and consequently all other parameters. Thus an upper bound of general error estimates for fixed values of ζ are applied here. However, once the spatial resolution of obtained data increases and the shape observed oscillation is more certain, quantification of these errors will be paramount for correct estimates.

Table 5.3 provides the comparison with previous models, we could see that inclusion of cooling to Events 03 02, 26 01, 40 02, 40 07 with oscillation time been equal to the oscillation time could lead the cooling theoretical model to have better approximations to the damping profiles than exponential and Gaussian fits, in case only extremum points (i.e. amplitude maxima) are taken as the point of reference. If instead we analyse the overall damping profile (i.e. calculate the χ^2 values at all time-steps), then Events 03 01, 03 02, 04 01, 26 01, 40 02, 40 07, 43 05 are approximated better by the cooling model, rather than exponential or Gaussian fits. We should note that the goodness of fit could be further improved in the cooling model if we were to put more stress on deviation from the observed data instead of focusing on finding the turning points. However, we should mention that position of turning point is crucial for estimation for values of ζ. Furthermore, changing the ratio between oscillation time and cooling time could improve significantly the goodness of fit as was described in Event 03 01.

§ 5.3 Summary

In this chapter, we have further demonstrated the promise of the theory developed by Shukhobodskiy et al. (2018) by applying it to 10 kink-mode oscillations. These events were sampled by the SDO/AIA instrument and were randomly selected from the population identified to have complex damping profiles in the statistical study of Goddard et al. (2016). Space-time diagrams were constructed for each oscillation before the edges of the loops through time were determined by employing the Canny edged-detection method (see Fig. 5.1). The mid-point between the edges was defined as the central axis of the oscillating loop for each time-step. The background trends were then subtracted from each oscillation using spline fitting before the detrended data

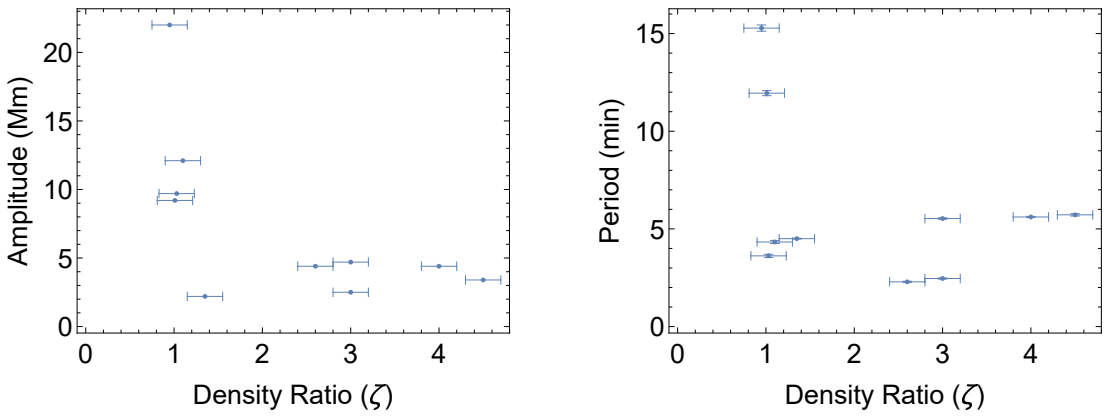

Figure 5.6: Scatter plots displaying the apparent relationships between the amplitude and period of the coronal loop oscillations (as measured by Goddard et al. 2016) and the density ratio inferred here.

were then fitted with a series of Gaussian functions. The results of the application of these steps to the oscillations can be seen in Fig. 5.2.

Next, we plotted the absolute values of the amplitude variation of the kink-mode oscillations through time in Fig. 5.3. Some oscillations displayed clear deviations from the usual Gaussian or exponential damping profiles even at this stage. Specifically, five (Events 04 01, 40 02, 40 04 (LC), 40 07, and 43 05) of the 10 oscillations studied here displayed evidence of increases in amplitude through time. Such amplification was shown to be possible during oscillations of cooling loops by Ruderman (2011b), Shukhobodskiy and Ruderman (2018) and has been reported before in observations by Nelson et al. (2019). Using an iterative approach, we then constructed best fits for the parameters defined in Eq. 5.5 such that the difference between the observed and theoretical damping profiles was minimised. In Fig. 5.4 it was shown that this theoretical model provides qualitatively reasonable approximations for the damping of kink oscillations of coronal loops for nine of the 10 cases (all except Event 40 04 [LC]). This result indicates that cooling should be studied in more detail in future research. Additionally, we have also shown that the model is capable of capturing the properties of fitting both simple Gaussian and exponential profiles, depending on the ratio of external and internal densities, ζ, at the loop foot-points. Furthermore, for sufficiently large loops with $\kappa \geq 1.6$, the shape of the damping profile is determined by this ratio. In the case where cooling is present, for the small values of ζ the profile would be Gaussian, while for large values of ζ it would be exponential. All values in-between would be a combination of both.

Chapter 6

Flute oscillations of cooling coronal loops with variable cross-section

§ 6.1 Model Proposed

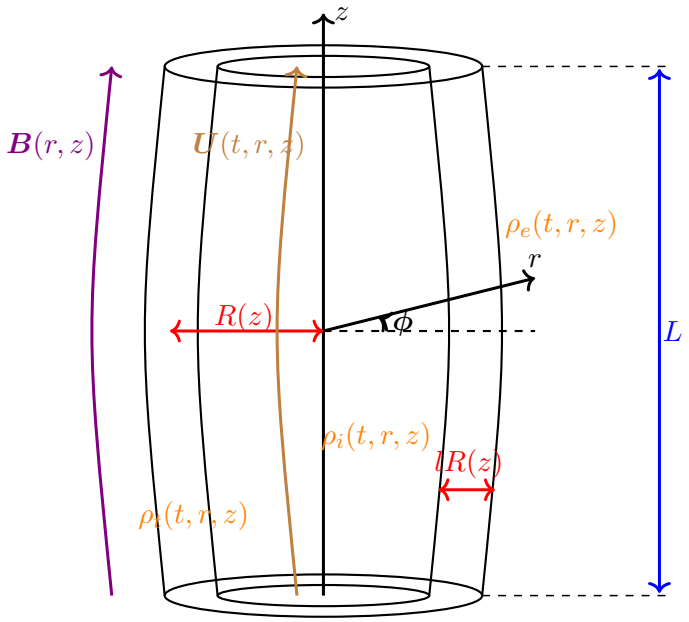

Figure 6.1: Sketch of the equilibrium configuration of magnetic flux tube with transitional layer in the presence of a background flow.

In this chapter, we continue to investigate the model of an axisymmetric coronal loop, that was defined in Chapter 4, by focusing on the propagation of fluting modes. The

unperturbed equilibrium configuration is given in Fig. 6.1. Similar as before, we introduce cylindrical coordinates r, ϕ, z. The density inside the tube $\rho_i(t,r,z)$ varies with time along and across the magnetic flux tube as well as the density in the surrounding plasma $\rho_e(t,r,z)$ and in the transitional layer $\rho_t(t,r,z)$ are considered and are given by

$$\rho = \begin{cases} \rho_i(t,r,z), & 0 \le r \le R(z)(1-l/2), \\ \rho_t(t,r,z), & R(z)(1-l/2) \le r \le R(z)(1+l/2), \\ \rho_e(t,r,z), & r \ge R(z)(1+l/2). \end{cases} \tag{6.1}$$

Here, l is a constant determining the thickness of the transitional layer sandwiched between the loops's interior and exterior. It is assumed that $\rho(t,r,z)$ is a continuous function, and $\rho_t(t,r,z)$ is a monotonically decreasing function of r. The reason why the tube is split into core and transitional layer is because we want to take into account damping due to resonance absorption. The time-independent non-twisted equilibrium magnetic field is $\boldsymbol{B} = (B_r(r,z), 0, B_z(r,z))$. Therefore the divergence-free condition $\nabla \cdot \boldsymbol{B} = 0$ for the magnetic field may be written as

$$\frac{1}{r}\frac{\partial (rB_r)}{\partial r} + \frac{\partial B_z}{\partial z} = 0. \tag{6.2}$$

It follows from this equation that we can write $\boldsymbol{B}$ as

$$B_r = -\frac{1}{r}\frac{\partial \psi}{\partial z}, \quad B_z = \frac{1}{r}\frac{\partial \psi}{\partial r}, \tag{6.3}$$

where ψ is a magnetic flux function. We also consider that boundaries of the transitional layers to be magnetic surfaces. As a result, we can write equations $\psi = \psi_i = \text{const}$ instead of $r = R(z)(1-l/2)$ and $r = R(z)(1+l/2)$, respectively. Here, and in what follows, indices i and e refer to internal and external values of quantities and parameters. Now, here and below, the cold plasma approximation and thin tube thin boundary TTTB approximation are applied. Thus, with the aid of equilibrium configuration we deduct that the magnetic field is potential. That means that, $\nabla \times \boldsymbol{B} = 0$, that we transform in polar coordinate as follows

$$\frac{\partial B_r}{\partial z} = \frac{\partial B_z}{\partial r}. \tag{6.4}$$

We substitute Equation (6.3) into Equation (6.4), that allows us to rewrite Equation (6.4) in terms of ψ to yield

$$r\frac{\partial}{\partial r}\left(\frac{1}{r}\frac{\partial \psi}{\partial r}\right) + \frac{\partial^2 \psi}{\partial z^2} = 0. \tag{6.5}$$

Moreover, in this model, the background flow $\boldsymbol{U} = (U_r(t,r,z), 0, U_z(t,r,z))$ also exists and depends on time. We also assume that the time-dependent background flow is field aligned, meaning that it is parallel to the equilibrium magnetic field. As a result, we

have, $\boldsymbol{U} \parallel \boldsymbol{B}$. The relation between plasma density and velocity is defined by the mass conservation equation:

$$\frac{\partial \rho}{\partial t} + \frac{1}{r}\frac{\partial (r\rho U_r)}{\partial r} + \frac{\partial (\rho U_z)}{\partial z} = 0. \tag{6.6}$$

We define the perturbations of the magnetic field $\boldsymbol{b} = (b_r, b_\phi, b_z)$ and of the plasma velocity $\boldsymbol{u} = (u_r, u_\phi, u_z)$. Then, we express these perturbations in terms of linearised MHD equation in the cold plasma approximation as

$$\frac{\partial \boldsymbol{u}}{\partial t} + (\boldsymbol{U}\cdot\nabla)\boldsymbol{u} + (\boldsymbol{u}\cdot\nabla)\boldsymbol{U} = \frac{1}{\mu_0\rho}(\nabla\times\boldsymbol{b})\times\boldsymbol{B}, \tag{6.7}$$

$$\frac{\partial \boldsymbol{b}}{\partial t} = \nabla\times(\boldsymbol{u}\times\boldsymbol{B} + \boldsymbol{U}\times\boldsymbol{b}), \tag{6.8}$$

$$\nabla\cdot\boldsymbol{b} = 0, \tag{6.9}$$

where μ_0 is the magnetic permeability of free space.

§ 6.2 Derivation of governing equation

As initial step, in order to be able to apply derivations of Ruderman et al. (2017) introduce the plasma displacement $\boldsymbol{\xi} = \boldsymbol{x} - \boldsymbol{x_0}$, where $\boldsymbol{x}(t, \boldsymbol{a})$ is the trajectory of the particle and $\boldsymbol{a}$ is the initial position. Components of displacement and components of the displacement and velocity are given by,

$$\xi_\perp = \xi_r b_{0z} - \xi_z b_{0r} \quad u_\perp = u_r b_{0z} - u_z b_{0r}. \tag{6.10}$$

The longitudinal component of background magnetic field is considered to be positive, thus $B_z > 0$. The magnetic flux tube is thin, as a result to approximate ψ it is enough to take first terms of Taylor's expansion. Furthermore, the tube axis is assumed to be the magnetic field line $\psi = \text{const}$ at $r = 0$. Thus, without loss of generality $\psi = 0$ at $r = 0$ could be considered, as a result with the aid of Equation (6.3) we have

$$\psi = \frac{1}{2}r^2 h(z). \tag{6.11}$$

Ruderman et al. (2017) showed that:

$$h(z)R^2(z) = C = \text{const}. \tag{6.12}$$

Here, $h(z)$ is arbitrary function of z that satisfies MHD equations. It is easy to see that the derivation of Ruderman et al. (2017) by means of multiple scale analysis is still valid up to Equation (57) therein under the thin tube thin boundary approximation. That means that we have thin magnetic tube and thus $R(z)/L = \mathcal{O}(\epsilon)$. Here, $\epsilon \ll 1$ is a small number and all quantities vary with characteristic scale of L. Furthermore, stretched variables are used, thus $Z = \epsilon z$ is introduced. That means that the characteristic time of the problem is L/V_*, where V_* is characteristic Alfvén speed. The Alfénic time with respect to the tube radius is defined by R_*/V_*, where R_* is the characteristic radius

of the magnetic flux tube. Therefore, the ratio of the both problem time and Alfénic time is of the order ϵ^{-1} . That allows us to introduced the stretched time $T = \epsilon t$. As a result, we use Equations (53)–(57) of Ruderman et al. (2017) described below

$$P = -\frac{1}{\mu_0}\left(rB^2\frac{\partial w}{\partial \psi} + \frac{B^2}{r}\frac{\partial \xi_\phi}{\partial \phi} - \epsilon^2\tilde{B}_r\frac{\partial w}{\partial Z} + B_z\frac{w}{r}\right), \tag{6.13}$$

$$u_\perp = \frac{\epsilon}{B}\frac{\partial w}{\partial T} + \frac{\epsilon U_z}{rB}\frac{\partial (rw)}{\partial Z}, \tag{6.14}$$

$$u_\phi = \epsilon\frac{\partial \xi_\phi}{\partial T} + \epsilon r U_z\frac{\partial}{\partial Z}\left(\frac{\xi_\phi}{r}\right), \tag{6.15}$$

$$\epsilon\frac{u_\perp}{T} + \epsilon r U B_z\overline{Z}\left(\frac{u_\perp}{rB}\right) = \frac{rBB_z}{\mu_0\rho}\frac{\partial}{\partial Z}\left(\frac{B_z}{r^2B^2}\frac{\partial (rw)}{\partial Z}\right) + \frac{B^2}{\rho}\left[\epsilon^2\tilde{b}_{0r}\frac{\partial}{\partial Z}\left(\frac{P}{B^2}\right) - rB\frac{\partial}{\partial \psi}\left(\frac{P}{B^2}\right)\right], \tag{6.16}$$

$$\epsilon\frac{\partial u_\phi}{\partial T} + \epsilon\frac{U_z}{r}\frac{\partial (ru_\phi)}{\partial Z} = \frac{\epsilon^2 B_z}{\mu_0\rho r}\frac{\partial}{\partial Z}\left[r^2B_z\frac{\partial}{\partial Z}\left(\frac{\epsilon_\phi}{r}\right)\right] - \frac{1}{\rho r}\frac{\partial P}{\partial \phi} \tag{6.17}$$

and take perturbations proportional to $e^{i\tilde{m}\phi}$, where $\tilde{m}$ is the azimuthal wavenumber, $u_\perp = \epsilon\tilde{u}_\perp$ and $u_\phi = \epsilon\tilde{u}_\phi$, to obtain:

$$\mathcal{O}(\epsilon^2) = rB^2\frac{\partial w}{\partial \psi} + \frac{i\tilde{m}B^2\xi_\phi}{r} + B_z\frac{w}{r}, \tag{6.18}$$

$$\tilde{u}_\perp = \frac{1}{B}\frac{\partial w}{\partial T} + \frac{U_z}{rB}\frac{\partial rw}{\partial Z}, \tag{6.19}$$

$$\tilde{u}_\phi = \frac{\partial \xi_\phi}{\partial T} + rU_z\frac{\partial}{\partial Z}\left(\frac{\xi_\phi}{r}\right), \tag{6.20}$$

$$\frac{\partial \tilde{u}_\perp}{\partial T} + rUB_z\frac{\partial}{\partial Z}\left(\frac{\tilde{u}_\perp}{rB}\right) = \frac{rBB_z}{\mu_o\rho}\frac{\partial}{\partial Z}\left(\frac{B_z}{r^2B^2}\frac{\partial rw}{\partial Z}\right) - \frac{rB^3}{\rho}\frac{\partial Q}{\partial \psi} + \mathcal{O}(\epsilon^2), \tag{6.21}$$

$$\frac{\partial \tilde{u}_\phi}{\partial T} + \frac{U_z}{r}\frac{\partial r\tilde{u}_\phi}{\partial Z} = \frac{B_z}{\mu_0\rho r}\frac{\partial}{\partial Z}\left[r^2B_z\frac{\partial}{\partial Z}\left(\frac{\xi_\phi}{r}\right)\right] - \frac{i\tilde{m}B^2Q}{\rho r}. \tag{6.22}$$

Then, we retain only the leading terms with respect to ϵ, and remove ξ_ϕ, $\tilde{u}_\perp$ and $\tilde{u}_\phi$ from the system of equation. Thus, we rewrite equations for Q and w as:

$$Q = \frac{1}{\mu_0\tilde{m}^2B}\frac{\partial}{\partial Z}\left(r^2B\frac{\partial^2 W}{\partial \psi \partial Z}\right) - \frac{\rho}{\tilde{m}^2B^2}\left(r^2\frac{\partial}{\partial T} + U\frac{\partial}{\partial Z}r^2\right)\left(\frac{\partial^2 W}{\partial T\partial \psi} + U\frac{\partial^2 W}{\partial \psi \partial Z}\right), \tag{6.23}$$

$$\left(\frac{\partial}{\partial T}+r^2UB^2\frac{\partial}{\partial Z}\frac{1}{r^2B^2}\right)\left(\frac{\partial W}{\partial T}+U\frac{\partial W}{\partial Z}\right)$$
$$=\frac{r^2B^3}{\mu_0\rho}\frac{\partial}{\partial Z}\left(\frac{1}{r^2B}\frac{\partial W}{\partial Z}\right)-\frac{r^2B^4}{\rho}\frac{\partial Q}{\partial\psi}, \tag{6.24}$$

where $W = rw = Br\xi_\perp$. Then, as quantities ρ, B and U could be treated as independent of r they could also be considered as quantities independent on ψ. Furthermore, with the aid of Equation (6.11), we transform Q as:

$$Q=\frac{2\psi}{\tilde{m}^2h}\frac{\partial}{\partial\psi}\left[\frac{1}{\mu_0}\frac{\partial^2W}{\partial Z^2}-\frac{\rho}{h^2}\left(\frac{\partial}{\partial T}+hU\frac{\partial}{\partial Z}\frac{1}{h}\right)\left(\frac{\partial W}{\partial T}+U\frac{\partial W}{\partial Z}\right)\right], \tag{6.25}$$

$$\left(\frac{\partial}{\partial T}+hU\frac{\partial}{\partial Z}\frac{1}{h}\right)\left(\frac{\partial W}{\partial T}+U\frac{\partial W}{\partial Z}\right)=\frac{h^2}{\mu_0\rho}\frac{\partial^2W}{\partial Z^2}-\frac{2\psi h^3}{\rho}\frac{\partial Q}{\partial\psi}. \tag{6.26}$$

Now, we differentiate Equation (6.26) with respect to ψ and apply Equation (6.25) on the result, to yield:

$$4\psi\frac{\partial}{\partial\psi}\left(\psi\frac{\partial Q}{\partial\psi}\right)-\tilde{m}^2Q=0. \tag{6.27}$$

In order to satisfy, the boundary conditions for the proposed model solutions to Equation (6.27) must be regular at ψ= 0 and decay as $\psi\to\infty$. Thus, we have

$$Q=\begin{cases}Q_i(T,Z)\psi^{\tilde{m}/2}, & 0\le\psi\le\psi_i,\\ Q_e(T,Z)\psi^{-\tilde{m}/2}, & \psi\ge\psi_e,\end{cases}, \tag{6.28}$$

where Q_i and Q_e are arbitrary functions. Equations $\psi=\psi_i$ and $\psi=\psi_e$, where ψ_i and ψ_e are constants, are defining the external and internal boundaries respectively. Then, with the aid of Equations (6.11) and (6.12) we obtain the following

$$\psi_i=\frac{C}{2}\left(1-\frac{l}{2}\right)^2,\quad \psi_e=\frac{C}{2}\left(1+\frac{l}{2}\right)^2. \tag{6.29}$$

Employing (6.26) and (6.28) yields that $W=\psi^{\tilde{m}/2}\widetilde{W}(T,Z)$ in the core region of the modelled magnetic flux tube, where $\widetilde{W}(T,Z)$ is an arbitrary function. With the aid of Equation (6.28) we transform Equation (6.26) to

$$\left(\frac{\partial}{\partial T}+hU_i\frac{\partial}{\partial Z}\frac{1}{h}\right)\left(\frac{\partial W_i}{\partial T}+U_i\frac{\partial W_i}{\partial Z}\right)-\frac{h^2}{\mu_0\rho_i}\frac{\partial^2W_i}{\partial Z^2}=-\frac{\tilde{m}\psi_i^{\tilde{m}/2}h^3Q_i}{\rho_i}, \tag{6.30}$$

$$\left(\frac{\partial}{\partial T}+hU_e\frac{\partial}{\partial Z}\frac{1}{h}\right)\left(\frac{\partial W_e}{\partial T}+U_e\frac{\partial W_e}{\partial Z}\right)-\frac{h^2}{\mu_0\rho_e}\frac{\partial^2W_e}{\partial Z^2}=\frac{\tilde{m}h^3Q_e}{\rho_e\psi_e^{\tilde{m}/2}}, \tag{6.31}$$

where W_i and W_e are calculated at $\psi=\psi_i$ and $\psi=\psi_e$, respectively. We now suggest the new variable

$$\eta=\frac{1}{R(z)}\xi_\perp. \tag{6.32}$$

We note that, in the case $\tilde{m} = 1$, $\xi_\perp$ is independent of r. In that case we can conclude that the magnetic flux tube oscillate as solid. In addition, Equations (6.30) and (6.31) reduce to ones obtained by Ruderman et al. (2017). Following Ruderman et al. (2017), we introduce jumps of η and the magnetic pressure perturbation across the transitional region,

$$\delta\eta = \eta\big|_{\psi=\psi_e} - \eta\big|_{\psi=\psi_i}, \quad \delta P = P\big|_{\psi=\psi_e} - P\big|_{\psi=\psi_i}. \tag{6.33}$$

We can estimate $\delta\eta$ as $\delta\eta = \mathcal{O}(l)$ and δP as $\delta P = \mathcal{O}(l)$. As a result, with the aid of Equation (6.28), we have

$$\begin{gathered} W_i = C(1 - l/2)\eta, \quad W_e = C[(1 + l/2)\eta + \delta\eta], \\ \psi_i^{\tilde{m}/2} h^3 Q_i = \frac{\epsilon^{-2} C}{R^2} P\big|_{\psi=\psi_i}, \quad \psi_e^{-\tilde{m}/2} h^3 Q_e = \frac{\epsilon^{-2} C}{R^2} P\big|_{\psi=\psi_e}. \end{gathered} \tag{6.34}$$

We multiply Equation (6.30) by ρ_i and Equation (6.31) by ρ_e, add the results, employing Equations (6.12), (6.33) and (6.34), and transforming the system to the initial non-scaled independent variables, yields

$$\begin{aligned} &\rho_i \left(\frac{\partial}{\partial t} + \frac{U_i}{R^2} \frac{\partial}{\partial z} R^2 \right) \left(\frac{\partial \eta}{\partial t} + U_i \frac{\partial \eta}{\partial z} \right) \\ &+ \rho_e \left(\frac{\partial}{\partial t} + \frac{U_e}{R^2} \frac{\partial}{\partial z} R^2 \right) \left(\frac{\partial \eta}{\partial t} + U_e \frac{\partial \eta}{\partial z} \right) - \frac{2B^2}{\mu_0} \frac{\partial^2 \eta}{\partial z^2} = \mathcal{L}, \end{aligned} \tag{6.35}$$

with

$$\begin{aligned} \mathcal{L} = &\frac{\tilde{m} \delta P}{R^2} + \frac{B^2}{\mu_0} \frac{\partial^2 \delta\eta}{\partial z^2} \\ &- \rho_e \left(\frac{\partial}{\partial t} + \frac{U_e}{R^2} \frac{\partial}{\partial z} R^2 \right) \left(\frac{\partial}{\partial t} + U_e \frac{\partial}{\partial z} \right) \left(\frac{l\eta}{2} + \delta\eta \right) \\ &+ \rho_i \left(\frac{\partial}{\partial t} + \frac{U_i}{R^2} \frac{\partial}{\partial z} R^2 \right) \left(\frac{\partial}{\partial t} + U_i \frac{\partial}{\partial z} \right) \frac{l\eta}{2}. \end{aligned} \tag{6.36}$$

For $0 \leq \psi \leq \psi_i$ we have

$$\begin{aligned} &\left(\frac{\partial}{\partial t} + \frac{U_i}{R^2} \frac{\partial}{\partial z} R^2 \right) \left(\frac{\partial \eta}{\partial t} + U_i \frac{\partial \eta}{\partial z} \right) - \frac{B^2}{\mu_0 \rho_i} \frac{\partial^2 \eta}{\partial z^2} = \\ &\left(\frac{\hat{r}}{1 - l/2} \right)^{\tilde{m}-1} \left(\left(\frac{\partial}{\partial t} + \frac{U_i}{R^2} \frac{\partial}{\partial z} R^2 \right) \left(\frac{\partial \eta_i}{\partial t} + U_i \frac{\partial \eta_i}{\partial z} \right) - \frac{B^2}{\mu_0 \rho_i} \frac{\partial^2 \eta_i}{\partial z^2} \right), \end{aligned} \tag{6.37}$$

while for $\psi \geq \psi_e$ we have

$$\left(\frac{\partial}{\partial t}+\frac{U_e}{R^2}\frac{\partial}{\partial z}R^2\right)\left(\frac{\partial \eta}{\partial t}+U_e\frac{\partial \eta}{\partial z}\right)-\frac{B^2}{\mu_0\rho_e}\frac{\partial^2\eta}{\partial z^2}=$$
$$\left(\frac{1+l/2}{\hat{r}}\right)^{\tilde{m}-1}\left(\left(\frac{\partial}{\partial t}+\frac{U_e}{R^2}\frac{\partial}{\partial z}R^2\right)\left(\frac{\partial \eta_e}{\partial t}+U_e\frac{\partial \eta_e}{\partial z}\right)-\frac{B^2}{\mu_0\rho_e}\frac{\partial^2\eta_e}{\partial z^2}\right), \tag{6.38}$$

$$\xi_\phi=\frac{ir}{\tilde{m}}\frac{\partial rw}{\partial \psi}, \tag{6.39}$$

where $\hat{r}=r/R(z)=(\psi/\psi_i)^{1/2}$, $\eta_i=\eta(\psi_i)$ and $\eta_e=\eta(\psi_e)$. Whenever $\tilde{m}>0$ and in the absence of the transitional layer i.e. $l=0$, the oscillations of the double-layered magnetic flux tube studied in this chapter, are governed by Equations (6.35) – (6.38). This result is applicable both for standing waves and propagating waves. Whenever, $l\neq 0$, the system of governing equation is not closed. To close it the jumps across the transitional layer $\delta\eta$ and δP should be obtained. Furthermore, in case $\tilde{m}=1$, Equation (6.37) is fulfilled identically, since η is independent of the r-coordinate. As a result, the above system of governing equation reduces identically to the governing system obtained by Ruderman et al. (2017), with a detailed investigation done by Shukhobodskiy and Ruderman (2018), Shukhobodskiy et al. (2018), Ruderman et al. (2019) and Ruderman and Petrukhin (2019).

6.2.1 Fluting Modes in the Absence of Transitional Layer

In this section, we assume that the transitional layer is absent so that the magnetic flux tube has sharp boundaries. In this case, we have $l=0$. As a result of such assumption for the equilibrium configuration of our model, Equation (6.35), with the right-hand side equal to 0 governs oscillation of the modelled magnetic flux tube. Thus, we transform Equation (6.35) to

$$\rho_i\left(\frac{\partial}{\partial t}+\frac{U_i}{R^2}\frac{\partial}{\partial z}R^2\right)\left(\frac{\partial \eta}{\partial t}+U_i\frac{\partial \eta}{\partial z}\right)+$$
$$\rho_e\left(\frac{\partial}{\partial t}+\frac{U_e}{R^2}\frac{\partial}{\partial z}R^2\right)\left(\frac{\partial \eta}{\partial t}+U_e\frac{\partial \eta}{\partial z}\right)-\frac{2B^2}{\mu_0}\frac{\partial^2\eta}{\partial z^2}=0. \tag{6.40}$$

Using Equation (6.37) we reduce it to

$$\left(\frac{\partial}{\partial t}+\frac{U}{R^2}\frac{\partial}{\partial z}R^2\right)\left(\frac{\partial \eta}{\partial t}+U\frac{\partial \eta}{\partial z}\right)-\frac{B^2}{\mu_0\rho}\frac{\partial^2\eta}{\partial z^2}=$$
$$=\hat{r}^{\tilde{m}-1}\left(\left(\frac{\partial}{\partial t}+\frac{U_i}{R^2}\frac{\partial}{\partial z}R^2\right)\left(\frac{\partial \eta_i}{\partial t}+U_i\frac{\partial \eta_i}{\partial z}\right)-\frac{B^2}{\mu_0\rho_i}\frac{\partial^2\eta_i}{\partial z^2}\right) \tag{6.41}$$

§ 6.3 Eigenvalue problem in the presence of stationary flow: General analysis

Here, we consider that the density and the flow velocity are both independent of time. Furthermore we assume that the external plasma is at rest, i.e $U_e = 0$. As we consider that the characteristic scale of variation of the equilibrium quantities in the radial direction is the same as in the axial direction, it is possible to ignore theirs radial variation inside the magnetic flux tube under TTTB approximation. Therefore, employing mass conservation Equation (6.6) yields that the relationship between the density and the flow speed is given by

$$\rho_i U R^2 = \text{const}, \tag{6.42}$$

where the subscript 'i' for the flow speed U in the internal region was discarded.

$$BR^2 = \text{const}. \tag{6.43}$$

We assume that both tube ends are fixed in much denser photosphere. Furthermore, we restrict our analysis to standing waves only. This allows us to introduce the following boundary conditions

$$\eta = 0 \quad \text{at} \quad z = \pm L/2, \tag{6.44}$$

where L is the tube length. In what follows, we seek for stationary solutions, hence we take $\eta \propto e^{-i\omega t}$. Thus, we reduce Equation (6.41) to

$$\left(\frac{B^2}{\mu_0} - \rho_i U_i^2\right)\left(\frac{\partial^2 \eta}{\partial z^2} - \hat{r}^{\tilde{m}-1}\frac{\partial^2 \eta_i}{\partial z^2}\right) + \left(2i\omega\rho_i U_i - \frac{\rho_i U_i}{R^2}\frac{\partial U_i R^2}{\partial z}\right) \times \left(\frac{\partial \eta}{\partial z} - \hat{r}^{\tilde{m}-1}\frac{\partial \eta_i}{\partial z}\right) + \left(\frac{2i\omega\rho_i U_i}{R}\frac{\partial R}{\partial z} + \omega^2\rho_i\right)\left(\eta - \hat{r}^{\tilde{m}-1}\eta_i\right) = 0 \tag{6.45}$$

Equations (6.44) and Equation (6.45), establish an eigenvalue problem. Below, we investigate the general properties of the described problem. The main point of interest in this section is to seek the conditions for which the magnetic flux tube would be stable with respect to long flute perturbations. As a result, we consider that for all $z \in [-L/2, L/2]$ $\mu_0\rho_i U^2 < B^2$, that is $U^2 < V_{Ai}^2 \equiv B^2/\mu_0\rho_i$. Thus we propose the following variable substitution

$$\eta - \hat{r}^{\tilde{m}-1}\eta_i = q\exp(-i\omega\sigma(z)), \quad \sigma = \int_{-L/2}^{z} \frac{\mu_0\rho_i U\, dz'}{B^2 - \mu_0\rho_i U^2}. \tag{6.46}$$

Now, with the aid of substitutions described by Equation (6.46), we act on Equation (6.45) Moreover, we multiply the obtained equation by R^4. As a result, we transform Equation (6.45) as

$$\frac{d}{dz}\left[R^4\left(\frac{B^2}{\mu_0} - \rho_i U^2\right)\frac{dq}{dz}\right] + \omega^2 W(z) q = 0, \tag{6.47}$$

where

$$W(z) = \frac{R^4\rho_i B^2}{B^2 - \mu_0\rho_i U^2}. \tag{6.48}$$

The classical Sturm-Liouville problem with the eigenvalue ω^2 can be constructed by means of Equation (6.47) and the boundary condition Equation (6.47). General theory of the Sturm-Liouville problem (e.g. Coddington and Levinson, 1955) imposes that the eigenvalues are real and constitute a monotonically increasing unbounded sequence. In accordance to the Sturm-Lioiville theory the first eigenvalue is the square of the fundamental frequency. Furthermore, eigenfunction that relates to the fundamental frequency has no nodes in $(-L/2, L/2)$. Moreover, all the remaining eigenvalues are the squares of frequencies of overtones that correlates to frequencies. The relations between eigenfunction of nth overtone to the nodes is n to $n-1$ respectively for all z in $(-L/2, L/2)$.

Eigenfunctions of the Sturm-Liouville problem can be always taken to be real, therefore we can always take q to be real . We multiply Equation (6.47) by q. Then, we integrate the obtained equation with the respect to z. The resulting expression Equation (6.48), yields

$$\omega^2 \int_{-L/2}^{L/2} W(z) q^2 \, dz = \int_{-L/2}^{L/2} R^4 \left(\frac{B^2}{\mu_0} - \rho_i U^2 \right) \left(\frac{dq}{dz} \right)^2 dz. \tag{6.49}$$

Due to $W(z) > 0$ and with the aid of Equation (6.49), we obtain that $\omega^2 > 0$. Thus, all the eigenfrequencies are real. As as result, the sufficient condition for stability inside the magnetic flux tube with respect to long flute perturbations is defined by following inequality $U^2 < V_{Ai}^2$. Moreover, the magnetic flux tube is outside of stable equilibrium, whenever $\omega^2 < 0$. To obtain an equation describing the boundary, we follow the analysis of Ruderman et al. (2017) to find out that the stability condition is different, with a sufficient condition $U^2 < 2V_{Ai}^2$. Moreover, we highlight that such condition is sufficient for the stability of the system, but not necessary. Furthermore, the presented analysis does not prove that the magnetic flux tube is stable even if the condition $U^2 < V_{Ai}^2$ is satisfied. Nevertheless, it insures that for long flute perturbations the magnetic flux tube is stable. For other types of perturbation the system might be unstable.

§ 6.4 Flute oscillations of magnetic flux tube with slowly varying density

In what follows, we assume that we have oscillations of a magnetic flux tube with slowly varying density with tube ends fixed on much denser photosphere. As a result,the boundary condition Equation (6.45) is fulfilled. Below, we assume that the characteristic time of density variation, t_{ch}, is much greater than the characteristic time of oscillations. Such assumptions does not impose significant restrictions on the model.

6.4.1 Derivation of adiabatic invariant

We consider the small value $\nu \ll 1$. This value is defined though the ratio of t_{ch} to the characteristic time of oscillations ν^{-1}. Then, νt_{ch} is the characteristic time of oscillations. Moreover, the characteristic time of oscillations is still of the order of the

loop length divided by the characteristic kink speed, $L/(B/\sqrt{\mu_0\rho_{ch}})$, where ρ_{ch} is the characteristic density. Therefore, we obtain

$$B \sim \nu^{-1}\sqrt{\mu_0\rho_{ch}}\frac{L}{t_{ch}}. \tag{6.50}$$

With the aid of estimate Equation (6.50), we consider the scaled magnetic field $\widetilde{B} = \nu B$. Thus, we transform Equations (6.38) and (6.47) as

$$\left(\frac{\nu^{-2}\widetilde{B}^2}{\mu_0} - \rho_i U_i^2\right)\left(\frac{\partial^2\eta}{\partial z^2} - \hat{r}^{\tilde{m}-1}\frac{\partial^2\eta_i}{\partial z^2}\right) + \left(2i\omega\rho_i U_i - \frac{\rho_i U_i}{R^2}\frac{\partial U_i R^2}{\partial z}\right)\times$$
$$\left(\frac{\partial\eta}{\partial z} - \hat{r}^{\tilde{m}-1}\frac{\partial\eta_i}{\partial z}\right) + \left(\frac{2i\omega\rho_i U_i}{R}\frac{\partial R}{\partial z} + \omega^2\rho_i\right)\left(\eta - \hat{r}^{\tilde{m}-1}\eta_i\right) = 0, \tag{6.51}$$

$$\left(\frac{\nu^{-2}\widetilde{B}^2}{\mu_0} - \rho_e U_e^2\right)\left(\frac{\partial^2\eta}{\partial z^2} - \hat{r}^{1-\tilde{m}}\frac{\partial^2\eta_e}{\partial z^2}\right) +$$
$$+\left(2i\omega\rho_e U_e - \frac{\rho_e U_e}{R^2}\frac{\partial U_e R^2}{\partial z}\right)\left(\frac{\partial\eta}{\partial z} - \hat{r}^{1-\tilde{m}}\frac{\partial\eta_i}{\partial z}\right) +$$
$$+\left(\frac{2i\omega\rho_e U_e}{R}\frac{\partial R}{\partial z} + \omega^2\rho_e\right)\left(\eta - \hat{r}^{1-\tilde{m}}\eta_e\right) = 0 \tag{6.52}$$

We now implement the Wentzel-Kramer-Brillouin (WKB) method (e.g. Bender and Orszag, 1978) and seek for solutions to the transformed governing equation defined by following relation

$$\eta = S(t, r, z)\exp[i\nu^{-1}\Theta(t)]. \tag{6.53}$$

Afterwards, S is expanded in the series

$$S = S_0 + \nu S_1 + \ldots \tag{6.54}$$

Substituting Equation (6.53) in Equations (6.51) and (6.52), employing Equation (6.54) and collecting terms of order ν^{-2}, yields

$$\frac{\partial^2\widetilde{S}_0}{\partial z^2} + \frac{\Omega^2}{\widetilde{V}_{Ai}^2}\widetilde{S}_0 = 0 \tag{6.55}$$

and

$$\frac{\partial^2\hat{S}_0}{\partial z^2} + \frac{\Omega^2}{\widetilde{V}_{Ae}^2}\hat{S}_0 = 0 \tag{6.56}$$

where

$$\widetilde{S}_0 = S_0(t, r, z) - \hat{r}^{\tilde{m}-1}S_0(t, R(z), z),$$
$$\hat{S}_0 = S_0(t, r, z) - \hat{r}^{1-\tilde{m}}S_0(t, R(z), z),$$
$$\Omega = \frac{d\Theta}{dt}, \quad \widetilde{V}_{Ai}^2 = \frac{\widetilde{B}^2}{\mu_0\rho_i} \quad \widetilde{V}_{Ae}^2 = \frac{\widetilde{B}^2}{\mu_0\rho_e}. \tag{6.57}$$

Now, we note that in interior of the expanding magnetic flux tube $\hat{r}^{\tilde{m}-1} << 1$. Furthermore in the exterior of the magnetic flux tube $\hat{r}^{1-\tilde{m}} << 1$. Thus, we add Equations (6.55) and (6.56), to have

$$\frac{\partial^2 S_0}{\partial z^2} + \frac{\Omega^2}{\tilde{C}_k^2} S_0 = 0, \tag{6.58}$$

where

$$\tilde{C}_k^2 = \frac{2\tilde{B}^2}{\mu_0(\rho_i + \rho_e)} \tag{6.59}$$

As the ends of magnetic flux tube are fixed to the dense photosphere, then

$$S_0 = 0 \quad \text{at} \quad z = \pm L/2. \tag{6.60}$$

Now, the classical Sturm-Liouville problem is established by Equations (6.58) and (6.60). This zero order approximation is also known as approximation of geometrical optics (e.g. Bender and Orszag, 1978). More interesting, the Sturm-Liouville problem Equations (6.58) and (6.60) coincide with a problem obtained by Dymova and Ruderman (2005), where non-expanding magnetic flux tube with density stratification was studied. Furthermore, the boundary value problem agrees, with expanding magnetic flux tube model with longitudinal density stratification investigated by Ruderman et al. (2008). Moreover, this result coincides with the work of Ruderman et al. (2017), where expanding magnetic flux tube with density stratification in the presence of background flow was studied. In what follows, we suppose that Ω^2 is an eigenvalue that corresponds to eigenfunction S_0 the corresponding eigenfunction. With the aid of generatl Sturm-Liouville theory (e.g. Coddington and Levinson, 1955), Ω^2 is real. It is possible to prove that $\Omega^2 > 0$. To do so we multiply equation (6.58) by S_0. Afterwards, we integrate the obtained equation by parts parts with respect to z from $-L/2$ to $L/2$. Then, we impose the boundary condition (6.60). Due to the nature of Sturm-Liouville problem, it is always possible to consider that S_0 is a real function.

Collecting terms of the order ν^{-1}, we obtain

$$\frac{\partial^2 \tilde{S}_1}{\partial z^2} + \frac{\Omega^2}{\widetilde{V}_{Ai}^2}\tilde{S}_1 = \frac{2i\Omega}{\widetilde{V}_{Ai}^2}\left(\frac{\partial \tilde{S}_0}{\partial t} + \frac{\tilde{S}_0}{2\Omega}\frac{\partial \Omega}{\partial t} + \frac{U_i}{R}\frac{\partial R\tilde{S}_0}{\partial z}\right) \tag{6.61}$$

and

$$\frac{\partial^2 \hat{S}_1}{\partial z^2} + \frac{\Omega^2}{\widetilde{V}_{Ae}^2}\tilde{S}_1 = \frac{2i\Omega}{\widetilde{V}_{Ae}^2}\left(\frac{\partial \hat{S}_0}{\partial t} + \frac{\hat{S}_0}{2\Omega}\frac{\partial \Omega}{\partial t} + \frac{U_e}{R}\frac{\partial R\hat{S}_0}{\partial z}\right), \tag{6.62}$$

where

$$\widetilde{S}_1 = S_1(t, r, z) - \hat{r}^{\tilde{m}-1} S_1(t, R(z), z) \tag{6.63}$$

and

$$\hat{S}_1 = S_1(t, r, z) - \hat{r}^{1-\tilde{m}} S_1(t, R(z), z). \tag{6.64}$$

Taking account that inside the magnetic flux tube $\hat{r}^{\tilde{m}-1} << 1$, outside the flux tube $\hat{r}^{1-\tilde{m}} << 1$ and on the boundary $\hat{r}^{\tilde{m}-1}$ and $\hat{r}^{1-\tilde{m}}$ are of the order of unity, from Equations (6.61) and (6.62), we have

$$\frac{\partial^2 S_1}{\partial z^2} + \frac{\Omega^2}{\tilde{C}_k^2} S_1 = \frac{2i\Omega}{\tilde{C}_k^2}\left(\frac{\partial S_0}{\partial t} + \frac{S_0}{2\Omega}\frac{\partial \Omega}{\partial t} + \frac{U_e}{R}\frac{\partial R S_0}{\partial z}\right), \tag{6.65}$$

This first order approximation is known as the approximation of the physical optics. Here, S_1 has to meet the boundary condition

$$S_1 = 0 \quad z = \pm L/2. \tag{6.66}$$

The homogeneous counterparts of Equations (6.58), (6.65), (6.60), and (6.66) construct boundary value has non-trivial solution $S_1 = S_0$. Therefore, the boundary value problem that determines S_1 has solution only if the right-hand side of Equation (6.65) satisfies the compatibility condition. This compatibility condition that the solution must be be orthogonal to S_0 respectively. In order to recover the compatibility condition we multiply Equation (6.65) by S_0, afterwards we integrate the obtained equation with respect to z from $-L/2$ to $L/2$. As a result, after some algebra we obtain

$$\int_{-L/2}^{L/2} \frac{1}{C_k^2}\frac{\partial \Omega S_0^2}{\partial t} dz = -\frac{\Omega}{2}\int_{-L/2}^{L/2} \frac{U_i}{R^2 C_k^2}\frac{\partial (S_0^2 R^2)}{\partial z} dz. \tag{6.67}$$

Now, we use integration by parts, and then some algebra, we ultimately obtain

$$\omega \int_{-L/2}^{L/2} \frac{S_0^2}{C_k^2} dz = \text{const}, \tag{6.68}$$

where

$$\omega = \nu^{-1}\Omega, \quad C_k = \frac{2B^2}{\mu_0(\rho_i + \rho_e)}. \tag{6.69}$$

The adiabatic invariant is defined by the left-hand side of Equation (6.68). Considering the full Equation (6.68) we can see that adiabatic invariant is conserved. We can follow analysis presented by Ruderman et al. (2017) to see that results for derivation for adiabatic invariant and approximations of 0 order for the boundary value problem still holds to be true. Furthermore, the obtained adiabatic invariant is the equivalent to that received by Ruderman (2011a) for oscillations of non-expanding magnetic flux tubes. As a result, the expansion of the magnetic flux tube does only affect the time evolution of flute oscillations of magnetic flux tubes with the varying density through $R(z)$ dependent C_k,V_{Ai}, V_{Ae}, S_0.

6.4.2 Effect of cooling on flute oscillations of coronal magnetic loops

The major reason of heat loss in a coronal loop is due to radiation. Furthermore, we know that in an optically thin plasma the intensity is proportional to the plasma density

squared. Therefore, as the internal region of a magnetic flux tube is much denser than the rarefied external plasma the energy deposition that has potential to cover energy losses in external region might not be significant enough to cover loss of energy in the magnetic flux tube interior. As a consequence, we consider the exterior region to have constant temperature. Following assumptions of Aschwanden and Nightingale (2005) and Morton and Erdélyi (2010), we approximate the evolution of temperature in the internal region of the loop by exponentially decaying function,

$$T(t) = T_0 \exp(-t/t_{cool}). \tag{6.70}$$

Here, we assume cooling starts at initial time, $t = 0$. Moreover, that the temperature of plasma both in internal and external is the same at the initial time. Thus the plasma temperature in external plasma is T_0. Now, we assume that the shape of the expanding magnetic flux tube is half-circle. This allows us to neglect the effect of the magnetic flux tube curvature on flute oscillations on everything but density variation along the loop. As a result, barometric formula is determining density variation in the external plasma (see e.g. Ruderman, 2017; Shukhobodskiy et al., 2018)

$$\rho_e(z) = \frac{\rho_f}{\zeta} \exp\left(\frac{-L}{\pi H_0} \cos\frac{\pi z}{L}\right) \tag{6.71}$$

and

$$H_0 = \frac{k_B T_0}{mg}, \tag{6.72}$$

where ρ_f is the plasma density at the footpoints inside the magnetic flux tube, ζ is the ratio of internal and external plasma densities at initial time, k_B is the Boltzmann constant, g is the gravity acceleration, and m is the mean mass per particle equal to one half of the proton mass for a proton-electron plasma. Furthermore, we assume that the plasma density at foopoints in internal region of the magnetic flux tube is constant. Plasma cooling is generating plasma flow within the magnetic flux tube. Since all equations are changed by power only the results of Ruderman (2011c) analysis could be easily generalised for the fluting modes described in the model proposed to show that the result is still valid. As a result, for typical coronal conditions density variation is weakly affected by plasma flow for the observed cooling times. Thus, we can approximate plasma density variation in the internal layer of the expanding magnetic flux tube by barometric formula, to obtain

$$\rho_i(z) = \rho_f \exp\left(\frac{-L}{\pi H(t)} \cos\frac{\pi z}{L}\right), \tag{6.73}$$

where

$$H(t) = \frac{k_B T(t)}{mg}. \tag{6.74}$$

The variation of cross-section radius of the tube can be defined by the same expression as in Ruderman et al. (2008), as the background magnetic field is potential. Thus, we

have

$$R(z) = R_f \lambda \sqrt{\frac{\cosh(L/2l_c) - 1}{\cosh(2L/2l_c) - \lambda^2 + (\lambda^2 - 1)\cosh(z/l_c)}}, \tag{6.75}$$

where $\lambda = R(0)/R_f$, l_c is an arbitrary positive constant and has the dimension of length and R_f is the cross-section radius of the expanding magnetic flux tube at the footpoints. Moreover, Ruderman et al. (2008) concluded that the expansion factor has to be in agreement with the inequality $\lambda < \lambda_m$, where

$$\lambda_m^2 \approx \frac{1.4\cosh(L/2l_c)}{1 + 0.4\cosh(L/2lc)}. \tag{6.76}$$

so that the z-component of the magnetic field stays positive everywhere in the region $|z| \leq L/2$. It follows from Equation (6.76) that λ_m is a monotonically increasing function of L/l_c, such that $\lambda_m \to 1$ as $L/l_c \to 0$, and $\lambda_m \to 1.87$ as $L/l_c \to \infty$. Observed coronal loop expansion factors do not exceed 1.5. Therefore, by varying L/l_c it possible to encompass the whole range of the possible expansion factors. Now, we proceed with the numerical analysis. We start by defining dimensionless variables and parameters required for the analysis:

$$Z = \frac{2z}{L},\ \tau = \frac{t}{t_{cool}},\ \varpi = \frac{\omega L}{C_f},\ \kappa = \frac{L}{\pi H_0},$$
$$\Lambda = \frac{R}{R_F},\ S_0' = \frac{S_0}{R_f}, \tag{6.77}$$

where the kink speed at the footpoints is defined by

$$C_f^2 = \frac{2\zeta B_f^2}{\mu_0 \rho_f (\zeta + 1)}. \tag{6.78}$$

Therefore, we can reduce Equation (6.58) to

$$\frac{\partial^2 S_0}{\partial Z^2} + \frac{\varpi^2 \Lambda^4(Z) S_0}{4(\zeta + 1)} \times [\zeta \exp(-\kappa e^{\tau} \cos(\pi Z/z) + \exp(-\kappa \cos(\pi Z/2)] = 0. \tag{6.79}$$

We have dropped the prime in Equation (6.79). We should also note that in order to obtain solution both for plasma displacement in internal region and for the plasma displacement in external region, which both depend on radial component, we first need find solution for the plasma displacement at the boundary Equation (6.79). We also know that $W = rR(z)B\eta$, knowing that inside the tube $W = \psi^{\tilde{m}/2}\tilde{W}(t,z)$ and in external region in vicinity of the magnetic flux tube $W = \psi^{\tilde{-m}/2}\hat{W}(t,z)$, where $\hat{W}(t,z)$ is arbitrary function we can obtain:

$$\eta = \frac{1}{2}\left(\frac{\psi^{\tilde{m}-1}}{\psi^i}\right)^{\frac{1}{2}} \tilde{W}(t,z) \quad \text{for} \quad 0 \leq r \leq R(z) \quad \text{and}$$
$$\eta = \frac{1}{2}\left(\frac{1}{\psi^{\tilde{m}+1}\psi^i}\right)^{\frac{1}{2}} \tilde{W}(t,z) \quad \text{for} \quad r \geq R(z). \tag{6.80}$$

The eigenfunction S_0 is accurately determined up to the multiplication of arbitrary function of τ, the dependence on ψ is determined by equation (6.80). We can always fix the value of it at one particular point. We assume $X(\tau, Z)$ to be an eigenfunction corresponding to the fundamental mode, which satisfy the condition $X(\tau, 0) = 1$. Then, the general solution to the eigenvalue problem of the fundamental mode is $S_0(\tau, Z, \psi) = A(\tau, \psi)X(\tau, Z)$, where $A(\tau, \psi)$ is the oscillation amplitude at $Z = 0$. With the aid of equation (6.80) we derive:

$$S_0 = \frac{1}{2}\left(\frac{\psi^{m-1}}{\psi_i}\right)^{\frac{1}{2}} \hat{A}(\tau)X(\tau, Z) \quad \text{for} \quad 0 \leq r \leq R(Z) \quad \text{and} \tag{6.81}$$

$$S_0 = \frac{1}{2}\left(\frac{1}{\psi^{m+1}\psi_i}\right)^{\frac{1}{2}} \tilde{A}(\tau)X(\tau, Z) \quad \text{for} \quad r \geq R(Z), \tag{6.82}$$

where

$$A(\tau, \psi) = \frac{1}{2}\left(\frac{\psi^{m-1}}{\psi_i}\right)^{\frac{1}{2}} \hat{A}(\tau) \quad 0 \leq r \leq R(Z) \quad \text{and} \tag{6.83}$$

$$A(\tau, \psi) = \frac{1}{2}\left(\frac{1}{\psi^{m+1}\psi_i}\right)^{\frac{1}{2}} \tilde{A}(\tau) \quad r \geq R(Z). \tag{6.84}$$

Therefore, we rewrite equation (6.68) as

$$\varpi A^2(\tau, \psi) \int_{-1}^{1} X^2 \Lambda^4 [\zeta \exp(-\kappa e^{\tau} cos(\pi Z/2)) + \exp(-\kappa cos(\pi Z/2))] dZ = \text{const}. \tag{6.85}$$

We also note that,

$$\frac{A(\tau, \psi)}{A(0, \psi_i)} = \frac{\hat{A}(\tau)}{\hat{A}(0)}\left(\frac{r}{R(Z)}\right)^{m-1} \quad \text{for} \quad 0 \leq r \leq R(Z) \quad \text{and} \tag{6.86}$$

$$\frac{A(\tau, \psi)}{A(0, \psi_i)} = \frac{\tilde{A}(\tau)}{\tilde{A}(0)}\left(\frac{R(Z)}{r}\right)^{m+1} \quad \text{for} \quad r \geq R(Z). \tag{6.87}$$

Then, we set $l_c = 4$ so that all the observed range of possible λ is covered by expansion model and solve equations (6.85) – (6.87) numerically to obtain the dependence of dimensionless amplitude on r for various values of $\tilde{m}$. First, we note that it follows from Figure 6.2 that the higher the value of λ is the lower is the amplitude closer to the magnetic flux tube core. The phenomena that can be spotted is that the amplitude increase between initial and final time. Furthermore, the higher the expansion factor is the higher the final amplitude, which is similar to the result obtained by Shukhobodskiy et al. (2018). The other pattern that we can notice in Figure 6.2 is that the higher the value of $\tilde{m}$ is the more the oscillations are localised to the tube boundary. The latest statement is in agreement with Soler (2017). Furthermore, we note that the expansion factor λ of magnetic flux tube is paramount in determining the oscillation intensity.

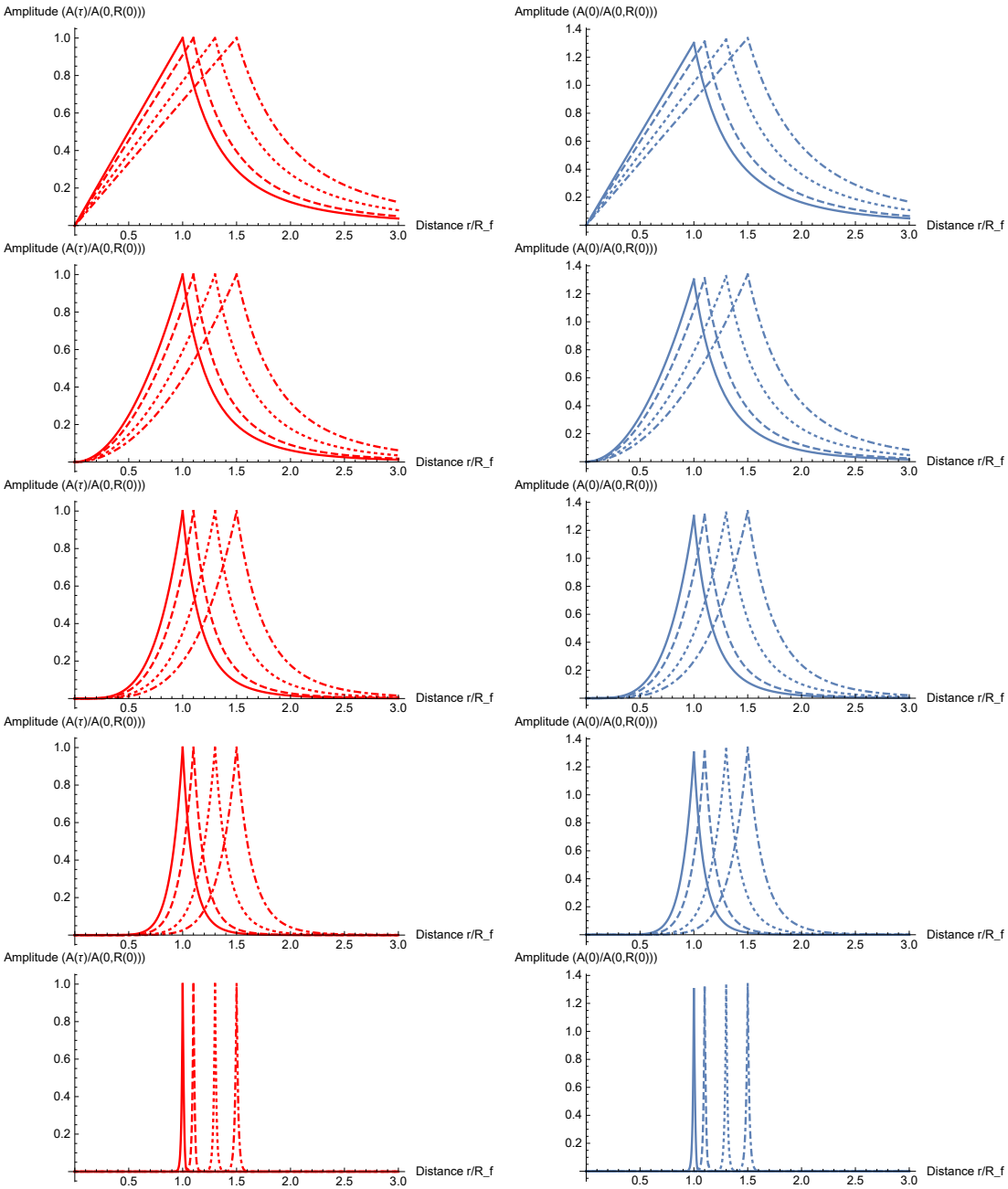

Figure 6.2: The dependence of dimensionless amplitude on r/R_f. Left panels correspond to amplitude variation at the initial time $\tau = 0$, right panels corresponds to amplitude variation at final time $\tau = 1$. Solid, dashed, dotted and dash-dotted lines correspond to $\lambda = 1$, $= 1.1$, $= 1.3$, 1.5, respectively. From top to bottom panels correspond to $\tilde{m} = 2$, $= 3$, $= 5$, $= 10$ and $= 100$, respectively.

This could be especially observed at the bottom panels of Figure 6.2, where oscillations occur close to the tube boundary magnetic field lines to such extend, that even the region above the boundary in the footpoints would not oscillate at the apex of the tube for even mildly expanded flux tube. Now, it follows from figure 6.3 that ζ has no effect on initial amplitude variation on the distance from the core region. On the other hand, at final time $\tau = 1$, it is possible to observe three separate phenomena. First of all, increasing the wave number $\tilde{m}$ localises the oscillation closer to the boundary. Secondly, the higher the value of ζ is the stronger the amplification of oscillations due to cooling. Finally, the increase in $\tilde{m}$ leads to reduction in the spread between oscillation variation across the tube for different values of ζ, preserving the trend the higher the value of ζ the higher is the amplification due to cooling.

Figure 6.4 represents the evolution of oscillation of magnetic flux tube both through time and distance from the annulus. We see that for both the top and bottom panels the amplitude increases with time. Furthermore, higher values of $\tilde{m}$ lead to localisation of oscillation closer to the boundary. On the other hand, an increasing expansion factor λ not only leads to increase of the oscillation amplitude but also shifts the localisation of oscillation of the magnetic flux tube further from the center. As a result, we note that not only $\tilde{m}$ has an important role in the evolution of the cooling system but also, variation of expansion λ and density ratio ζ, with the latest one having significant deviation between initial and final time.

§ 6.5 Summary

In this chapter, we studied the oscillations of fluting modes for an expanding magnetic flux tube in the presence of a bulk flow. The plasma density and the velocity vary both in space and with time. However, we assume that the characteristic scale of variation of these quantities along the loop and across the loop are the same order and may vary in a thin transitional layer. Starting from the linearised MHD equations, with the aid of multi-scale expansion, we derived Equations (6.34) – (6.39) that govern the flute oscillations of a magnetic flux tube, both for standing and propagating waves. This system is closed in the absence of a transitional layer. However, with the transitional layer being present, additional information is needed to solve the governing equations, since jumps of pressure and displacement may manifest within the system. In order to close this system, these jumps should be expressed in terms of the displacement.

The derived set of equations is then used to study the effect of density variation with time on oscillations for a magnetic flux tube. We have assumed that the characteristic time of the density variation is much greater than the characteristic time of the oscillation. Via the WKB method, we were able to derive an adiabatic invariant (the quantity which is conserved while plasma density evolves).
Furthermore, by considering cooling of a curved magnetic flux tube with ends fixed to dense photosphere, i.e. imposing line-tying, we numerically solved the system of governing equations. First of all, we found that for all values of m, the oscillation amplitude amplifies with time. The same conclusion was made previously by Ruderman et al. (2017) for kink modes. Moreover, the higher the value of m is, the closer the

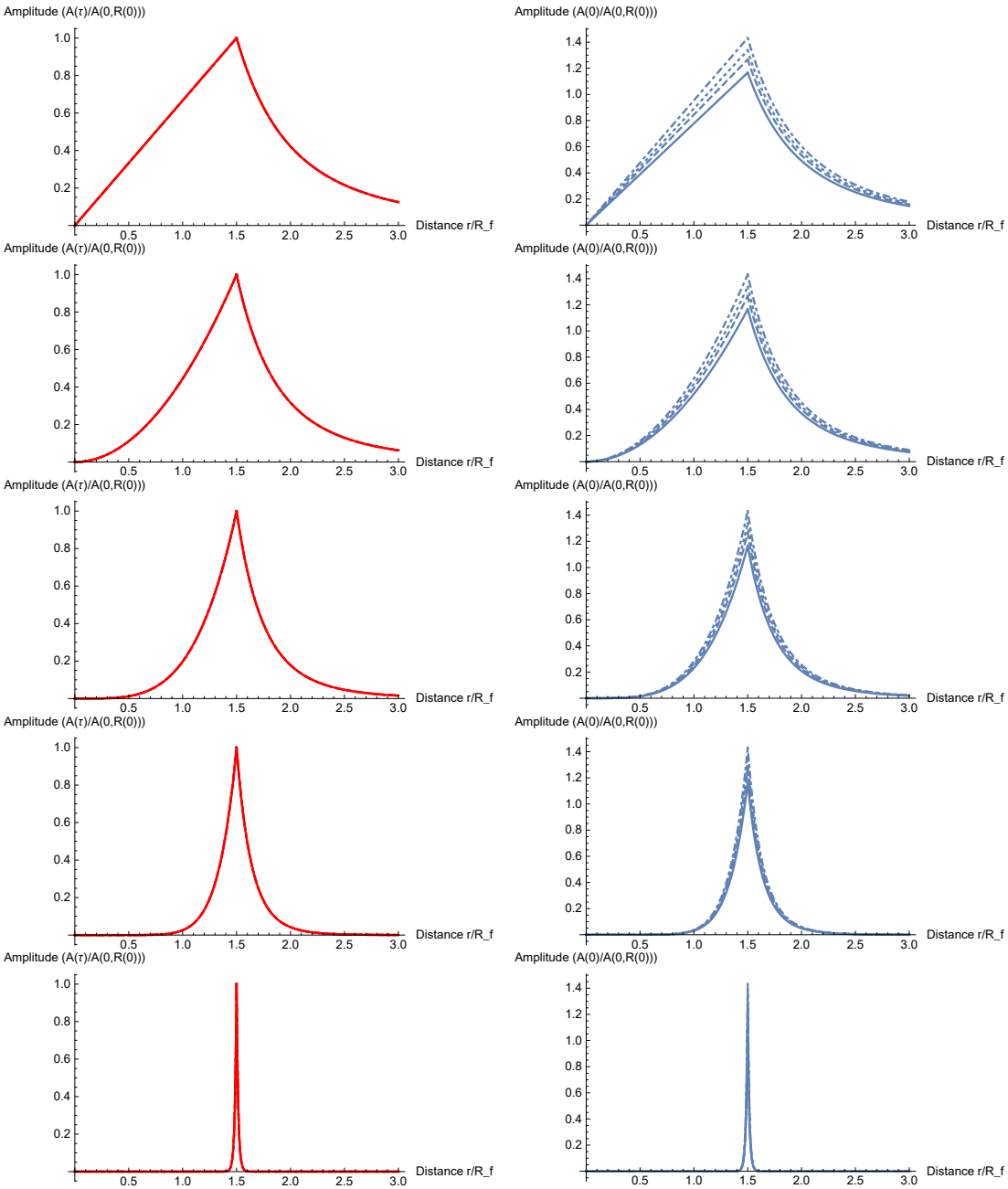

Figure 6.3: The dependence of dimensionless amplitude on r/R_f. Left panels correspond to amplitude variation at the initial time $\tau = 0$, right panels corresponds to amplitude variation at final time $\tau = 1$. Solid, dashed, dotted and dash-dotted lines correspond to $\zeta = 1, = 2, = 3, = 4$, respectively. From top to bottom panels correspond to $\tilde{m} = 2, = 3, = 5, = 10$ and $= 100$, respectively

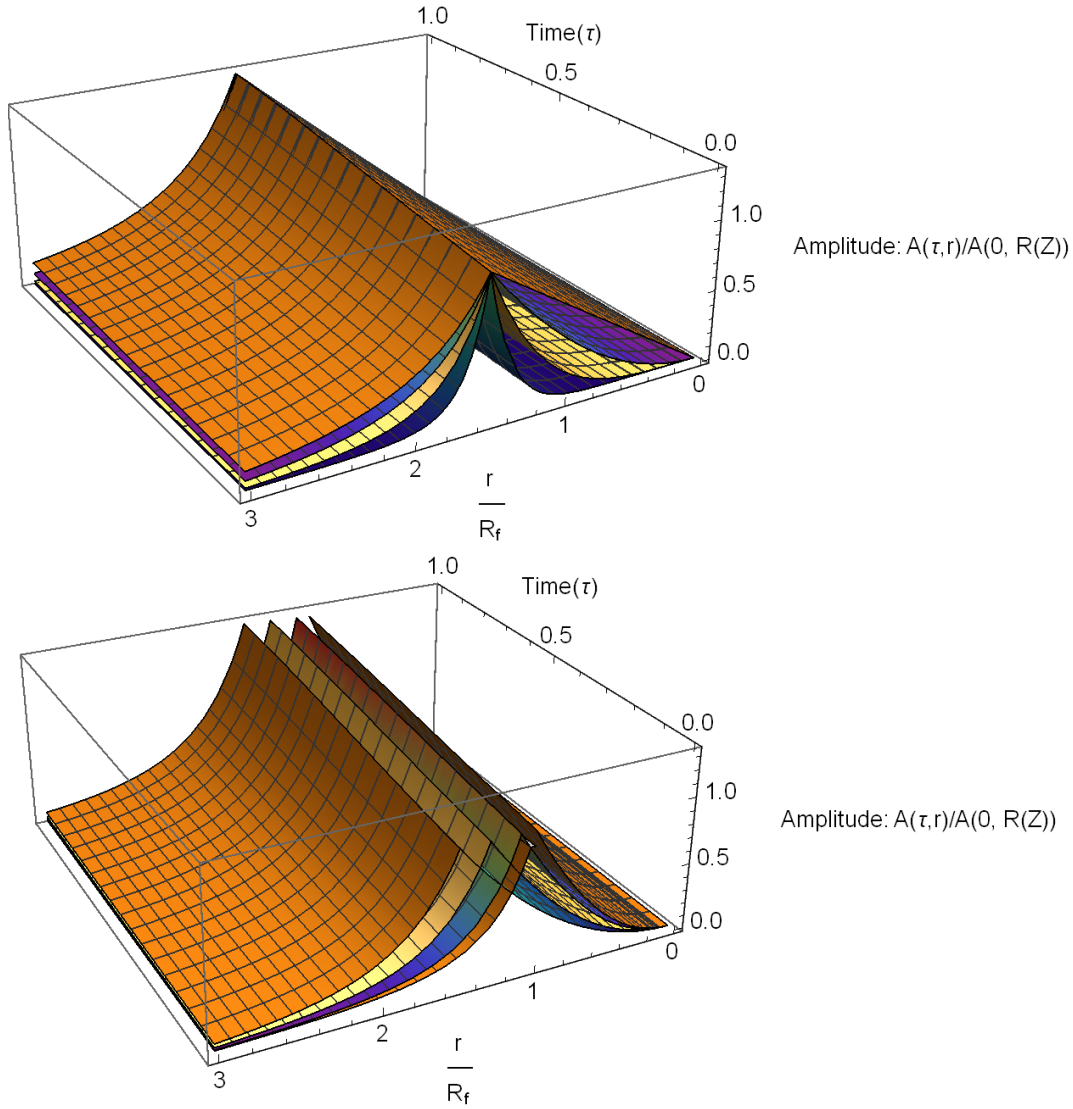

Figure 6.4: The dependence of dimensionless amplitude on r/R_f and time τ for $\zeta = 3$. Orange, purple, yellow, dark purple color scheme correspond at top panel to $\tilde{m} = 2$, $= 3$, $= 4$, $= 5$ respectively and in bottom panel to $\lambda = 1.1$, 1.2, $= 1.3$ and $= 1.5$ respectively. Top panel has fixed value of $\zeta = 1.5$ and bottom panel has fixed value of $\tilde{m} = 3$

oscillation to the boundary, where this effect is becoming less prominent as time passes, with similar conclusion being recorded previously (e.g. Soler, 2017).
We also found that the expansion factor not only shifts the oscillation localisation toward higher values, but also modifies the oscillation variation pattern.
Another fascinating phenomenon found is that the higher the density ratio between the external and internal plasma is the stronger the amplification for all values of m. As a result, higher density contrast results in stronger oscillation. Furthermore, although the higher the value of m is the more localised towards the boundary of the oscillation, nevertheless, the increase in values of the density ratio ζ allows some compensation of these events by shifting the oscillation from the boundary. That effect adds additional knowledge to previous understanding of flute oscillation, which suggested that oscillation is concentrated on the boundary of the object.
Last but not least, we note that a correct combination of a magnetic flux tube expansion and the ratio between internal and external density could negate the effect of increase due to higher azimuthal wave number. Thus, making it possible for high m flute modes, not only to present properties of surface waves, but also body waves.

Chapter 7

Conclusions

The thesis presents developments of theoretical models of MHD wave propagation in magnetic slab and magnetic flux tube environments, as well as applications of these contemporary theoretical models to solar physics. The structure of the thesis is build on a series of my previous works Shukhobodskaia and Erdélyi (2018), Allcock et al. (2019), Ruderman et al. (2019), Shukhobodskaia et al. (2020) and Shukhobodskaia et al. (2021). The MHD approximation and the corresponding equations are used in this thesis to describe plasma evolution in the Sun's atmosphere. Furthermore, the obtained theory is tested and validated with solar observations.

There is potential applicability as an SMS diagnostic tool of our current multi-slab model presented in Chapters 2 and 3. We have illustrated that the spatial distribution of the oscillation amplitudes depend on the type of structuring of the equilibrium model. We have also shown that in asymmetric (multi-)slab configurations, the oscillation amplitudes are *different* at the boundaries of these slabs. Since these amplitude ratios are observable, assuming adequate instrumental resolution is available, knowing them and some other parameters such as the wave frequency, wavelength or magnetic and non-magnetic slab widths, further equilibrium parameters of the MHD waveguide could be diagnosed and determined.
The property of the oscillation amplitude ratio is proposed to be seen as a novel diagnostic tool to unveil the approximate structuring of local solar multi-layered MHD waveguides, analogous to Allcock and Erdélyi (2018) for a single asymmetric waveguide. Furthermore, there is another distinct property of the oscillations in asymmetric slab equilibria that could be exploited for SMS: namely the discontinuity in the derivatives in the (velocity) perturbation as shown here, (or for other eigenfunctions, like magnetic field, etc.) could be exploited for indication of the actual structuring present that should be taken into account when modelling the wave propagation in such media. Such discontinuities may be deduced from suitable time-distance plots of a given oscillating asymmetric MHD waveguide, yielding further evidence about its structuring.

A direct application of the considered model might be the analysis of wave propagation in elongated MBPs of the solar photosphere. Knowing the characteristic parameters of neighbouring granular cells, one would be able to find out what is the least

amount of granular cells that one should consider for a correct description of waves in MBPs. With the completion of the next generation of solar telescopes with ultra-high resolution, *e.g.* the Daniel K. Inouye Solar Telescope (DKIST), significant improvement is expected in studying wave phenomena in MBPs. Therefore these opportunities provide and enable a better addressing of the wave coupling between the solar photosphere and the lower solar atmosphere above it. Further applications to MHD wave diagnostics of e.g. sunspot light bridges, light walls, or the oscillations in the filamentary structure of sunspot penumbrae could be made.

Recent high-resolution state-of-the-art ground-based or space-borne observations, as detailed above, clearly show that there is strong structuring (inhomogeneity) and dynamics in the observed solar (and magnetospheric) MHD waveguides. Solar MHD wave theory is boosted by the development of solar magneto-seismology; see the avalanche of Space Sci. Reviews since 2010 (e.g. Pintér and Erdélyi, 2011, McLaughlin et al., 2011, Goossens et al., 2011). SMS is an excellent tool to obtain sub-resolution information about MHD waveguides present in the Sun. It was shown by Allcock et al. (2019) that MHD waveguides can be used as a proof-of-concept in solar plasma diagnostics. This latter result has an additional importance, given that the field of solar physics is at the brink of its greatest historic development: the commencing of our 4 m aperture ground-based DKIST telescope.

In Chapter 4, the propagation of MHD waves was studied in cylindrical waveguides with variable cross section. The density varied both in space and time along the flux tube. In the thin tube approximation, the equations which govern such system were obtained and solved numerically, for an environment with varying cooling properties. Interestingly stronger cooling contributes to longer distance travelled by the wavefront in a given time. However, the effect on the wave number is inconclusive. Furthermore, cooling increases both wave amplitude and wave frequency. The applications of such theory are vast and yet to be tested in observations, as it was suggested by Pascoe et al. (2020). Other structures such as e.g. prominences could be also investigated with the work presented in this thesis. This shows significant importance of magnetic flux tube technique for solar magneto-seismology, both in theoretical and observational aspects.

It was shown by Shukhobodskiy et al. (2018) that higher expansion factors of coronal loops could result in overall amplification of the first part of the oscillation eventually resulting in Gaussian decay of the amplitude profile. Thus, studying complex damping profiles, could allow us to extract interesting seismological information, such as the ratios of densities at foot-points. Chapter 5 is concentrating on such a study. Furthermore, the information presented in Fig. 5.6 suggests, that lower ratios of internal and external densities have higher amplitude and period. One of the reasons why this could happen is that the coronal loops investigated are lighter and less disturbance created by the flare is needed to disturb the system more prominently. A larger statistical study and more targeted observations with spectral instruments suitable for providing density diagnostics (such as IRIS) should be used to study this potenatial result in more detail in the future.

Overall, we presented an alternative approach to model more complex damping profiles that deviate from the widely studied Gaussian and exponential decays. A

number of examples of such deviation were addressed in this study, thus strengthening the claim made by Nelson et al. (2019) that the effect of cooling should be further considered for analysing oscillations of coronal loops. This is in agreement with some earlier studies, e.g. by Morton and Erdélyi (2009, 2010). Furthermore, in the case of strong damping the theoretical model proposed by Shukhobodskiy et al. (2018) is able to provide seismological information, just from the damping profile alone. For some events, the cooling model demonstrated significant improvement over standard Gaussian on exponential fitting when χ^2 goodness of fits were calculated. We should note that the results employed from Shukhobodskiy et al. (2018) model were applied to the fundamental mode only. However, additional studies with inclusion of mode mixing would allow comparison with other fitting techniques that allow multiple harmonics to be present, which could further unveil details regarding kink oscillations of coronal loops. Unfortunately, for less dominant damping more parameters need to be determined from observation in order to extract the information about the kink oscillations of coronal loops.

Although a limited evidence is presented about the actual cooling for the events studied here, it is still possible that the gradual fading of the intensity of several coronal loops presented in Fig. 5.1 (specifically for Events 03 01, 04 01, and 43 05) may imply that some thermal evolution (either heating or cooling) is present. In a future work, it would be worthwhile to analyse oscillations within loops which are undergoing specific processes linked to cooling. Examples could be such as coronal rain (Antolin et al. 2015) or the associated high velocity transition region downflows (see *e.g.* Nelson et al. 2020b,a and literature within), to understand whether abnormal amplitude profiles through time (such as those studied here) are present. Additionally, it would be worthwhile to develop further the analytical methods. This, then, could help to extract additional information about the kink oscillation of coronal loops, in order to optimise this theory for the application of solar magneto-seismology to kink-mode oscillations.

Finally in Chapter 6 the fluting mode of magnetic flux tube was investigated under solar coronal conditions. It was already shown previously theoretically that flute modes could couple and contribute to kink oscillation. This yet to be observed phenomenon could result in improving our understating of the damping of kink oscillation of coronal loops. Starting from the linearised MHD equations, the set of equations which govern the magnetic flux tube was obtained. Theses equations are valid both for standing and propagating waves. The so-called transitional layer was later removed from investigation to study the effect of the wave number m, density ratio ζ and expansion factors λ for cooling magnetic flux tube. It was shown that cooling enhances the oscillation amplitudes with time, for all values of m. More interestingly, although similarly to previous studies, e.g Soler (2017), it was found that higher values of m localise the oscillations to the surface, and changing the values of ζ and λ could compensate such effect. This latter could add extra level of freedom for interpreting wave observations in order to understand mysteries of the Sun.

§ 7.1 Future work

The work presented in this thesis provides unprecedented opportunities for a number of applications of theoretical MHD models. The further development in both magnetic slab and magnetic flux tube environments would allow us to investigate such complex phenomena as solar jets. In case of the first framework, the slab could be fixed to the photosphere, with the magnetic field being directed away from the photosphere in the direction of solar corona. Such a simplistic approach may lead to the discovery of mechanisms responsible for jet formation and evolution, which are currently unknown. Moreover, the same could be potentially achieved by employing the magnetic flux tube framework and fixing the tube to the dense photosphere. The tube would be twisted and, instead of expansion, the tube would contract in radial direction.

Another possible way of reaping the benefits from this thesis is to continue to investigate kink oscillations of coronal loops by means of a theoretical model that incorporates cooling and expansion. First of all, it seems from the theoretical model that the cooling time varies the shape of oscillations. Further studies in this direction could potentially lead to the production of estimates that would allow us to describe kink oscillations in a more accurate way. Furthermore, the theoretical model could be enhanced by itself. Recently conducted research suggests that multiple harmonics are present within kink oscillations of coronal loops (Pascoe et al., 2016b). A carefully produced theoretical model, which incorporates cooling and mode coupling, might further clarify such findings and enhance understanding of the process. Finally, it would be interesting to automate the process of this newly developed technique in order to accumulate significant amount of data and compare the method with widespread DEM analysis.

The framework of magnetic flux tube has widely recommended itself in the past to provide a theoretical model for descriptions not only of coronal loops but also of prominences and filaments. Since observations suggest that both structures could potentially be twisted, there would be ultimate interests to incorporate magnetic twists within modelling the flux tubes and obtain analytical solution to the problem. Construction of such analytical model, which also has magnetic flux tube expansions, presence of flow and twist, could potentially lead to better understanding of the MHD wave phenomenon in the solar atmosphere. Moreover, due to lack of resolution in the observations, we do not know up to what extent the standard assumption that the flux tube is circular is a correct one. Some previous studies computed the effect of the shape on processes. As a next step advancement, implementation of different shapes of cross-section, for example elliptical one, may better estimate the wave process from basic physical principles.

Summarising all of the above, it is safe to conclude that the thesis provides a significant advancement in the development and application of contemporary MHD wave theory to solar observations. Furthermore, the thesis is stressing on the importance of theoretical advancement that could lead to a better approach or create different perspectives in the understanding of solar magneto-seismology. We provided a few clear steps of what kind of advancements could be made in order to further test and validate our models, in both the magnetic slab and magnetic flux tube frameworks.

Appendix A

Boundary conditions in matrix form

It is possible to rewrite the boundary conditions (2.13) in matrix form (2.14), where $\mathbf{M}$ has dimension $[4+2(p+q)] \times [4+2(n+q)]$. The precise form of the matrix, with the first row corresponding to the continuity of the velocity at $x = -x_p^L$, is:

$$\begin{aligned} \mathbf{M}[1,1] &= \cosh m_{p+1}^L x_p^L - \sinh m_{p+1}^L x_n^L, \\ \mathbf{M}[1,2] &= -\cosh m_p^L x_p^L, \quad \mathbf{M}[1,3] = \sinh m_p^L x_p^L. \end{aligned} \tag{A.1}$$

The second row represents the continuity of the total pressure at $x = -x_p^L$:

$$\begin{aligned} \mathbf{M}[2,1] &= \Lambda_{p+1}^L (\cosh m_{p+1}^L x_p^L - \sinh m_{p+1}^L x_p^L) \\ \mathbf{M}[2,2] &= \Lambda_n^L \sinh m_p^L x_p^L, \quad \mathbf{M}[2,3] = -\Lambda_p^L \cosh m_p^L x_p^L. \end{aligned} \tag{A.2}$$

The penultimate row corresponds to the continuity of the velocity at $x = x_q^R$:

$$\begin{aligned} \mathbf{M}[2(p+q)+3, 2(p+q)+2] &= \cosh m_q^R x_q^R, \\ \mathbf{M}[2(p+q)+3, 2(p+q)+3] &= \sinh m_q^R x_q^R, \\ \mathbf{M}[2(p+q)+3, 2(p+q)+4] &= \sinh m_{q+1}^R x_q^R - \cosh m_{q+1}^R x_q^R. \end{aligned} \tag{A.3}$$

Finally, the last row that represents the continuity of the total pressure at $x = x_q^R$, and is:

$$\begin{aligned} \mathbf{M}[2(p+q)+4, 2(p+q)+2] &= \Lambda_q^R \sinh m_q^R x_q^R, \\ \mathbf{M}[2(p+q)+4, 2(p+q)+3] &= \Lambda_q^R \cosh m_q^R x_q^R, \\ \mathbf{M}[2(p+q)+4, 2(p+q)+4] &= \Lambda_{q+1}^R (\cosh m_{q+1}^R x_q^R - \sinh m_{q+1}^R x_q^R). \end{aligned} \tag{A.4}$$

For $1 \leq i \leq p$, the general boundary condition on the left regions takes the form

$$\begin{aligned}
\mathbf{M}[2i+1,2i] = \cosh m^L_{p-i+1}x^L_{(p-i)}, \quad \mathbf{M}[2i+1,2i+1] = -\sinh m^L_{p-i+1}x^L_{(p-i)},\\
\mathbf{M}[2i+1,2i+2] = -\cosh m^L_{p-i}x^L_{(p-i)}, \quad \mathbf{M}[2i+1,2i+3] = \sinh m^L_{p-i}x^L_{(p-i)},\\
\mathbf{M}[2i+2,2i] = -\Lambda^L_{p-i+1}\sinh m^L_{p-i+1}x^L_{(p-i)},\\
\mathbf{M}[2i+2,2i+1] = \Lambda^L_{p-i+1}\cosh m^L_{p-i+1}x^L_{(p-i)},\\
\mathbf{M}[2i+2,2i+2] = \Lambda^L_{p-i}\sinh m^L_{p-i}x^L_{(p-i)},\\
\mathbf{M}[2i+2,2i+3] = -\Lambda^L_{p-i}\cosh m^L_{p-i}x^L_{(p-i)}. \quad \text{(A.5)}
\end{aligned}$$

For $p+1 \leq i \leq p+q$, the general boundary condition on the right **regions** is

$$\begin{aligned}
\mathbf{M}[2i+1,2i] = \cosh m^R_{i-p-1}x^R_{(i-p-1)}, \quad \mathbf{M}[2i+1,2i+1] = \sinh m^R_{i-p-1}x^R_{(i-p-1)},\\
\mathbf{M}[2i+1,2i+2] = -\cosh m^R_{i-p}x^R_{(i-p-1)}, \quad \mathbf{M}[2i+1,2i+3] = -\sinh m^R_{i-p}x^R_{(i-p-1)},\\
\mathbf{M}[2i+2,2i] = \Lambda^R_{i-p-1}\sinh m^R_{i-p-1}x^R_{(i-p-1)},\\
\mathbf{M}[2i+2,2i+1] = \Lambda^R_{i-p-1}\cosh m^R_{i-p-1}x^R_{(i-p-1)},\\
\mathbf{M}[2i+2,2i+2] = -\Lambda^R_{i-p}\sinh m^R_{i-p}x^R_{(i-p-1)},\\
\mathbf{M}[2i+2,2i+3] = -\Lambda^R_{i-p}\cosh m^R_{i-p}x^R_{(i-p-1)}. \quad \text{(A.6)}
\end{aligned}$$

For the rest of values, $\mathbf{M}[i,j] = 0$.

Appendix B

Dispersion relation for thin slab approximation

Two-slab case

Let us now derive the dispersion relation, up to first order in kx_0, under the thin-slab approximation. From Eq. (2.18), we found a power series expansions with respect to x_0 and d_1^L, namely

$$\rho_0\left(\frac{m_1^R}{\rho_1^R}+\frac{m_2^L}{\rho_2^L}\right)\omega^2\left(\omega^2-k^2v_A^2\right)+2x_0\left(m_0^2\omega^4+\frac{m_1^Rm_2^L}{\rho_1^R\rho_2^L}\rho_0^2\left(\omega^2-k^2v_A^2\right)^2\right)+$$
$$d_1^L\rho_0\left(\frac{m_1^Lm_1^L}{\rho_1^L}+\frac{m_1^Rm_2^L\rho_1^L}{\rho_1^R\rho_2^L}\right)\omega^2\left(\omega^2-k^2v_A^2\right)+$$
$$2x_0d_1^L\left(\frac{m_0^2m_2^L\rho_1^L\omega^4}{\rho_2^L}+\frac{m_1^Lm_1^Lm_1^R\rho_0^2\left(\omega^2-k^2v_A^2\right)^2}{\rho_1^L\rho_1^R}\right)+$$
$$+O[x_0]^3+O[d_1^L]^3=0. \quad \text{(B.1)}$$

If $d_1^L \ll d_0 \ll \lambda$, up to the first order in kx_0, using Eq. (B.1) we have

$$\rho_0\left(\frac{m_1^R}{\rho_1^R}+\frac{m_2^L}{\rho_2^L}\right)\omega^2\left(\omega^2-k^2v_A^2\right)+2x_0\left(m_0^2\omega^4+\frac{m_1^Rm_2^L}{\rho_1^R\rho_2^L}\rho_0^2\left(\omega^2-k^2v_A^2\right)^2\right)=0. \quad \text{(B.2)}$$

If $d_1^L \approx d_0 \ll \lambda$, again, up to the first order of approximation in kx_0, from Eq. (B.1) we obtain

$$\rho_0\left(\frac{m_1^R}{\rho_1^R}+\frac{m_2^L}{\rho_2^L}\right)\omega^2\left(\omega^2-k^2v_A^2\right)+2x_0\left(m_0^2\omega^4+\frac{m_1^Rm_2^L}{\rho_1^R\rho_2^L}\rho_0^2\left(\omega^2-k^2v_A^2\right)^2\right)+$$
$$d_1^L\rho_0\left(\frac{m_1^Lm_1^L}{\rho_1^L}+\frac{m_1^Rm_2^L\rho_1^L}{\rho_1^R\rho_2^L}\right)\omega^2\left(\omega^2-k^2v_A^2\right)=0. \quad \text{(B.3)}$$

Three-slab case

For Eq. (2.20), we obtain a power series expansions in kx_0, with respect to x_0, d_1^L, and d_1^R:

$$\begin{aligned}
&\rho_0(m_2^R\rho_2^L + m_2^L\rho_2^R)\omega^2\left(\omega^2 - k^2v_A^2\right) + 2x_0\left(m_0^2\omega^4\rho_2^L\rho_2^R + m_2^Lm_2^R\rho_0^2\left(\omega^2 - k^2v_A^2\right)^2\right) + \\
&\qquad d_1^R\frac{\rho_0}{\rho_1^R}\left(m_2^Lm_2^R\rho_1^R\rho_1^R + m_1^Rm_1^R\rho_2^L\rho_2^R\right)\omega^2\left(\omega^2 - k^2v_A^2\right) + \\
&\qquad d_1^L\frac{\rho_0}{\rho_1^L}\left(m_2^Lm_2^R\rho_1^L\rho_1^L + m_1^Lm_1^L\rho_2^L\rho_2^R\right)\omega^2\left(\omega^2 - k^2v_A^2\right) + \\
&\qquad 2x_0\frac{d_1^R}{\rho_1^R}\left[m_0^2m_2^R\rho_1^R\rho_1^R\rho_2^L\omega^4 + m_1^Rm_1^Rm_2^L\rho_0^2\rho_2^R\left(\omega^2 - k^2v_A^2\right)^2\right] + \\
&\qquad 2x_0\frac{d_1^L}{\rho_1^L}\left[m_0^2m_2^L\rho_1^L\rho_1^L\rho_2^R\omega^4 + m_1^Lm_1^Lm_2^R\rho_0^2\rho_2^L\left(\omega^2 - k^2v_A^2\right)^2\right] + \\
&\frac{d_1^Rd_1^L}{\rho_1^L\rho_1^R}\left[\rho_0\left(m_1^Lm_1^Lm_2^R\rho_1^R\rho_1^R\rho_2^L + m_1^Rm_1^Rm_2^L\rho_1^L\rho_1^L\rho_2^R\right)\omega^2\left(\omega^2 - k^2v_A^2\right)\right] + \\
&\qquad +O[x_0]^3 + O[d_1^R]^3 + O[d_1^L]^3 = 0. \qquad \text{(B.4)}
\end{aligned}$$

If $d_1^L \approx d_1^R \ll d_0 \ll \lambda$, up to first order in kx_0, from Eq. (B.4) we acquire

$$\begin{aligned}
&\rho_0(m_2^R\rho_2^L + m_2^L\rho_2^R)\omega^2\left(\omega^2 - k^2v_A^2\right) + \\
&+2x_0\left(m_0^2\omega^4\rho_2^L\rho_2^R + m_2^Lm_2^R\rho_0^2\left(\omega^2 - k^2v_A^2\right)^2\right) = 0. \qquad \text{(B.5)}
\end{aligned}$$

If $d_1^L \approx d_1^R \approx d_0 \ll \lambda$, from Eq. (B.4) we have

$$\begin{aligned}
&\rho_0(m_2^R\rho_2^L + m_2^L\rho_2^R)\omega^2\left(\omega^2 - k^2v_A^2\right) + 2x_0\left(m_0^2\omega^4\rho_2^L\rho_2^R + m_2^Lm_2^R\rho_0^2\left(\omega^2 - k^2v_A^2\right)^2\right) + \\
&\qquad d_1^R\frac{\rho_0}{\rho_1^R}\left(m_2^Lm_2^R\rho_1^R\rho_1^R + m_1^Rm_1^R\rho_2^L\rho_2^R\right)\omega^2\left(\omega^2 - k^2v_A^2\right) + \\
&\qquad d_1^L\frac{\rho_0}{\rho_1^L}\left(m_2^Lm_2^R\rho_1^L\rho_1^L + m_1^Lm_1^L\rho_2^L\rho_2^R\right)\omega^2\left(\omega^2 - k^2v_A^2\right) = 0. \qquad \text{(B.6)}
\end{aligned}$$

Appendix C

Boundary conditions in matrix form

We rewrite the boundary conditions (3.7) in the compact matrix form (3.9) with $[2n+2]\times[2n+2]$ matrix $\mathbf{M}$. The precise form of the matrix with the first row corresponding to the continuity of the velocity at $x = x_0$, is

$$\begin{aligned}\mathbf{M}[1,1] &= \cosh m_0 x_0 + \sinh m_0 x_0,\\ \mathbf{M}[1,2] &= -\cosh m_1 x_0, \quad \mathbf{M}[1,3] = -\sinh m_1 x_0.\end{aligned} \tag{C.1}$$

The second row represents the continuity of the total pressure at $x = x_0$:

$$\begin{aligned}\mathbf{M}[2,1] &= \Lambda_0(\cosh m_0 x_0 + \sinh m_0 x_0),\\ \mathbf{M}[2,2] &= -\Lambda_1 \sinh m_1 x_0, \quad \mathbf{M}[2,3] = -\Lambda_1 \cosh m_1 x_0.\end{aligned} \tag{C.2}$$

The last but one row corresponds to the continuity of the velocity at $x = x_n$:

$$\begin{aligned}\mathbf{M}[2n+1,2n] &= \cosh m_n x_n, \quad \mathbf{M}[2n+1,2n+1] = \sinh m_n x_n,\\ \mathbf{M}[2n+1,2n+2] &= \sinh m_{n+1} x_n - \cosh m_{n+1} x_n.\end{aligned} \tag{C.3}$$

Finally, the last row represents the continuity of the total pressure at $x = x_n$ and is

$$\begin{aligned}\mathbf{M}[2n+2,2n] &= \Lambda_n \sinh m_n x_n, \quad \mathbf{M}[2n+2,2n+1] = \Lambda_n \cosh m_n x_n,\\ \mathbf{M}[2n+2,2n+2] &= \Lambda_{n+1}(\cosh m_{n+1} x_n - \sinh m_{n+1} x_n).\end{aligned} \tag{C.4}$$

For $1 \le j \le n-1$, general boundary condition takes the form

$$\begin{aligned}\mathbf{M}[2j+1,2j] &= \cosh m_j x_j, \quad \mathbf{M}[2j+1,2j+1] = \sinh m_j x_j,\\ \mathbf{M}[2j+1,2j+2] &= -\cosh m_{j+1} x_j, \quad \mathbf{M}[2j+1,2j+3] = -\sinh m_{j+1} x_j,\\ \mathbf{M}[2j+2,2j] &= \Lambda_j \sinh m_j x_j, \quad \mathbf{M}[2j+2,2j+1] = \Lambda_j \cosh m_j x_j,\\ \mathbf{M}[2j+2,2j+2] &= -\Lambda_{j+1} \sinh m_{j+1} x_j, \quad \mathbf{M}[2j+2,2j+3] = -\Lambda_{j+1} \cosh m_{j+1} x_j.\end{aligned} \tag{C.5}$$

For the rest of the values i and j, $\mathbf{M}[i,j] = 0$. Introducing the notation $C_j^{(i)} = \cosh m_i x_j$, $S_j^{(i)} = \sinh m_i x_j$ and using Equations (C.1)-(C.5), the matrix in explicit

form can be written as:

$$
\begin{pmatrix}
C_0^{(0)}+S_0^{(0)} & -C_0^{(1)} & -S_0^{(1)} & 0 & \cdots & \cdots & \cdots & 0 & 0 & 0 & 0 \\
\Lambda_0(C_0^{(0)}+S_0^{(0)}) & -\Lambda_1 S_0^{(1)} & -\Lambda_1 C_0^{(1)} & 0 & \cdots & \cdots & \cdots & 0 & 0 & 0 & 0 \\
0 & C_1^{(1)} & S_1^{(1)} & -C_1^{(2)} & -S_1^{(2)} & 0 & \cdots & 0 & 0 & 0 & 0 \\
 & \Lambda_1 S_1^{(1)} & \Lambda_1 C_1^{(1)} & -\Lambda_2 S_1^{(2)} & -\Lambda_2 C_1^{(2)} & 0 & & \vdots & \vdots & \vdots & \vdots \\
0 & \vdots & \vdots & \vdots & & & \ddots & & & & \\
 & 0 & 0 & 0 & \cdots & \cdots & \cdots & C_{n-1}^{(n-1)} & -C_{n-1}^{(n)} & -S_{n-1}^{(n)} & 0 \\
0 & 0 & 0 & 0 & \cdots & \cdots & \cdots & \Lambda_{n-1}S_{n-1}^{(n-1)} & -\Lambda_n S_{n-1}^{(n)} & -\Lambda_n C_{n-1}^{(n)} & 0 \\
0 & 0 & 0 & 0 & \cdots & \cdots & \cdots & 0 & C_n^{(n)} & S_n^{(n)} & S_n^{(n+1)} \\
0 & 0 & 0 & 0 & \cdots & \cdots & \cdots & 0 & \Lambda_n S_n^{(n)} & \Lambda_n C_n^{(n)} & \Lambda_{n+1}(C_n^{(n+1)}-S_n^{(n+1)})
\end{pmatrix}
\tag{C.6}
$$

Appendix D

Solution to Eq. 4.54

In this section, we obtain the solution to Eq. (4.54) satisfying the asymptotic condition Eq. (4.57). To simplify the calculations, we introduce the notation

$$\Psi = \frac{\psi - \psi_A}{RB\delta_A}, \quad h = \frac{\rho_i S(C_k^2 - V_{Ai}^2)}{\rho_A B \Delta \delta_A}. \tag{D.1}$$

Using this notation we rewrite Eq. (4.54) as

$$\Psi \hat{\xi}_\varphi + i\frac{\partial^2 \hat{\xi}_\varphi}{\partial \Psi^2} = -ih. \tag{D.2}$$

To solve this equation we use the Fourier transform with respect to Ψ defined by

$$\mathcal{F}[\hat{\xi}_\varphi] = \int_{-\infty}^{\infty} \hat{\xi}_\varphi e^{-i\sigma\Psi} d\Psi, \quad \hat{\xi}_\varphi = \frac{1}{2\pi}\int_{-\infty}^{\infty} \mathcal{F}[\hat{\xi}_\varphi] e^{i\sigma\Psi} d\sigma. \tag{D.3}$$

Applying this transform to Eq. (D.2) we obtain

$$\frac{\partial}{\partial \sigma}\mathcal{F}[\hat{\xi}_\varphi] + \sigma^2 \mathcal{F}[\hat{\xi}_\varphi] = -2\pi h \delta(\sigma), \tag{D.4}$$

where $\delta(\sigma)$ is the delta-function. The solution to this equation decaying as $|\sigma| \to \infty$ is given by

$$\mathcal{F}[\hat{\xi}_\varphi] = -2\pi h H(\sigma) e^{-\sigma^3/3}, \tag{D.5}$$

where $H(\sigma)$ is the Heaviside step function. Calculating the inverse Fourier transform we obtain

$$\hat{\xi}_\varphi = -h\int_0^{\infty} \exp\left(i\sigma\Psi - \tfrac{1}{3}\sigma^3\right) d\sigma. \tag{D.6}$$

Using the integration by parts we obtain the asymptotic expression valid for $|\Psi| \gg 1$,

$$\hat{\xi}_\varphi = -\frac{ih}{\Psi} + \mathcal{O}\big(\Psi^{-2}\big). \tag{D.7}$$

Using Eq. (D.1) it is straightforward to verify that Eq. (D.7) coincides with Eq. (4.57).

Appendix E

Evaluation of integral in Eq. 63

In this section, we evaluate the integral on the right-hand side of Eq. (4.67) for $|\Psi \gg 1$. We immediately obtain

$$\int_{-\Psi}^{\Psi} \left(\Psi_1 G(\Psi_1) - \frac{dF}{d\Psi_1} \right) d\Psi_1 = -F(\Psi) + F(-\Psi) + \int_{-\Psi}^{\Psi} \Psi_1 G(\Psi_1)\, d\Psi_1. \tag{E.1}$$

It is obvious that

$$F(\Psi) - F(-\Psi) = 2i \int_0^{\infty} \sin(\sigma\Psi)\, e^{-\sigma^3/3} d\sigma = \mathcal{O}(1). \tag{E.2}$$

Changing the order of integration we obtain

$$\int_{-\Psi}^{\Psi} \Psi_1 G(\Psi_1)\, d\Psi_1 = 2i \int_0^{\infty} [\sin(\sigma\Psi) - (\sigma\Psi)\cos(\sigma\Psi)] \frac{e^{-\sigma^3/3}}{\sigma^3} d\sigma. \tag{E.3}$$

Then, using the integration by parts yields

$$\int_{-\Psi}^{\Psi} \Psi_1 G(\Psi_1)\, d\Psi_1 = i\Psi^2 \int_0^{\infty} \frac{\sin(\sigma\Psi)}{\sigma} e^{-\sigma^3/3} d\sigma + I(\Psi), \tag{E.4}$$

where

$$I(\Psi) = i \int_0^{\infty} [(\sigma\Psi)\cos(\sigma\Psi) - \sin(\sigma\Psi)]\, e^{-\sigma^3/3} d\sigma. \tag{E.5}$$

Again using the integration by parts we obtain

$$I(\Psi) = i \int_0^{\infty} \left(\sigma^3 - 2\right) \sin(\sigma\Psi) e^{-\sigma^3/3} d\sigma = \mathcal{O}(1). \tag{E.6}$$

With the aid of the variable substitution we obtain

$$\int_0^{\infty} \frac{\sin(\sigma\Psi)}{\sigma} e^{-\sigma^3/3} d\sigma = \int_0^{\infty} \frac{\sin\sigma}{\sigma} e^{-\sigma^3/3\Psi^2} d\sigma = \frac{\pi}{2}[1 + o(1)]. \tag{E.7}$$

Using Eqs. (E.1), (E.2), (E.4), (E.6), and (E.7) we finally arrive at

$$\int_{-\Psi}^{\Psi} \left(\Psi_1 G(\Psi_1) - \frac{dF}{d\Psi_1} \right) d\Psi_1 = \frac{\pi i}{2} \Psi^2 [1 + o(1)]. \tag{E.8}$$

References

Abbo, L., Ofman, L., Antiochos, S. K., Hansteen, V. H., Harra, L., Ko, Y. K., Lapenta, G., Li, B., Riley, P., Strachan, L., von Steiger, R., and Wang, Y. M. (2016). Slow Solar Wind: Observations and Modeling. *Space Sci. Rev.*, 201(1-4):55–108.

Al-Ghafri, K. S. and Erdélyi, R. (2013). Effect of Variable Background on an Oscillating Hot Coronal Loop. *Solar Phys.*, 283(2):413–428.

Al-Ghafri, K. S., Ruderman, M. S., Williamson, A., and Erdélyi, R. (2014). Longitudinal Magnetohydrodynamics Oscillations in Dissipative, Cooling Coronal Loops. *Astrophys. J., submitted*, 786.

Alfvén, H. (1947). Magneto hydrodynamic waves, and the heating of the solar corona. *Mon. Not. Roy. Astron. Soc.*, 107:211.

Allcock, M. and Erdélyi, R. (2017). Magnetohydrodynamic Waves in an Asymmetric Magnetic Slab. *Solar Physics*, 292(2):35.

Allcock, M. and Erdélyi, R. (2018). Solar Magnetoseismology with Magnetoacoustic Surface Waves in Asymmetric Magnetic Slab Waveguides. *Astrophys. J.*, 855(2):90.

Allcock, M., Shukhobodskaia, D., Zsámberger, N. K., and Erdélyi, R. (2019). Magnetohydrodynamic waves in multi-layered asymmetric waveguides: solar magnetoseismology theory and application. *Frontiers in Astronomy and Space Sciences*, 6:48.

Andries, J., van Doorsselaere, T., Roberts, B., Verth, G., Verwichte, E., and Erdélyi, R. (2009). Coronal Seismology by Means of Kink Oscillation Overtones. *Space Sci. Rev.*, 149:3–29.

Anfinogentov, S., Nisticò, G., and Nakariakov, V. M. (2013). Decay-less kink oscillations in coronal loops. *Astron. Astrophys.*, 560:A107.

Antolin, P., Vissers, G., Pereira, T. M. D., Rouppe van der Voort, L., and Scullion, E. (2015). The Multithermal and Multi-stranded Nature of Coronal Rain. *Astrophys. J.*, 806(1):81.

Antolin, P., Yokoyama, T., and Van Doorsselaere, T. (2014). Fine Strand-like Structure in the Solar Corona from Magnetohydrodynamic Transverse Oscillations. *Astrophys. J. Lett.*, 787(2):L22.

Arregui, I. (2015). Wave heating of the solar atmosphere. *Philosophical Transactions of the Royal Society of London Series A*, 373(2042):20140261–20140261.

Arregui, R., Oliver, R., and Ballester, J. L. (2012). Prominence Oscillations. *Liv. Rev. Sol. Phys.*, 9:2.

Aschwanden, M. J. (2005). *Physics of the Solar Corona. An Introduction with Problems and Solutions (2nd edition).*

Aschwanden, M. J., Fletcher, L., Schrijver, C. J., and Alexander, D. (1999). Coronal Loop Oscillations Observed with the Transition Region and Coronal Explorer. *Astrophys. J.*, 520:880–894.

Aschwanden, M. J. and Nightingale, R. W. (2005). Elementary Loop Structures in the Solar Corona Analyzed from TRACE Triple-Filter Images. *Astrophys. J.*, 633:499–517.

Aschwanden, M. J. and Schrijver, C. J. (2011). Coronal Loop Oscillations Observed with Atmospheric Imaging Assembly Kink Mode with Cross-sectional and Density Oscillations. *Astrophys. J.*, 736:A102.

Aschwanden, M. J. and Terradas, J. (2008). The Effect of Radiative Cooling on Coronal Loop Oscillation. *Astrophys. J.*, 686:L127–L130.

Ballai, I. and Ruderman, M. S. (2011). Nonlinear Effects in Resonant Layers in Solar and Space Plasmas. *Space Sci. Rev.*, 158:421–450.

Banerjee, D., Erdélyi, R., Oliver, R., and O'Shea, E. (2007). Present and Future Observing Trends in Atmospheric Magnetoseismology. *Solar Physics*, 246:3–29.

Belcher, J. W. (1971). ALFVÉNIC Wave Pressures and the Solar Wind. *Astrophys. J.*, 168:509.

Bender, C. M. and Orszag, S. A. (1978). *Advanced Mathematical Methods for Scientists and Engineers.* New York: McGraw-Hill, 1978.

Berger, T. E. and Title, A. M. (1996). On the Dynamics of Small-Scale Solar Magnetic Elements. *Astrophys. J.*, 463:365.

Bloomfield, D. S., Lagg, A., and Solanki, S. K. (2007). The Nature of Running Penumbral Waves Revealed. *Astrophys. J.*, 671(1):1005–1012.

Coddington, E. A. and Levinson, N. (1955). *Theory of Ordinary Differential Equations.* New York: McGraw-Hill.

de Moortel, I. (2009). Longitudinal Waves in Coronal Loops. *Space Science Reviews*, 149:65–81.

De Moortel, I. and Nakariakov, V. M. (2012). Magnetohydrodynamic waves and coronal seismology: an overview of recent results. *Philosophical Transactions of the Royal Society of London Series A*, 370(1970):3193–3216.

De Pontieu, B., McIntosh, S. W., Carlsson, M., Hansteen, V. H., Tarbell, T. D., Schrijver, C. J., Title, A. M., Shine, R. A., Tsuneta, S., Katsukawa, Y., Ichimoto, K., Suematsu, Y., Shimizu, T., and Nagata, S. (2007). Chromospheric Alfvénic Waves Strong Enough to Power the Solar Wind. *Science*, 318:1574–.

De Pontieu, B., Title, A. M., Lemen, J. R., Kushner, G. D., Akin, D. J., Allard, B., Berger, T., Boerner, P., Cheung, M., Chou, C., Drake, J. F., Duncan, D. W., Freeland, S., Heyman, G. F., Hoffman, C., Hurlburt, N. E., Lindgren, R. W., Mathur, D., Rehse, R., Sabolish, D., Seguin, R., Schrijver, C. J., Tarbell, T. D., Wülser, J. P., Wolfson, C. J., Yanari, C., Mudge, J., Nguyen-Phuc, N., Timmons, R., van Bezooijen, R., Weingrod, I., Brookner, R., Butcher, G., Dougherty, B., Eder, J., Knagenhjelm, V., Larsen, S., Mansir, D., Phan, L., Boyle, P., Cheimets, P. N., DeLuca, E. E., Golub, L., Gates, R., Hertz, E., McKillop, S., Park, S., Perry, T., Podgorski, W. A., Reeves, K., Saar, S., Testa, P., Tian, H., Weber, M., Dunn, C., Eccles, S., Jaeggli, S. A., Kankelborg, C. C., Mashburn, K., Pust, N., Springer, L., Carvalho, R., Kleint, L., Marmie, J., Mazmanian, E., Pereira, T. M. D., Sawyer, S., Strong, J., Worden, S. P., Carlsson, M., Hansteen, V. H., Leenaarts, J., Wiesmann, M., Aloise, J., Chu, K. C., Bush, R. I., Scherrer, P. H., Brekke, P., Martinez-Sykora, J., Lites, B. W., McIntosh, S. W., Uitenbroek, H., Okamoto, T. J., Gummin, M. A., Auker, G., Jerram, P., Pool, P., and Waltham, N. (2014). The Interface Region Imaging Spectrograph (IRIS). *Solar Phys.*, 289(7):2733–2779.

DeForest, C. E. and Gurman, J. B. (1998). Observation of Quasi-periodic Compressive Waves in Solar Polar Plumes. *Astrophys. J. Lett.*, 501(2):L217–L220.

Díaz, A. J., Oliver, R., and Ballester, J. L. (2005). Fast magnetohydrodynamic oscillations in a multifibril Cartesian prominence model. *Astron. Astrophys.*, 440(3):1167–1175.

Díaz, A. J. and Roberts, B. (2006). Slow MHD oscillations in density structured coronal loops. *Astron. Astrophys.*, 458:975–985.

Doorsselaere, T. V., Nakariakov, V. M., and Verwichte, E. (2008). Detection of waves in the solar corona: Kink or alfvén? *The Astrophysical Journal*, 676(1):L73–L75.

Dymova, M. V. and Ruderman, M. S. (2005). Non-Axisymmetric Oscillations of Thin Prominence Fibrils. *Solar Physics*, 229:79–94.

Dymova, M. V. and Ruderman, M. S. (2006). Resonantly damped oscillations of longitudinally stratified coronal loops. *Astron. Astrophys.*, 457:1059–1070.

Edwin, P. M. and Roberts, B. (1982). Wave propagation in a magnetically structured atmosphere. III - The slab in a magnetic environment. *Solar Physics*, 76:239–259.

Edwin, P. M. and Roberts, B. (1983). Wave propagation in a magnetic cylinder. *Solar Physics*, 88:179–191.

Erdélyi, R. (2006a). Magnetic coupling of waves and oscillations in the lower solar atmosphere: can the tail wag the dog? *Royal Society of London Philosophical Transactions Series A*, 364:351–381.

Erdélyi, R. (2006b). Magnetic seismology of the lower solar atmosphere. In Fletcher, K. and Thompson, M., editors, *Proceedings of SOHO 18/GONG 2006/HELAS I, Beyond the spherical Sun*, ESA SP-624.

Erdélyi, R., Al-Ghafri, K. S., and Morton, R. J. (2011). Damping of Longitudinal Magneto-Acoustic Oscillations in Slowly Varying Coronal Plasma. *Solar Phys.*, 272(1):73–89.

Erdélyi, R. and Fedun, V. (2007). Are There Alfvén Waves in the Solar Atmosphere? *Science*, 318:1572–.

Erdelyi, R. and Goossens, M. (1994). Viscous computations of resonant absorption of MHD waves in flux tubes by fem. *Astrophys. Space Sci.*, 213(2):273–298.

Erdelyi, R. and Goossens, M. (1995). Resonant absorption of Alfven waves in coronal loops in visco-resistive MHD. *Astron. Astrophys.*, 294:575–586.

Erdélyi, R. and Taroyan, Y. (2008). Hinode EUV spectroscopic observations of coronal oscillations. *Astron. Astrophys.*, 489:L49–L52.

Freij, N., Scullion, E. M., Nelson, C. J., Mumford, S., Wedemeyer, S., and Erdélyi, R. (2014). The Detection of Upwardly Propagating Waves Channeling Energy from the Chromosphere to the Low Corona. *Astrophys. J.*, 791(1):61.

Goddard, C. R. and Nakariakov, V. M. (2016). Dependence of kink oscillation damping on the amplitude. *Astron. Astrophys.*, 590:L5.

Goddard, C. R. and Nisticò, G. (2020). Temporal evolution of oscillating coronal loops. *Astron. Astrophys.*, 638:A89.

Goddard, C. R., Nisticò, G., Nakariakov, V. M., and Zimovets, I. V. (2016). A statistical study of decaying kink oscillations detected using SDO/AIA. *Astron. Astrophys.*, 585:A137.

Goddard, C. R., Pascoe, D. J., Anfinogentov, S., and Nakariakov, V. M. (2017). A statistical study of the inferred transverse density profile of coronal loop threads observed with SDO/AIA. *Astron. Astrophys.*, 605:A65.

Goossens, M., Andries, J., and Aschwanden, M. J. (2002). Coronal loop oscillations. An interpretation in terms of resonant absorption of quasi-mode kink oscillations. *Astron. Astrophys.*, 394:L39–L42.

Goossens, M., Erdélyi, R., and Ruderman, M. S. (2011). Resonant MHD waves in the solar atmosphere. *Space Sci. Rev.*, 158:289–338.

Goossens, M., Hollweg, J. V., and Sakurai, T. (1992). Resonant behavior of MHD waves on magnetic-flux tubes. 3. Effect of equilibrium-flow. *Solar Phys.*, 138:233–255.

He, J. S., Tu, C. Y., Marsch, E., Guo, L. J., Yao, S., and Tian, H. (2009). Upward propagating high-frequency Alfvén waves as identified from dynamic wave-like spicules observed by SOT on Hinode. *Astron. Astrophys.*, 497(2):525–535.

Heyvaerts, J. and Priest, E. R. (1983). Coronal heating by phase-mixed shear Alfven waves. *Astron. Astrophys.*, 117:220–234.

Hollweg, J. V. (1991). Alfvén Waves. In Ulmschneider, P., Priest, E. R., and Rosner, R., editors, *Mechanisms of Chromospheric and Coronal Heating*, page 260.

Hollweg, J. V. and Yang, G. (1988). Resonant-absorption of compressible magnetohydrodynamic waves at thin surfaces. *Computer Phys. Rep.*, 93:5423–5436.

Hood, A. W., Ruderman, M., Pascoe, D. J., De Moortel, I., Terradas, J., and Wright, A. N. (2013). Damping of kink waves by mode coupling. I. Analytical treatment. *Astron. Astrophys.*, 551:A39.

Ionson, J. A. (1978). Resonant absorption of Alfvénic surface waves and the heating of solar coronal loops. *Astrophys. J.*, 226:650–673.

Ishikawa, R. T., Katsukawa, Y., Antolin, P., and Toriumi, S. (2020). Temporal and Spatial Scales in Coronal Rain Revealed by UV Imaging and Spectroscopic Observations. *Solar Phys.*, 295(4):53.

Jess, D. B., Shelyag, S., Mathioudakis, M., Keys, P. H., Christian, D. J., and Keenan, F. P. (2012). Propagating Wave Phenomena Detected in Observations and Simulations of the Lower Solar Atmosphere. *Astrophys. J.*, 746(2):183.

Kelvinsong (2014). *https://commons.wikimedia.org/w/index.php?curid=23371669*.

Kleint, L., Antolin, P., Tian, H., Judge, P., Testa, P., De Pontieu, B., Martínez-Sykora, J., Reeves, K. K., Wuelser, J. P., McKillop, S., Saar, S., Carlsson, M., Boerner, P., Hurlburt, N., Lemen, J., Tarbell, T. D., Title, A., Golub, L., Hansteen, V., Jaeggli, S., and Kankelborg, C. (2014). Detection of Supersonic Downflows and Associated Heating Events in the Transition Region above Sunspots. *Astrophys. J. Lett.*, 789(2):L42.

Klimchuk, J. A. (2000). Cross-Sectional Properties of Coronal Loops. *Solar Phys.*, 193:53–75.

Klimchuk, J. A. (2006). On Solving the Coronal Heating Problem. *Solar Phys.*, 234(1):41–77.

Klimchuk, J. A. (2015). Key aspects of coronal heating. *Philosophical Transactions of the Royal Society of London Series A*, 373(2042):20140256–20140256.

Krishna Prasad, S., Banerjee, D., and Singh, J. (2012). Oscillations in Active Region Fan Loops: Observations from EIS/ Hinode and AIA/SDO. *Solar Phys.*, 281(1):67–85.

Krishna Prasad, S., Jess, D. B., Klimchuk, J. A., and Banerjee, D. (2017). Unravelling the Components of a Multi-thermal Coronal Loop using Magnetohydrodynamic Seismology. *Astrophys. J.*, 834(2):103.

Kumar, P., Cho, K. S., Chen, P. F., Bong, S. C., and Park, S.-H. (2013). Multiwavelength Study of a Solar Eruption from AR NOAA 11112: II. Large-Scale Coronal Wave and Loop Oscillation. *Solar Phys.*, 282(2):523–541.

Kuridze, D., Morton, R. J., Erdélyi, R., Dorrian, G. D., Mathioudakis, M., Jess, D. B., and Keenan, F. P. (2012). Transverse Oscillations in Chromospheric Mottles. *Astrophys. J.*, 750(1):51.

Lemen, J. R., Title, A. M., Akin, D. J., Boerner, P. F., Chou, C., Drake, J. F., Duncan, D. W., Edwards, C. G., Friedlaender, F. M., Heyman, G. F., Hurlburt, N. E., Katz, N. L., Kushner, G. D., Levay, M., Lindgren, R. W., Mathur, D. P., McFeaters, E. L., Mitchell, S., Rehse, R. A., Schrijver, C. J., Springer, L. A., Stern, R. A., Tarbell, T. D., Wuelser, J.-P., Wolfson, C. J., Yanari, C., Bookbinder, J. A., Cheimets, P. N., Caldwell, D., Deluca, E. E., Gates, R., Golub, L., Park, S., Podgorski, W. A., Bush, R. I., Scherrer, P. H., Gummin, M. A., Smith, P., Auker, G., Jerram, P., Pool, P., Soufli, R., Windt, D. L., Beardsley, S., Clapp, M., Lang, J., and Waltham, N. (2012). The Atmospheric Imaging Assembly (AIA) on the Solar Dynamics Observatory (SDO). *Solar Phys.*, 275(1-2):17–40.

Lin, Y., Engvold, O., Rouppe van der Voort, L. H. M., and van Noort, M. (2007). Evidence of Traveling Waves in Filament Threads. *Solar Physics*, 246:65–72.

Lin, Y., Engvold, O., Soler, R., Engvold, O., Ballester, J. L., Langangen, O., and Oliver, R. (2009). Swaying Threads of a Solar Filament. *Astrophys. J.*, 704:870–876.

Liu, Y., Xiang, Y., Erdélyi, R., Liu, Z., Li, D., Ning, Z., Bi, Y., Wu, N., and Lin, J. (2018). Studies of Isolated and Non-isolated Photospheric Bright Points in an Active Region Observed by the New Vacuum Solar Telescope. *Astrophys. J.*, 856(1):17.

Löhner-Böttcher, J. and Bello González, N. (2015). Signatures of running penumbral waves in sunspot photospheres. *Astron. Astrophys.*, 580:A53.

López Fuentes, M. C., Klimchuk, J. A., and Mandrini, C. H. (2007). The Temporal Evolution of Coronal Loops Observed by GOES SXI. *Astrophys. J.*, 657:1127–1136.

Luna, M., Terradas, J., Oliver, R., and Ballester, J. L. (2006). Fast magnetohydrodynamic waves in a two-slab coronal structure: collective behaviour. *Astron. Astrophys.*, 457(3):1071–1079.

Magyar, N. and Van Doorsselaere, T. (2016). Damping of nonlinear standing kink oscillations: a numerical study. *Astron. Astrophys.*, 595:A81.

Magyar, N., Van Doorsselaere, T., and Marcu, A. (2015). Numerical simulations of transverse oscillations in radiatively cooling coronal loops. *Astron. Astrophys.*, 582:A117.

Mathioudakis, M., Jess, D. B., and Erdélyi, R. (2013). Alfvén Waves in the Solar Atmosphere. From Theory to Observations. *Space Sci. Rev.*, 175(1-4):1–27.

McLaughlin, J. A., Hood, A. W., and de Moortel, I. (2011). Review Article: MHD Wave Propagation Near Coronal Null Points of Magnetic Fields. *Space Sci. Rev.*, 158(2-4):205–236.

Morton, R., Hood, A., and Erdélyi, R. (2010). Propagating MHD waves in a cooling homogenous coronal plasma. *Astron. Astrophys.*, 512:A23.

Morton, R. J. and Erdélyi, R. (2009). Transverse Oscillations of a Cooling Coronal Loop. *Astrophys. J.*, 707:750–760.

Morton, R. J. and Erdélyi, R. (2010). Application of the theory of damping of kink oscillations by radiative cooling of coronal loop plasma. *Astron. Astrophys.*, 519:A43.

Morton, R. J., Verth, G., Jess, D. B., Kuridze, D., Ruderman, M. S., Mathioudakis, M., and Erdélyi, R. (2012). Observations of ubiquitous compressive waves in the Sun's chromosphere. *Nature Communications*, 3:1315.

Nakariakov, V. M. (2006). Magnetohydrodynamic waves in coronal polar plumes. *Philosophical Transactions of the Royal Society of London Series A*, 364(1839):473–483.

Nakariakov, V. M. and Ofman, L. (2001). Determination of the coronal magnetic field by coronal loop oscillations. *Astron. Astrophys.*, 372:L53–L56.

Nakariakov, V. M., Ofman, L., Deluca, E. E., Roberts, B., and Davila, J. M. (1999). TRACE observation of damped coronal loop oscillations: Implications for coronal heating. *Science*, 285:862–864.

Nakariakov, V. M., Pilipenko, V., Heilig, B., Jelínek, P., Karlický, M., Klimushkin, D. Y., Kolotkov, D. Y., Lee, D. H., Nisticò, G., Van Doorsselaere, T., Verth, G., and Zimovets, I. V. (2016). Magnetohydrodynamic Oscillations in the Solar Corona and Earth's Magnetosphere: Towards Consolidated Understanding. *Space Sci. Rev.*, 200(1-4):75–203.

Nakariakov, V. M. and Verwichte, E. (2005). Coronal Waves and Oscillations. *Living Reviews in Solar Physics*, 2:3–+.

Nelson, C. J., Krishna Prasad, S., and Mathioudakis, M. (2020a). Evolution Of Downflows In The Transition Region Above A Sunspot Over Short Time-Scales. *arXiv e-prints*, page arXiv:2006.13617.

Nelson, C. J., Krishna Prasad, S., and Mathioudakis, M. (2020b). Evolution of supersonic downflows in a sunspot. *Astron. Astrophys.*, 636:A35.

Nelson, C. J., Shukhobodskiy, A. A., Erdélyi, R., and Mathioudakis, M. (2019). The Effect Of Cooling On Driven Kink Oscillations Of Coronal Loops. *Frontiers in Astronomy and Space Sciences*, 6:45.

Ofman, L., Romoli, M., Poletto, G., Noci, G., and Kohl, J. L. (1997). Ultraviolet Coronagraph Spectrometer Observations of Density Fluctuations in the Solar Wind. *Astrophys. J. Lett.*, 491(2):L111–L114.

Okamoto, L., Tsuneta, S., Berger, T. E., and et al. (2007). Coronal Transverse Magnetohydrodynamic Waves in a Solar Prominence. *Science*, 318:1577–.

Osterbrock, D. E. (1961). The Heating of the Solar Chromosphere, Plages, and Corona by Magnetohydrodynamic Waves. *Astrophys. J.*, 134:347.

Parnell, C. E. and De Moortel, I. (2012). A contemporary view of coronal heating. *Philosophical Transactions of the Royal Society of London Series A*, 370(1970):3217–3240.

Pascoe, D. J., Goddard, C. R., and Nakariakov, V. M. (2016a). Spatially resolved observation of the fundamental and second harmonic standing kink modes using SDO/AIA. *Astron. Astrophys.*, 593:A53.

Pascoe, D. J., Goddard, C. R., Nisticò, G., Anfinogentov, S., and Nakariakov, V. M. (2016b). Coronal loop seismology using damping of standing kink oscillations by mode coupling. *Astron. Astrophys.*, 589:A136.

Pascoe, D. J., Goddard, C. R., Nisticò, G., Anfinogentov, S., and Nakariakov, V. M. (2016c). Damping profile of standing kink oscillations observed by SDO/AIA. *Astron. Astrophys.*, 585:L6.

Pascoe, D. J., Hood, A. W., De Moortel, I., and Wright, A. N. (2013). Damping of kink waves by mode coupling. II. Parametric study and seismology. *Astron. Astrophys.*, 551:A40.

Pascoe, D. J., Hood, A. W., and Van Doorsselaere, T. (2019). Coronal loop seismology using standing kink oscillations with a lookup table. *Frontiers in Astronomy and Space Sciences*, 6:22.

Pascoe, D. J., Russell, A. J. B., Anfinogentov, S. A., Simões, P. J. A., Goddard, C. R., Nakariakov, V. M., and Fletcher, L. (2017). Seismology of contracting and expanding coronal loops using damping of kink oscillations by mode coupling. *Astron. Astrophys.*, 607:A8.

Pascoe, D. J., Smyrli, A., and Van Doorsselaere, T. (2020). Tracking and Seismological Analysis of Multiple Coronal Loops in an Active Region. *Astrophys. J.*, 898(2):126.

Pascoe, D. J., Wright, A. N., and De Moortel, I. (2010). Coupled Alfvén and Kink Oscillations in Coronal Loops. *Astrophys. J.*, 711(2):990–996.

Pascoe, D. J., Wright, A. N., and De Moortel, I. (2011). Propagating Coupled Alfvén and Kink Oscillations in an Arbitrary Inhomogeneous Corona. *Astrophys. J.*, 731(1):73.

Pintér, B. and Erdélyi, R. (2011). Effects of Magnetic Fields in the Solar Atmosphere on Global Oscillations. *Space Sci. Rev.*, 158(2-4):471–504.

Priest, E. (2014). *Magnetohydrodynamics of the Sun*.

Priest, E. R. (1999). Heating the Solar Corona by Magnetic Reconnection. *Astrophys. Space Sci.*, 264:77–100.

Roberts, B. (1981a). Wave propagation in a magnetically structured atmosphere. I - Surface waves at a magnetic interface. *Solar Physics*, 69:27–38.

Roberts, B. (1981b). Wave propagation in a magnetically structured atmosphere. II - Waves in a magnetic slab. *Solar Physics*, 69:39–56.

Roberts, B. (2000). Waves and Oscillations in the Corona - (Invited Review). *Solar Physics*, 193:139–152.

Roberts, B., Edwin, P. M., and Benz, A. O. (1984). On coronal oscillations. *Astrophys. J.*, 279:857–865.

Ruderman, M. S. (1992). Soliton propagation on multiple-interface magnetic structures. *J. Geophys. Res.*, 97(A11):16843–16854.

Ruderman, M. S. (2011a). Erratum to: Transverse oscillations of coronal loops with slowly changing density. *Solar Physics*, 271:55–56.

Ruderman, M. S. (2011b). Resonant damping of kink oscillations of cooling coronal magnetic loops. *Astron. Astrophys.*, 534:A78.

Ruderman, M. S. (2011c). Transverse oscillations of coronal loops with slowly changing density. *Solar Physics*, 271:41–54.

Ruderman, M. S. (2017). Nonlinear Generation of Fluting Perturbations by Kink Mode. *Solar Physics*, 292(8):111.

Ruderman, M. S. and Erdélyi, R. (2009). Transverse Oscillations of Coronal Loops. *Space Science Reviews*, 149:199–228.

Ruderman, M. S., Goossens, M., and Andries, J. (2010). Nonlinear propagating kink waves in thin magnetic tubes. *Physics of Plasmas*, 17(8):082108.

Ruderman, M. S. and Petrukhin, N. S. (2019). Effect of siphon flow on resonant damping of kink oscillations in magnetic flux tubes. *Astron. Astrophys.*, 631:A31.

Ruderman, M. S. and Roberts, B. (2002). The Damping of Coronal Loop Oscillations. *Astrophys. J.*, 577:475–486.

Ruderman, M. S., Shukhobodskaya, D., and Shukhobodskiy, A. A. (2019). Resonant damping of propagating kink waves in non-stationary, longitudinally stratified, and expanding solar waveguides. *Frontiers in Astronomy and Space Sciences*, 6:10.

Ruderman, M. S., Shukhobodskiy, A. A., and Erdélyi, R. (2017). Kink oscillations of cooling coronal loops with variable cross-section. *Astron. Astrophys.*, 602:A50.

Ruderman, M. S. and Terradas, J. (2013). Damping of coronal loop kink oscillations due to mode conversion. *Astron. Astrophys.*, 555:A27.

Ruderman, M. S., Tirry, W., and Goossens, M. (1995). Non-stationary resonant Alfvén surface waves in one-dimensional magnetic plasmas. *Journal of Plasma Physics*, 54(2):129–148.

Ruderman, M. S., Verth, G., and Erdélyi, R. (2008). Transverse Oscillations of Longitudinally Stratified Coronal Loops with Variable Cross Section. *Astrophys. J.*, 686:694–700.

Ryutov, D. D. and Ryutova, M. P. (1976). Sound oscillations in a plasma with "magnetic filaments". *Sov. Phys. – JETP*, 43:491–000.

Samanta, T., Tian, H., and Prasad Choudhary, D. (2018). Statistical Investigation of Supersonic Downflows in the Transition Region above Sunspots. *Astrophys. J.*, 859(2):158.

Schmelz, J. T. and Martens, P. C. H. (2005). Multithermal analysis of a SOHO /CDS coronal loop. *The Astrophysical Journal*, 636(1):L49–L52.

Schmelz, J. T., Nasraoui, K., Zanna, G. D., Cirtain, J. W., DeLuca, E. E., and Mason, H. E. (2007). Coronal diagnostic spectrometer observations of isothermal and multithermal coronal loops. *The Astrophysical Journal*, 658(2):L119–L122.

Shukhobodskaia, D. and Erdélyi, R. (2018). Propagation of Surface Magnetohydrodynamic Waves in Asymmetric Multilayered Plasma. *Astrophys. J.*, 868(2):128.

Shukhobodskaia, D., Shukhobodskiy, A. A., and Erdélyi, R. (submitted 2021). Flute oscillations of cooling coronal loops with variable cross-section. *Astron. Astrophys.*.

Shukhobodskaia, D., Shukhobodskiy, A. A., Nelson, C. J., Ruderman, M. S., and Erdélyi, R. (2020). Significance of Cooling Effect On Comprehension of Kink Oscillations of Coronal Loops. *Frontiers in Astronomy and Space Sciences*, in press.

Shukhobodskiy, A. A. and Ruderman, M. S. (2018). Resonant damping of kink oscillations of thin expanding magnetic tubes. *Astron. Astrophys.*, 615:A156.

Shukhobodskiy, A. A., Ruderman, M. S., and Erdélyi, R. (2018). Resonant damping of kink oscillations of thin cooling and expanding coronal magnetic loops. *Astron. Astrophys.*, 619:A173.

Soler, R. (2017). Fluting Modes in Transversely Nonuniform Solar Flux Tubes. *Astrophys. J.*, 850(2):114.

Soler, R., Oliver, R., and Ballester, J. L. (2011a). Spatial Damping of Propagating Kink Waves in Prominence Threads. *Astrophys. J.*, 726(2):102.

Soler, R., Terradas, J., and Goossens, M. (2011b). Spatial Damping of Propagating Kink Waves Due to Resonant Absorption: Effect of Background Flow. *Astrophys. J.*, 734(2):80.

Soler, R., Terradas, J., Verth, G., and Goossens, M. (2011c). Resonantly Damped Propagating Kink Waves in Longitudinally Stratified Solar Waveguides. *Astrophys. J.*, 736(1):10.

Straus, T., Fleck, B., and Andretta, V. (2015). A steady-state supersonic downflow in the transition region above a sunspot umbra. *Astron. Astrophys.*, 582:A116.

Tandberg-Hanssen, E. (1995). *The nature of solar prominences*. Astrophysics and Space Science Library. Springer Netherlands.

Terradas, J., Andries, J., Goossens, M., Arregui, I., Oliver, R., and Ballester, J. L. (2008). Nonlinear Instability of Kink Oscillations due to Shear Motions. *Astrophys. J. Lett.*, 687:L115–L118.

Terradas, J., Goossens, M., and Verth, G. (2010). Selective spatial damping of propagating kink waves due to resonant absorption. *ArXiv e-prints*.

Terradas, J., Magyar, N., and Van Doorsselaere, T. (2018). Effect of Magnetic Twist on Nonlinear Transverse Kink Oscillations of Line-tied Magnetic Flux Tubes. *Astrophys. J.*, 853(1):35.

Thompson, B. J., Plunkett, S. P., Gurman, J. B., Newmark, J. S., St. Cyr, O. C., and Michels, D. J. (1998). SOHO/EIT observations of an Earth-directed coronal mass ejection on May 12, 1997. *Geophys. Res. Lett.*, 25(14):2465–2468.

Tomczyk, S. and McIntosh, S. W. (2009). Time-Distance Seismology of the Solar Corona with CoMP. *Astrophys. J.*, 697(2):1384–1391.

Tomczyk, S., McIntosh, S. W., Keil, S. L., Judge, P. G., Schad, T., Seeley, D. H., and Edmondson, J. (2007). Alfvén Waves in the Solar Corona. *Science*, 317:1192–.

Tsiropoula, G., Tziotziou, K., Kontogiannis, I., Madjarska, M. S., Doyle, J. G., and Suematsu, Y. (2012). Solar Fine-Scale Structures. I. Spicules and Other Small-Scale, Jet-Like Events at the Chromospheric Level: Observations and Physical Parameters. *Space Sci. Rev.*, 169(1-4):181–244.

Uchida, Y. (1970). Diagnosis of Coronal Magnetic Structure by Flare-Associated Hydromagnetic Disturbances. *PASJ*, 22:341–+.

Verth, G., Terradas, J., and Goossens, M. (2010). Observational Evidence of Resonantly Damped Propagating Kink Waves in the Solar Corona. *Astrophys. J. Lett.*, 718:L102–L105.

Wang, T., Ofman, L., Davila, J. M., and Su, Y. (2012). Growing Transverse Oscillations of a Multistranded Loop Observed by SDO/AIA. *Astrophys. J. Lett.*, 751(2):L27.

Watko, J. A. and Klimchuk, J. A. (2000). Width Variations along Coronal Loops Observed by TRACE. *Solar Physics*, 193:77–93.

Winebarger, A. R. and Warren, H. P. (2005). Cooling Active Region Loops Observed with SXT and TRACE. *Astrophys. J.*, 626:543–550.

Xiong, J., Yang, Y., Jin, C., Ji, K., Feng, S., Wang, F., Deng, H., and Hu, Y. (2017). The Characteristics of Thin Magnetic Flux Tubes in the Lower Solar Atmosphere Observed by Hinode/SOT in the G band and in Ca II H Bright Points. *Astrophys. J.*, 851(1):42.

Yang, S., Zhang, J., and Erdélyi, R. (2016). Enhancement of a Sunspot Light Wall with External Disturbances. *Astrophys. J. Lett.*, 833(2):L18.

Yang, S., Zhang, J., Erdélyi, R., Hou, Y., Li, X., and Yan, L. (2017). Sunspot Light Walls Suppressed by Nearby Brightenings. *Astrophys. J. Lett.*, 843(1):L15.

Yang, S., Zhang, J., Jiang, F., and Xiang, Y. (2015). Oscillating Light Wall Above a Sunspot Light Bridge. *Astrophys. J. Lett.*, 804:L27.

Yuan, D., Nakariakov, V. M., Huang, Z., Li, B., Su, J., Yan, Y., and Tan, B. (2014). Oscillations in a Sunspot with Light Bridges. *Astrophys. J.*, 792(1):41.

Zajtsev, V. V. and Stepanov, A. V. (1975). On the origin of pulsations of type IV solar radio emission. Plasma cylinder oscillations (I). *Issledovaniia Geomagnetizmu Aeronomii i Fizike Solntsa*, 37:3–10.

Zaqarashvili, T. V. and Erdelyi, R. (2009). Oscillations and waves in solar spicules. *ArXiv e-prints*.

Zhang, J., Tian, H., He, J., and Wang, L. (2017). Surge-like Oscillations above Sunspot Light Bridges Driven by Magnetoacoustic Shocks. *Astrophys. J.*, 838(1):2.

Zimovets, I. V. and Nakariakov, V. M. (2015). Excitation of kink oscillations of coronal loops: statistical study. *Astron. Astrophys.*, 577:A4.

Zsámberger, N. K., Allcock, M., and Erdélyi, R. (2018). Magneto-acoustic Waves in a Magnetic Slab Embedded in an Asymmetric Magnetic Environment: The Effects of Asymmetry. *Astrophys. J.*, 853(2):136.